

# NOTE TO USERS

This reproduction is the best copy available.

**UMI**®



# **EFFECT OF A SLAT ARM DOOR ON THE WING EFFICIENCY OF A COMMERCIAL AIRCRAFT**

By

**Sharman Perera, B.Eng.**

Department of Aerospace Engineering

Ryerson University

Toronto, Ontario, Canada

Year 2001

A thesis

Presented to Ryerson University

In partial fulfillment of the  
Requirement for the degree of  
Master in Applied Science  
In the program of  
Mechanical Engineering

Toronto, Ontario, Canada 2004

© Sharman Perera 2004

PROPERTY OF  
RYERSON UNIVERSITY LIBRARY

UMI Number: EC52953

### INFORMATION TO USERS

The quality of this reproduction is dependent upon the quality of the copy submitted. Broken or indistinct print, colored or poor quality illustrations and photographs, print bleed-through, substandard margins, and improper alignment can adversely affect reproduction.

In the unlikely event that the author did not send a complete manuscript and there are missing pages, these will be noted. Also, if unauthorized copyright material had to be removed, a note will indicate the deletion.

**UMI**<sup>®</sup>

---

UMI Microform EC52953

Copyright 2008 by ProQuest LLC.

All rights reserved. This microform edition is protected against unauthorized copying under Title 17, United States Code.

ProQuest LLC  
789 E. Eisenhower Parkway  
PO Box 1346  
Ann Arbor, MI 48106-1346

---

## **Abstract**

### **EFFECT OF A SLAT ARM DOOR ON THE WING EFFICIENCY OF A COMMERCIAL AIRCRAFT**

**Sharman Perera, MASc.**  
Department of Mechanical Engineering  
Ryerson University  
Toronto, Ontario, Canada  
Year 2004

The objective of this thesis is to determine the influence of a slat arm door on the aerodynamic performance of a wing of a commercial aircraft during its take off and landing configurations using CFD simulation. The slats are extended forward by extendable arms coming out from the leading edge of the wing through the openings. A door covers the top part of the opening of the leading edge of the wing after the slat arm is deployed. CFD analysis of wing and slat configuration of the aircraft showed that the removal of this slat door at higher angle of attacks increased the drag by 0.88%, reduced the lift by 1.29%, increased the inert particle residence time inside the slat door compartment by 200.00% and increased the local flow separation area on the top surface of the wing by 42.81% with reference to the closed model.

---

## Acknowledgments

The author would like to thank, Professor Paul Walsh for his unfailing support, other professors at Ryerson University for their guidance and Manufacturing Materials Ontario (MMO) for providing the funding for this work. Without their supports this project could not have been completed. Special thanks to technical staff at Ryerson University, namely Gerald Bootes and Jason Naughton who assisted the author in administering the computer system and providing computer access under less than ideal circumstances.

---

## **Dedication**

The author would like to dedicate this project to his wife and darling daughter Kaylan.

---

## **Special notes**

Some pictures of the thesis report left blank intentionally for confidentiality reasons. These pictures are replaced by text boxes with a word "OMITTED" written at the center.



## Table of contents

|  | Page No. |
|--|----------|
| Author's declaration.....  | ii       |
| Abstract .....   | iii      |
| Acknowledgments .....  | iv       |
| Dedication.....  | v        |
| Special notes .....  | vi       |
| Table of contents .....  | vii      |
| List of tables .....   | x        |
| Table of figures .....   | xi       |
| Nomenclature .....   | xvi      |
| <br>CHAPTER 1: INTRODUCTION.....                                     | <br>1    |
| 1.1 Background .....   | 1        |
| 1.2 Use of high lift devices on the Aurora aircraft.....             | 2        |
| 1.3 High lift devices aerodynamics .....                             | 5        |
| 1.3.1 Flap aerodynamics.....   | 5        |
| 1.3.2 Slat aerodynamics.....   | 7        |
| 1.4 Boundary layer phenomena.....                                    | 8        |
| 1.4.1 Laminar sub layer .....  | 9        |
| 1.4.2 Boundary layer interaction and creation of vortices.....       | 10       |
| 1.4.3 Angle of attack and boundary layer separation .....            | 12       |
| 1.5 Reynolds number effect.....                                      | 14       |
| 1.6 Aircraft corrosion due to contaminants around the airports ..... | 15       |

---

|   |           |
|---|-----------|
| 1.7 General approach to the problem .....                               | 16        |
| 1.7.1 Previous studies .....  | 16        |
| 1.8 Thesis objectives .....   | 18        |
| 1.9 Thesis overview .....   | 18        |
| <b>CHAPTER 2: USE OF CFD IN AEROSPACE ENGINEERING .....</b>             | <b>20</b> |
| 2.1 Why CFD.....  | 20        |
| 2.2 Use of CFD in aerospace industry to model high lift systems.....    | 21        |
| 2.3 Advantages of using CFD methods over wind tunnel testing .....      | 21        |
| 2.3.1 CFD modeling of a wind tunnel.....                                | 23        |
| 2.4 Validation of CFD codes .....                                       | 26        |
| 2.5 Testing the capabilities and limitations of FLUENT .....            | 27        |
| <b>CHAPTER 3: MESH GENERATION.....</b>                                  | <b>30</b> |
| 3.1 Import of geometry and mesh information .....                       | 31        |
| 3.2 Creation of geometry.....   | 32        |
| 3.3 Modeling of the flow domain .....                                   | 35        |
| 3.4 Creation and refinement of the mesh.....                            | 38        |
| 3.5 Assignment of zone types .....                                      | 49        |
| <b>CHAPTER 4: MODEL SELECTION AND SOLVING STRATEGIES.....</b>           | <b>52</b> |
| 4.1 Numerical techniques used in CFD.....                               | 52        |
| 4.2 Selection of the turbulence model .....                             | 53        |
| 4.2.1 Comparison of viscous models .....                                | 53        |
| 4.3 Selection of solution algorithm and solution formation method ..... | 55        |
| 4.4 Selection of appropriate time step.....                             | 56        |
| 4.5 Solver control.....   | 57        |
| 4.6 Residual monitoring .....   | 58        |

|   |           |
|---|-----------|
| <b>CHAPTER 5: THEORY .....</b>                                  | <b>60</b> |
| 5.1 Basic equations in fluid dynamics .....                     | 60        |
| 5.2 State equation.....   | 61        |
| 5.4 Spalart-Allmaras turbulence model.....                      | 61        |
| 5.5 Wall boundary conditions .....                              | 63        |
| 5.6 Discrete phase modeling.....                                | 64        |
| 5.7 Time integration .....                                      | 67        |
| 5.7.1 Implicit time integration .....                           | 67        |
| 5.7.2 Explicit time integration .....                           | 67        |
| <b>CHAPTER 6:RESULTS .....</b>                                  | <b>69</b> |
| 6.1 Fuselage effect on the wing .....                           | 70        |
| 6.2 Comparison of total configuration lift and drag.....        | 74        |
| 6.3 Surface pressures.....                                      | 78        |
| 6.4 Surface shear stress distribution .....                     | 83        |
| 6.5 Comparison of turbulence viscosity ratio .....              | 84        |
| 6.6 Dispersion of contaminants in the slat arm compartment..... | 86        |
| <b>CHAPTER 7: SUMMARY, CONCLUSIONS AND RECOMENDATIONS .....</b> | <b>91</b> |
| 7.1 Summary .....   | 91        |
| 7.2 Future challenges.....                                      | 92        |
| <b>APPENDICES.....</b>  | <b>94</b> |
| Appendix A: Continuous model .....                              | 94        |
| Appendix B: Discrete model .....                                | 95        |
| Appendix C: Reference values.....                               | 98        |
| <b>REFERENCES .....</b>   | <b>99</b> |

## List of tables

| Table   | Page No |
|---|---------|
| Table 3.4.1: Zone type specifications of the Aurora wing and slat configuration. Entity Slat-Door exists only in the closed model.  | 48      |
| Table 3.4.2: Type of cell, size and the area of the respective zones  | 49      |
| Table 4.2.1: Comparison of results for NACA 0012 airfoil at $6^\circ$ angle of attack, $M=0.21$ and Reynolds number of 13.9 million based on the mean chord.  | 55      |
| Table 4.2.2: Turbulence model scoring: Note that, the equal total scores do not mean that a models perform identically in all tests.  | 55      |
| Table 4.6.1: Convergence criterion of the residuals   | 58      |
| Table 6.2.1: Coefficient of lift ( $C_L$ ), coefficient of drag ( $C_D$ ) and difference in coefficients of $C_L$ and $C_D$ of closed and opened models found using FLUNET at a range of angle of attack. $M=0.21$ and Reynolds number of 13.9 million based on the mean chord. | 74      |
| Table B1: Facet average velocity of the rectangular interior surface at different angles of attacks. $M=0.21$ and Reynolds number of 13.9 million based on the mean chord.  | 95      |
| Table B3: The average residence time for inert particles (Sulfur) injected at different angles of attack. $M=0.21$ and Reynolds number of 13.9 million based on the mean chord.   | 97      |
| Table C1: Reference values used in the report   | 98      |

## Table of figures

| Table  | Page No. |
|--|----------|
| Figure 1.2.1: Double-slotted flap and slat system of Aurora wing at cruise, take off and landing configurations [5].   | 3        |
| Figure 1.2.2: Locations of slat arms and slat arm doors along the half a span of Aurora wing [5].  | 3        |
| Figure 1.2.3: Aurora aircraft. Picture just above the right wing shows the mechanism used to deploy the slat during take-off. The slat door is marked in dark red color with black background just above the long slat arm covering the opening [5]. | 4        |
| Figure 1.3.1: Definition of reference values used in this report.  | 5        |
| Figure 1.3.2: $C_L$ vs. flap deflection and angle of attack generated at Mach 0.2 for the DC-9-30 aircraft when slats are retracted.   | 6        |
| Figure 1.3.3: The effect of slats on the stall angle at $0^\circ$ and $40^\circ$ flaps.  | 7        |
| Figure 1.4.1: Boundary layer on a flat plate.  | 8        |
| Figure 1.4.2: Close up of a laminar sub layer over a flat plate.   | 10       |
| Figure 1.4.3: Interaction of boundary layer with the cylinder and formation of horseshoe vortices [7].   | 11       |
| Figure 1.4.4: Angle of attack vs. flow separation.   | 13       |
| Figure 1.5.1: Reynolds number effect on $C_{Lmax}$ for several Aurora aircraft and the difference between wind tunnel and in-flight testing as per McMasters and Mack. Not to a scale [12].  | 14       |
| Figure 1.7.1: Balsa wood model of Aurora wing and slat configuration built by Andrew Craig. [19]   | 17       |
| Figure 2.3.1: Wind tunnel and Free air models.   | 24       |
| Figure 2.3.2: Pressure contours of Wind Tunnel shaped model. $M=0.21$ and Reynolds number of 13.9 million based on the mean chord. $\alpha = 0^\circ$ .  | 25       |

|  |           |
|--|-----------|
| <b>Figure 2.3.3: Pressure contours of free air shaped model. <math>M=0.21</math> and Reynolds number of 13.9 million based on the mean chord. <math>\alpha=0^\circ</math>.</b>   | <b>25</b> |
| <b>Figure 2.5.1: Velocity contours of the multi element airfoil achieved using FLUENT at <math>M_\infty=0.197</math> and <math>\alpha=4.01^\circ</math>. A selected section of a mesh below the main airfoil shows how mesh is stretched in the 2D domain.</b> | <b>28</b> |
| <b>Figure 2.5.2: AGARD multi element airfoil and static pressure distribution found using FLUENT<sup>TM</sup> for <math>M_\infty=0.197</math> and <math>\alpha=4.01^\circ</math>.</b>  | <b>29</b> |
| <b>Figure 3.1.1: Aurora wing and slat configuration. Detailed model provided by Aurora Toronto showing both retracted and extended positions of the slat.</b>  | <b>30</b> |
| <b>Figure 3.2.1: Top view of Aurora aircraft. The marked solid section shows the extent of the model given by Aurora and the section with lines running diagonally shows the top view of the regenerated model, using GAMBIT.</b>                              | <b>33</b> |
| <b>Figure 3.2.2: Extruded model of Aurora wing and slat configuration.</b>   | <b>34</b> |
| <b>Figure 3.2.3: Simplified model of Aurora wing and slat configuration regenerated using GAMBIT showing slat arm door which covers the upper part of the opening. Note that slat is intentionally deleted to visualize the slat arm and the slat door.</b>    | <b>35</b> |
| <b>Figure 3.3.1: Comparison of models between all sided Pressure Far-Field and Pressure Far-Field with symmetry boundary conditions.</b>   | <b>36</b> |
| <b>Figure 3.4.1: Comparison of unstructured and structured meshes. Both meshes have same off wall spacing.</b>   | <b>38</b> |
| <b>Figure 3.4.2: Use of structured mesh in continuous volumes.</b>   | <b>39</b> |
| <b>Figure 3.4.3: Flow domain of the Aurora model. Domain consists of 33 volumes. Volumes of set 1 are shown in the diagram and the rest are not shown due to clarity.</b>  | <b>40</b> |
| <b>Figure 3.4.4: Modeling boundary layers of two mating faces using GAMBIT. Picture shows the boundary layers along wing upper and lower surfaces towards the wing trailing edge.</b>  | <b>42</b> |
| <b>Figure 3.4.5: Surface mesh of the symmetry plane with respect the wing and slat surfaces.</b>   | <b>43</b> |
| <b>Figure 3.4.6: Surface mesh of a section of the extruded wing model and internal surface meshes of the flow domain.</b>  | <b>44</b> |
| <b>Figure 3.4.7: Surface meshes of the slat arm, slat rear and slat.</b>   | <b>45</b> |
| <b>Figure 3.4.8: A Cross section sketch of the opening of the wing where slat arm is coming out.</b>   | <b>46</b> |

|   |           |
|---|-----------|
| <b>Figure 3.4.9: Surface mesh of the slat box with respect to slat door and the slat arm.</b>   | <b>47</b> |
| <b>Figure 3.4.10: Surface mesh of the slat door with respect to slat doorframe.</b>   | <b>47</b> |
| <b>Figure 3.4.11: Boundary and continuum type specifications of Aurora wing and slat configuration.</b>   | <b>48</b> |
| <b>Figure 4.2.1: 2D Velocity distribution of the NSCA 0012 and slat configuration. <math>M=0.21</math> and Reynolds number of 13.9 million based on the mean chord. <math>\alpha = 6^\circ</math>.</b>  | <b>54</b> |
| <b>Figure 4.6.1: Convergence history of selected variables of Aurora wing and slat configuration. <math>M=0.21</math> and Reynolds number of 13.9 million based on the mean chord. <math>\alpha = 17.5^\circ</math>.</b>  | <b>58</b> |
| <b>Figure 5.6.1: Heat, Mass, and Momentum transfer between the discrete and continuous phases [33].</b>   | <b>65</b> |
| <b>Figure 6.1.1: Schematic of the 3D model built to simulate the full 3D aircraft. Not to scale.</b>  | <b>70</b> |
| <b>Figure 6.1.2: Velocity vectors of a plane parallel to the wing and through the fuselage and wing. <math>M=0.21</math> and Reynolds number of 13.9 million based on the mean chord. <math>\alpha = 15^\circ</math>.</b>   | <b>71</b> |
| <b>Figure 6.1.3: Static Pressure contour plots of planes through symmetry, two planes across the wing parallel to symmetry plane and a plane parallel to the wing running through the fuselage (shifted down for clarity). <math>M=0.21</math> and Reynolds number of 13.9 million based on the mean chord. <math>\alpha = 15^\circ</math>.</b> | <b>71</b> |
| <b>Figure 6.1.4: Static Pressure contour plots of two planes across the wing parallel to symmetry plane and filled pressure contours of the wing of the models with fuselage. <math>M=0.21</math> and Reynolds number of 13.9 million based on the mean chord. <math>\alpha = 15^\circ</math>.</b>  | <b>72</b> |
| <b>Figure 6.1.5: Static Pressure contour plots of two planes across the wing parallel to symmetry plane and filled pressure contours of the wing of the models without fuselage. <math>M=0.21</math> and Reynolds number of 13.9 million based on the mean chord. <math>\alpha = 15^\circ</math>.</b>   | <b>72</b> |
| <b>Figure 6.2.1: <math>C_L</math> vs. <math>\alpha</math> for closed and opened configurations of base models. <math>M=0.21</math> and Reynolds number of 13.9 million based on the mean chord.</b>   | <b>75</b> |
| <b>Figure 6.2.2: <math>C_L</math> vs. <math>\alpha</math> for closed and opened configurations of base models. <math>M=0.21</math> and Reynolds number of 13.9 million based on the mean chord.</b>   | <b>76</b> |

|  |           |
|--|-----------|
| <b>Figure 6.2.3: Difference in lift and drag coefficients between the slat door opened and closed cases. (closed –opened). <math>M=0.21</math> and Reynolds number of 13.9 million based on the mean chord..</b>   | <b>77</b> |
| <b>Figure 6.3.1: Locations of the planes where <math>C_p</math> distributions are depicted in figures 6.3.2 to 6.3.8</b>   | <b>78</b> |
| <b>Figure 6.3.2: Comparison of <math>C_p</math> on slat and wing at 0% location between closed (left) and opened (right) models calculated at Mach number of 0.21, angle of attack of <math>17.5^\circ</math> and Reynolds number of 13.90 million.</b>    | <b>78</b> |
| <b>Figure 6.3.3: Comparison of <math>C_p</math> on slat and wing at 25% location between closed (left) and opened (right) models calculated at Mach number of 0.21, angle of attack of <math>17.5^\circ</math> and Reynolds number of 13.90 million.</b>   | <b>79</b> |
| <b>Figure 6.3.4: Comparison of <math>C_p</math> on slat and wing at 32.5% location between closed (left) and opened (right) models calculated at Mach number of 0.21, angle of attack of <math>17.5^\circ</math> and Reynolds number of 13.90 million.</b> | <b>79</b> |
| <b>Figure 6.3.5: Comparison of <math>C_p</math> on slat and wing at 50% location between closed (left) and opened (right) models calculated at Mach number of 0.21, angle of attack of <math>17.5^\circ</math> and Reynolds number of 13.90 million.</b>   | <b>80</b> |
| <b>Figure 6.3.6: Comparison of <math>C_p</math> on slat and wing at 62.5% location between closed (left) and opened (right) models calculated at Mach number of 0.21, angle of attack of <math>17.5^\circ</math> and Reynolds number of 13.90 million.</b> | <b>80</b> |
| <b>Figure 6.3.7: Comparison of <math>C_p</math> on slat and wing at 75% location between closed (left) and opened (right) models calculated at Mach number of 0.21, angle of attack of <math>17.5^\circ</math> and Reynolds number of 13.90 million.</b>   | <b>81</b> |
| <b>Figure 6.3.8: Comparison of <math>C_p</math> on slat and wing at 100% location between closed (left) and opened (right) models calculated at Mach number of 0.21, angle of attack of <math>17.5^\circ</math> and Reynolds number of 13.90 million.</b>  | <b>81</b> |
| <b>Figure 6.3.9: Pressure contours just above the slat arm with and without slat arm door. <math>M=0.21</math> and Reynolds number of 13.9 million based on the mean chord. <math>\alpha = 17.5^\circ</math>.</b>  | <b>82</b> |
| <b>Figure 6.4.1: Shear stress contour values from 0 to 5 Pascal of the wing upper surfaces of closed and opened models. <math>M=0.21</math> and Reynolds number of 13.9 million based on the mean chord. <math>\alpha = 17.5^\circ</math>.</b>             | <b>83</b> |
| <b>Figure 6.5.1: Turbulence viscosity ratio contours across a plane above the wing upper surface at 20% chord behind the wing leading edge and the streamlines of the</b>  |           |



|  |    |
|--|----|
| particles released from the wing box. $M=0.21$ and Reynolds number of 13.9 million based on the mean chord. $\alpha = 17.5^\circ$ .  | 84 |
| Figure 6.5.2: Modified turbulence viscosity contours of selected planes just above the wing upper surface of slat  | 85 |
| arm door closed model. $M=0.21$ and Reynolds number of 13.9 million based on the mean chord. $\alpha = 17.5^\circ$ .   | 85 |
| Figure 6.5.3: Modified turbulence viscosity contours of selected planes just above the wing upper surface of slat arm door opened model. $M=0.21$ and Reynolds number of 13.9 million based on the mean chord. $\alpha = 17.5^\circ$ . | 85 |
| Figure 6.6.1: Location of the face where injections were released.   | 86 |
| Figure 6.6.2: Direction and the magnitude of the velocity vectors going through a plane across the slat door cavity. $M=0.21$ and Reynolds number of 13.9 million based on the mean chord.   | 87 |
| Figure 6.6.3: Particle track of selected 8 particles at $0^\circ$ angle of attack. Trajectories of particles are represented as the cylinders.   | 88 |
| Figure 6.6.4: Particle track of selected 8 particles at $10^\circ$ angle of attack. Trajectories of particles are represented as the cylinders.  | 88 |
| Figure 6.6.5: Particle track of selected 8 particles at $15^\circ$ angle of attack. Trajectories of particles are represented as the cylinders.  | 89 |
| Figure 6.6.6: Average residence time of sulfur particles inside the slat box in seconds at different angles of attack. $M=0.21$ and Reynolds number of 13.9 million based on the mean chord.   | 90 |
| Figure A1: Isometric views of Aurora aircraft [1]  | 94 |
| Figure B1: Facet average velocity of the rectangular interior surface at different angles of attacks. $M=0.21$ and Reynolds number of 13.9 million based on the mean chord.  | 96 |

---

## Nomenclature

### Acronyms

|               |   |
|---------------|---|
| 2D            | Two dimensional                               |
| 3D            | Three dimensional                             |
| ATOP          | Advanced computational lab                    |
| B             | Bit   |
| CFD           | Computational fluid dynamics                  |
| CFL           | Courant Friedrichs Lewy number                |
| DF            | Discrete phase model                          |
| FNSE          | Full Navier-Stokes equations                  |
| GPS           | Global positioning system                     |
| IGES          | Initial graphics exchange specification       |
| IO            | Input and out put ratio of a processor        |
| k- $\epsilon$ | k-epsilon model                               |
| LES           | Large eddy simulation                         |
| NASA          | National aeronautics and space administration |
| RAM           | Random access memory                          |
| RANS          | Reynolds-averaged approach                    |
| SA            | Spalart-Allmaras model                        |
| STP           | Standard temperature and pressure             |

### Variables

|                          |   |
|--------------------------|---|
| $a_1, a_2, a_3$          | Constant, DF model  |
| $A_\Omega$               | Surface of the control volume   |
| $b_1, b_2, b_3, b_4$     | Constants, DF model   |
| $C$                      | Wing mean chord   |
| $C_{b1}, C_{b2}, k_1$    | Constants, SA model   |
| $C_D$                    | Drag coefficient  |
| $C_L$                    | Lift coefficient  |
| $C_p$                    | Pressure coefficient  |
| $C_{prod}$               | Constant, SA model  |
| $C_{v1}$                 | Constant, SA model  |
| $C_{w1}, C_{w2}, C_{w3}$ | Constants, SA model   |
| $D$                      | Distance from the wall, SA model  |
| $D_p$                    | Particle diameter, DFM model  |
| $f_{v1}$                 | Viscosity damping function, SA model                                      |
| $F_D$                    | Drag force, DF model  |
| $f_{v1}$                 | Viscosity damping function, SA model                                      |
| $F_x$                    | Force required to accelerate the fluid surrounding the particle, DF model |
| $G_v$                    | Product of turbulent viscosity in SA model                                |
| $K$                      | Conduction coefficient  |
| $L_c$                    | Length of original wing section   |

---

|   |   |
|---|---|
| P   | Pressure  |
| PFFB  | Pressure far field boundary   |
| Q   | Heat flux vector  |
| Q   | Vector of dependent variables   |
| R   | Universal gas constant  |
| S   | Scalar measure of the deformation tensor                                |
| S   | Source term vector  |
| SB  | Symmetry boundary   |
| S <sub>E</sub>                                      | Source of energy per unit volume  |
| S <sub>ij</sub>                                     | Mean strain rate  |
| S <sub>Mx</sub> , S <sub>My</sub> , S <sub>Mz</sub> | Body forces acting along x,y and z directions                           |
| s <sub>p</sub>                                      | Surface area of the sphere having same volume of the particle, DF model |
| S <sub>p</sub>                                      | Actual surface area of the particle                                     |
| S <sub>Slat-Door</sub>                              | Surface area of the slat door   |
| T   | Local temperature   |
| U <sub>l</sub>                                      | Laminar strain  |
| u,v,w   | Velocity components into x, y and z directions                          |
| u <sup>2</sup> v <sup>2</sup>                       | Products of velocity fluctuations                                       |
| u <sub>p</sub>                                      | Particle velocity, DFM model  |
| U <sub>t</sub>                                      | Frictional viscosity  |
| V   | Volume of an arbitrary control volume A <sub>Ω</sub>                    |
| V <sub>∞</sub>                                      | Velocity at free stream   |
| X   | Ratio of molecular viscosity  |

---

|       |  |
|-------|--|
| $Y$   | Off wall spacing                                       |
| $Y^+$ | Unit use to measure off wall spacing                   |
| $Y_v$ | Destruction of turbulent viscosity near wall, SA model |

### Greek Symbols

|               |  |
|---------------|--|
| $\Phi$        | Scalar such as pressure, energy or species concentration |
| $\nu$         | Molecular kinematics viscosity                           |
| $\Omega$      | Arbitrary control volume                                 |
| $\alpha$      | Angle of attack  |
| $\rho$        | Average local density                                    |
| $\phi$        | Shape factor, DFM model                                  |
| $\mu$         | Molecular viscosity of fluid                             |
| $\rho_\infty$ | Density of free stream air                               |
| $\sigma_v$    | Constant   |
| $\tau?$       | Reynolds stress  |
| $\Omega_{ij}$ | Mean rate of rotation tensor                             |
| $\rho_p$      | Density of the particle, DFM model                       |
| $\mu_t$       | Turbulent viscosity                                      |
| $\sigma_v$    | Constant, SA model                                       |
| $t_w$         | Skin friction  |

---

# CHAPTER 1: INTRODUCTION

## 1.1 Background

The Aurora was introduced to the commercial aircraft market in October 2001. This twinjet was designed specifically to serve the emerging regional market. This short-haul, high frequency market demands full-size jetliner comfort, low noise and emissions, low operating costs and high schedule reliability. At 100 seats, the Aurora fits this new market perfectly. The Aurora meets the worldwide need for efficient short-hop service, short-field operations, fast turnaround at airport gates and the ability to sustain 8 to 12 one-hour flights every day. The Aurora Inc. strengthens the product line with a smaller, lighter model optimized for the emerging regional market. It is estimated that the market will require 3,000 aircraft worldwide over the next 20 years [1]. Aurora Inc. is constantly on the lookout for ways to cut down the manufacturing and maintenance cost of these aircraft and to increase their efficiency.

The merger between Mazenda Inc. with Aurora Inc. in 2003 increased efficiency by filling gaps at both companies while at the same time eliminating duplication and redundancies [2]. As a result of the merger, construction and manufacturing costs of all aircraft were revised for improvements in efficiency. One of the components brought into question was the slat door of the Aurora wing. Slat doors in Aurora are used to cover partially the openings that are cut into the leading edge of

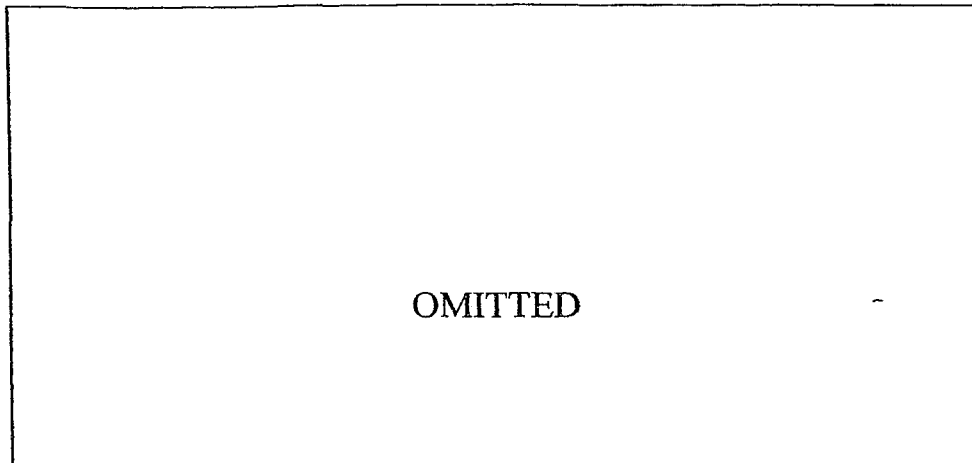
---

the wing once slats are deployed during take-off and landing. Other commercial aircraft produced by Aurora do not include slat doors on their wings. It is important to find the effectiveness of these slat doors on the Aurora since a significant portion of its operational life is spent in the take off and landing configurations. The Aurora spends an average of 17 minutes during take-off from sea level to basic ceiling and 29 minutes during landing from basic ceiling to sea level [3]. According to Master Pilot R. Chaffin's flight logbook, the Aurora spends an average of 50% of its flight time during take off and landing for a flight which takes 1.5 hrs to fly from the Caribbean Islands to Central America [4].

## **1.2 Use of high lift devices on the Aurora aircraft**

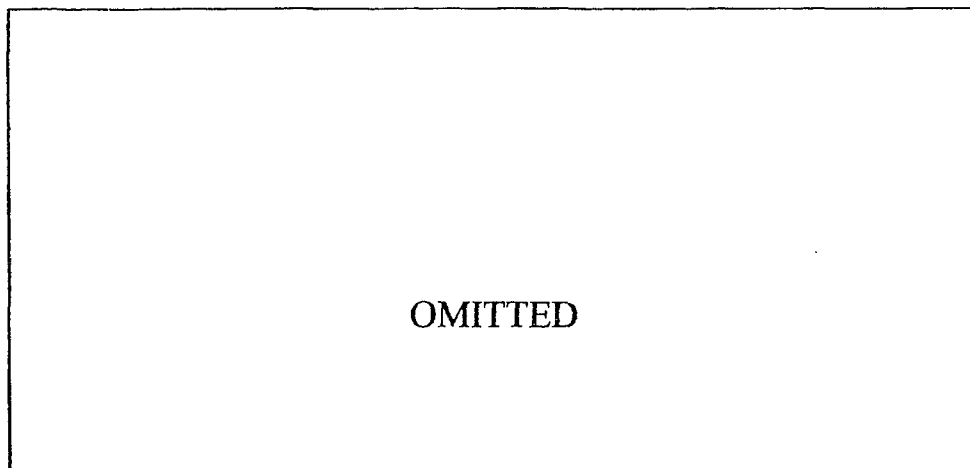
Take-off and landing distances of all aircraft are strongly influenced by their stall speeds. Lower stall speeds require lower accelerations or decelerations and correspondingly shorter field lengths. Increasing the wing area for the duration of take-off and landing can reduce stall speed. This wing area is increased by deploying slats and the flaps using mechanical actuators located at the fixed leading and fixed trailing edges of the wing respectively.

Figure 1.2.1 shows cross sections of an Aurora wing at cruise, take-off and landing configurations. The high lift devices such as the slat and the flap of Aurora are used to increase the lift during take off and the drag during landing and to enhance the boundary layer stability. The slat is located at the fixed leading edge of the wing and the flap is located at the fixed trailing edge of the main wing.



**Figure 1.2.1: Double-slotted flap and slat system of Aurora wing at cruise, take off and landing configurations [5].**

The slat has only two positions, fully extended during both take off and landing and fully retracted during cruise. However, the location and the orientation of the flap will vary depending on the landing and take-off configurations. The maximum flap deflection at landing is  $40^{\circ}$ , while at take-off it is  $20^{\circ}$ .



**Figure 1.2.2: Locations of slat arms and slat arm doors along the half a span of Aurora wing [5].**



---

The leading edge of the slat is heated from the anti-icing bleed air running through a tube located inside the slat. The connection between this tube inside the slat and the fixed wing is provided through the telescopic duct located in-between slat arm number 1 and 2. Aurora uses 5 cable-operated sets of tracks to deploy and retract the slats. Figure 1.2.3 shows one of the track sets and the connection of the cables to the slat arm. The spring-loaded slat door is located just above the slat arm and is shown in dark red. As the slat arm is pulled out using cables, the spring loaded slat door is opened and locked at the door-closed position until the slat arm is pulled back in again. The lobe shape end of the slat arm near the slat pushes the spring loaded slat door as the slat is retracted into cruise configuration. The intent of this door is to close the slat arm cavity when the slats are deployed.

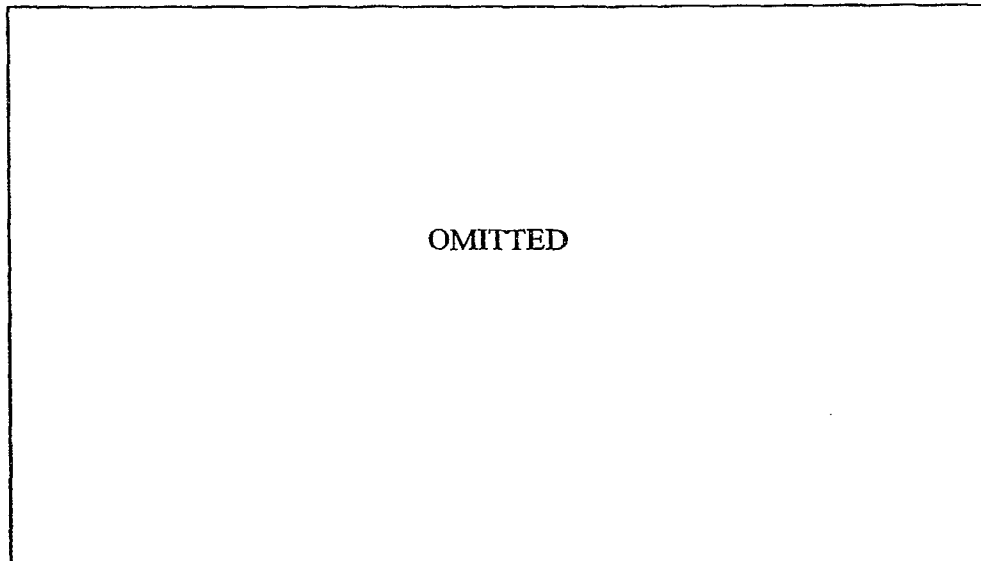


**Figure 1.2.3: Aurora aircraft. Picture just above the right wing shows the mechanism used to deploy the slat during take-off. The slat door is marked in dark red color with black background just above the long slat arm covering the opening [5].**

## 1.3 High lift devices aerodynamics

High lift devices increase performance by effectively increasing airfoil camber increasing wing's wetted surface area. The lift acts perpendicular to the direction of the free stream velocity while drag acts in the direction of the flow. The figure 1.3.1 shows the reference value of the chord, angle of attack and directions of the Drag and the Lift forces with respect to the free stream velocity that will be used in this report for further analysis.

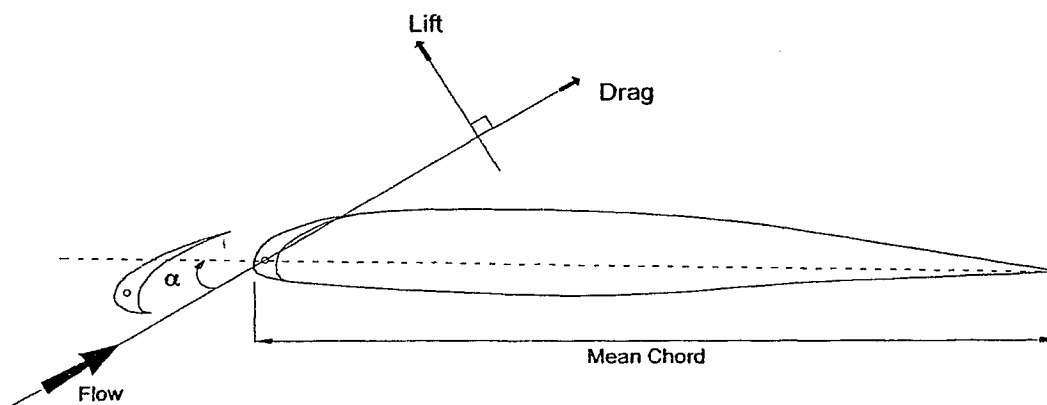


Figure 1.3.1: Definition of reference values used in this report.

Normally both the flap and slat are extended during take-off and landing phases, but the deployment of the flap is not included in the CFD model of the wing to isolate effects of slat/slat arm door.

### 1.3.1 Flap aerodynamics

One of the most time consuming parts of CFD modeling is the mesh generation. One must know the aerodynamic phenomenon around the wing and high lift devices in order to generate an appropriate mesh. A finer mesh is required especially in the areas closer to the wing, in regions

suspected to have viscous phenomenon such as boundary layer development and separation, wakes, and any interactions of such phenomena. The CFD results found in this thesis will not include the effects of flaps but understanding the aerodynamics behind flaps will provide the reader with an overall appreciation of high lift devices if they were introduced in the CFD model. Flap in the Aurora aircraft is located in the wake of the slat arm door and there will not be any significant effect on the slat arm door if flaps were introduced.

Flaps are located at the fixed trailing edge of the wing. They are deployed during take off to increase the lift and drag during landing. This is done by effectively increasing the airfoil camber. The shape of the airfoil camber also changes simply by changing flap angle. The Aurora uses an average flap angle of  $20^\circ$  during take-off and  $40^\circ$  during landing. Figure 1.3.2 shows how flaps can change the lift coefficient ( $C_L$ ) as angle of attack of the aircraft increases from  $0^\circ$  to  $25^\circ$ .

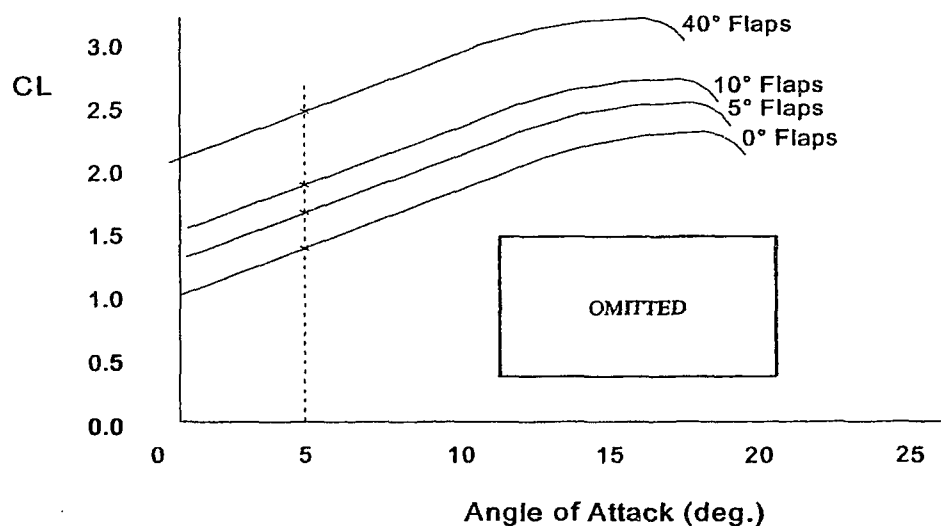


Figure 1.3.2:  $C_L$  vs. flap deflection and angle of attack generated at Mach 0.2 for the DC-9-30 aircraft when slats are retracted.

Figure 1.3.2 shows that flaps increase the lift at a given angle of attack. The  $C_L$  vs. angle of attack plot for the DC-9-30 aircraft will have similar trends as the Aurora aircraft since both the Aurora and DC-9-30 aircrafts have similar flap configurations.

### 1.3.2 Slat aerodynamics

The effect of slats on the total lift of the aircraft is comparatively small compared to the contribution of lift due to flaps. However, slats play a major role in wing aerodynamics by extending the range of attack angles over which the flow over an airfoil remains attached. Slats reduce the pressure peak near the nose by changing the nose camber of an airfoil. The flow close to the lower surface of the airfoil creeps through the opening between the slat and the fixed leading edge and re-energizes the boundary layer on the main airfoil. The new boundary layer formed at the fixed leading edge of the airfoil effectively delays the flow separation on the upper surface of the airfoil, eliminating the detrimental effect of the initial adverse pressure gradient that would otherwise initiate flow separation, especially at higher angle of attacks.

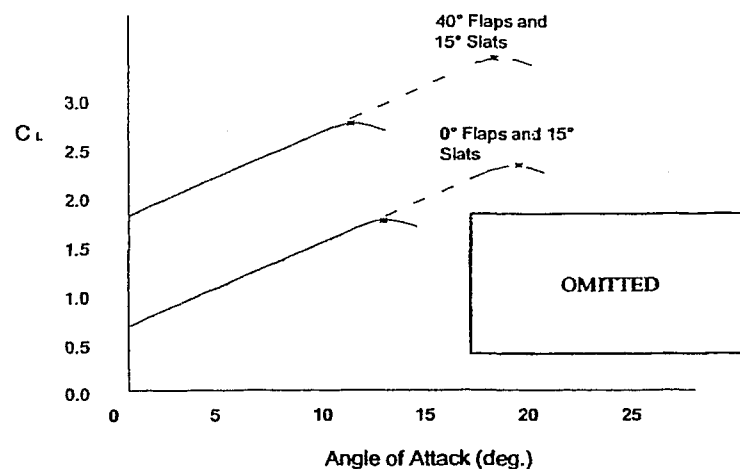


Figure 1.3.3: The effect of slats on the stall angle at 0° and 40° flaps.

Figure 1.3.3 shows several streamlines  $C_L$  to the airfoil and the behavior of  $C_L$  at a range of angle of attacks. This plot also shows the effect of the slat at  $0^\circ$  and  $40^\circ$  of flap and how it delays the stall angles corresponds to the highest  $C_L$ . The solid lines of plot  $C_L$  vs. angle of attack shows plots of  $C_L$  vs. angle of attack from  $0^\circ$  to  $25^\circ$  without slats while the hidden lines represents the same plots when slats are deployed.

## 1.4 Boundary layer phenomena

A flowing fluid can be classified as either laminar or turbulent. Laminar flow moves in non-mixing laminas while turbulent flow is the exact opposite; laminas break up and move in an irregular and random pattern. Characteristics of these two types of flows depend on the history of the flow and the strength of the fluid viscosity. Usually, flow over a shape starts out laminar and becomes turbulent a short distance downstream. This transformation region from laminar to turbulent flow is called the transition region and is found on the external surface of most commercial aircraft.

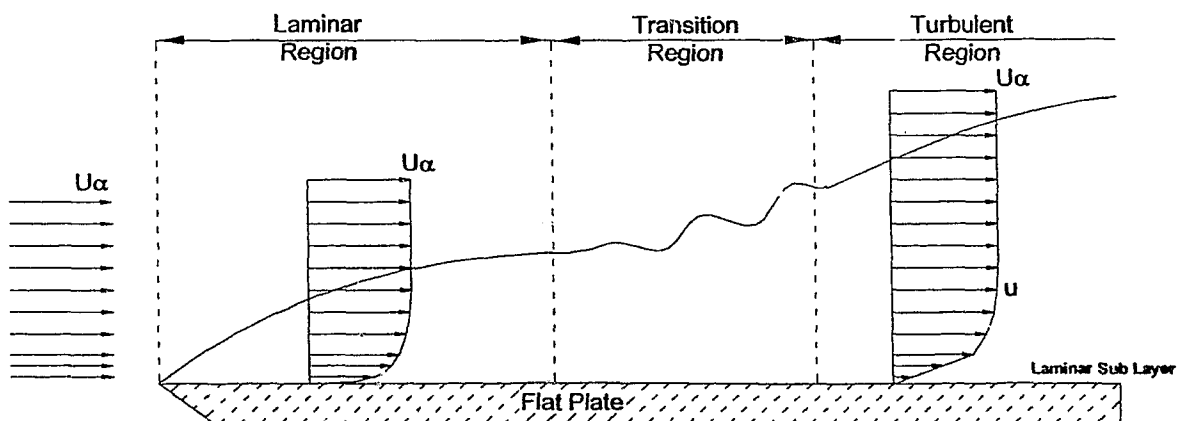


Figure 1.4.1: Boundary layer on a flat plate.

---

Figure 1.4.1 shows the boundary layer over a flat plate. This figure also shows the laminar layer as it becomes turbulent and how the boundary layer grows towards the rear of the plate. At some point the flow actually separates from the body surface. Downstream of this separation point, reverse flow will be found along the surface with the static pressure nearly constant and equal to that at the point of separation.

The boundary layer development described can vary depending on the size, shape and the surface finish of the wall surface, the magnitude of the free-stream velocity, and the properties of the fluid. Variation in these parameters can change the position at which transition or separation occurs. Unlike the flat plate, the Aurora wing has thickness and camber but will nevertheless experience a boundary layer development similar to a flat plate.

### **1.4.1 Laminar sub layer**

The viscous effects on the fluid adjacent to the wall surfaces are dominant and turbulence is almost completely absent in this region. The temperature and velocity in this region can be found using a linear relationship. This behavior of the fluid close to the wall surfaces is very important when modeling boundary layers using CFD packages since most of the turbulence models require a sufficient number of nodes in the laminar sub layer to allow accurate modeling of the log-law behavior throughout the layer.

Figure 1.4.2 shows the velocity profile of a turbulent boundary layer close to a flat plate. The region with a linear velocity profile is defined as the laminar sub layer. The heat transfer in the laminar sub layer is governed by conduction only. The shear stress on the wall can be found by simply dividing the velocity at the end of the laminar sub layer by its thickness and then

multiplying the result by the fluid's viscosity. A laminar sub-layer will be present in the flow over an Aurora wing.

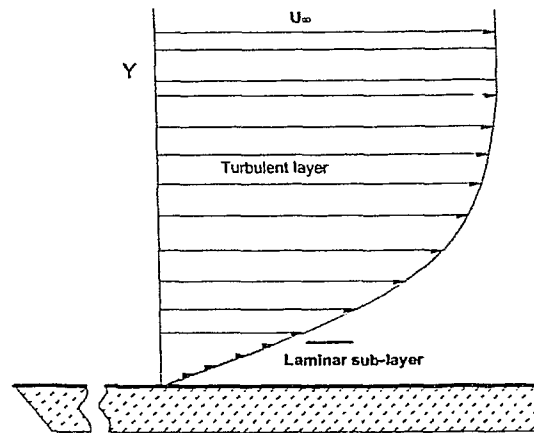


Figure 1.4.2: Close up of a laminar sub layer over a flat plate.

### 1.4.2 Boundary layer interaction and creation of vortices

Interaction between boundary layers and bluff bodies are very important since most external aircraft components can be considered as bluff bodies with flow around them affected by the neighboring parts or by their supports. Aircraft wake vortex formation during approach plays a major role in deciding the separation distances between aircraft. Reducing the separation distance between aircraft during approach will increase the number of sorties avoiding costly delays in busy airports [6] [7]. These vortices are mainly created by the wing tip horseshoe vortices but recent studies using CFD shows the presence of vortices due to the flow traveling upward through the small gap between the slats, especially at higher angles of attack [8].

Studies conducted by Lee and Klewicki examined the flow around a circular cylinder embedded in a single boundary layer, shear-wake and combination of boundary layer and shear-wake [6]. The results found using smoke injection visualization and the velocity calculations using a hot wire probe, showed that there are vortices present in all three cases.

The results confirm that vortices are present not only when the boundary layer is separated due to the adverse pressure gradient above a wall surface but also when the boundary layer and bluff body interact, and when interaction between shear layer and bluff body and the interaction of inflection boundary layer and bluff body create vortices with the specific orientation as shown in figure 1.4.3.

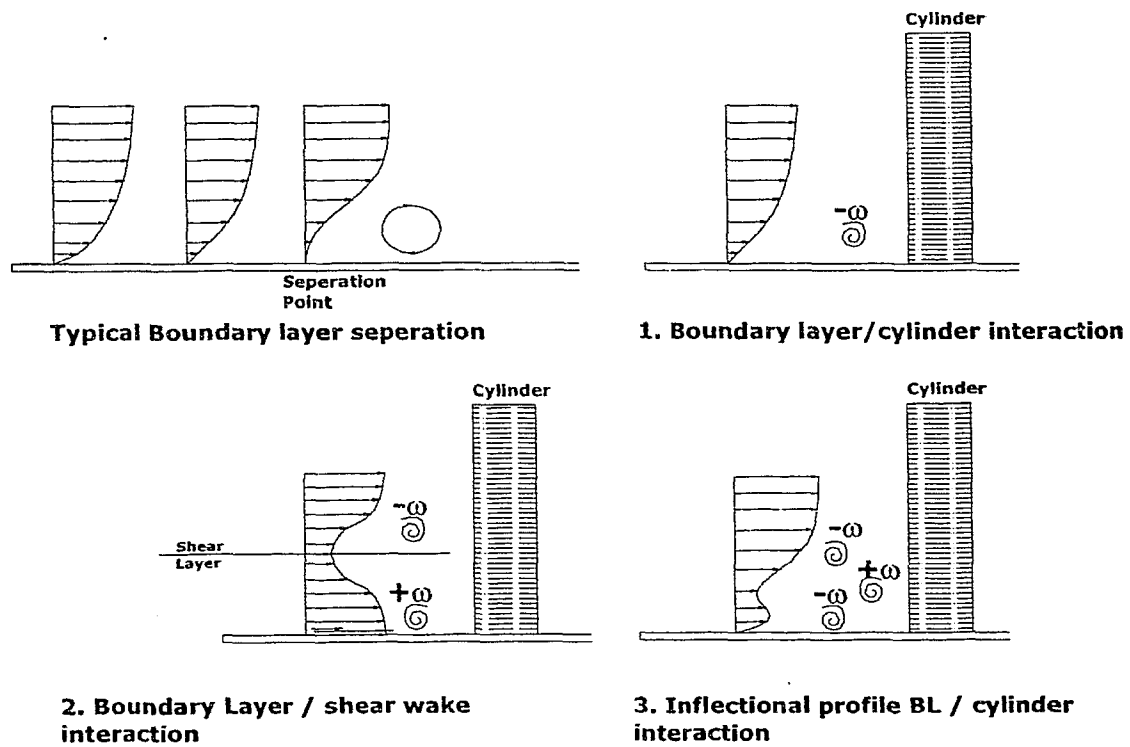


Figure 1.4.3: Interaction of boundary layer with the cylinder and formation of horseshoe vortices [7].

All these flow scenarios shown in figure 1.4.3 are present in flow around slat arm at high lift configuration. The separation of a boundary layer is present on the upper surface of the main airfoil at higher angles of attack. The boundary layer that forms over the slat sees the fixed leading edge of the wing as a bluff body. The shear wake emanating from the fixed trailing edge of the wing and the flaps are similar to the shear layer and cylinder interaction. The wake of the upper



---

edge of the slat has an inflectional profile, which interacts with the fixed leading edge of the wing similar to interaction of the inflectional profile/ cylinder in figure 1.4.3. The Aurora model needs to have a fine mesh around the areas where boundary layers interact with bluff bodies to capture all of these 3 situations.

### **1.4.3 Angle of attack and boundary layer separation**

Figure 1.4.4 shows the separation of a boundary layer on an aircraft wing as angle of attack increases. The separation point moves slowly forward as angle of attack increases from  $0^\circ$  to  $15^\circ$  and remains relatively close to the trailing edge of the airfoil. At  $15^\circ$  this airfoil creates maximum lift, beyond this angle of attack the boundary layer separation point jumps forward, reducing the lift and increasing the pressure drag. The angle that corresponds to maximum lift is called the stall angle the critical angle. The turbulent wake increases in size slowly as the angle of attack increases from  $0$  to  $15^\circ$  and beyond the critical angle it increases rapidly covering the entire upper surface of the airfoil.

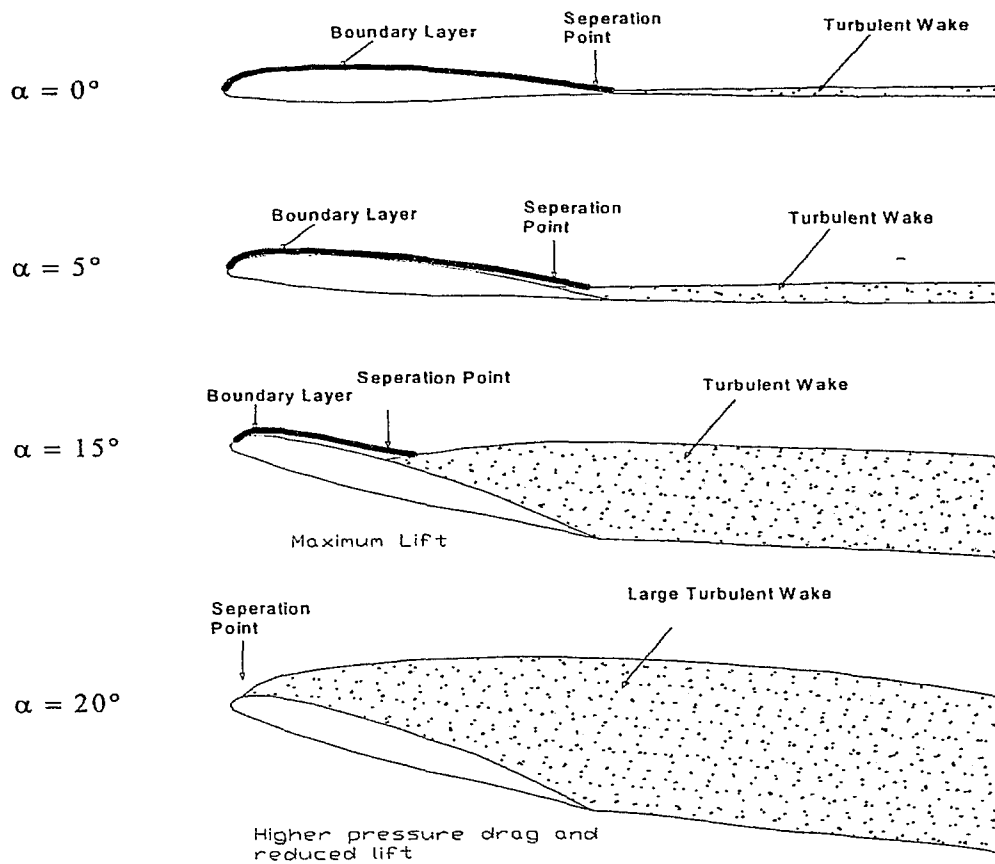


Figure 1.4.4: Angle of attack vs. flow separation.

The main wing of the Aurora also has the same performance characteristics of the 2D airfoil but the 3D nature of the real wing will affect the effective angle of attack due to its inherited twist and tapered ratio. The mesh of the Aurora wing needs to have a finer mesh throughout the whole upper surface of the wing and significant off wall spacing in the boundary layer to capture the boundary layer separation [9].

## 1.5 Reynolds number effect

A commonly held view in aerodynamics is that an increase of Reynolds number will increase the aerodynamics properties of an airplane such as  $C_L$ ,  $C_D$  and etc. [10]. Wind tunnel testing of the DC-10 aircraft done in low Reynolds number to simulate the cruising conditions by Lynch of Douglas showed that this view does not hold all the time [11]. In-flight condition Reynolds number tends to be higher than a wind tunnel test resulting a thicker boundary layer.

Figure 1.5.1 shows the progressive work done by McMasters and Mack on several Aurora 700 series aircraft from 1950 to present. It shows how  $C_{Lmax}$  in wind tunnel and in-flight testing changes at different Reynolds numbers.

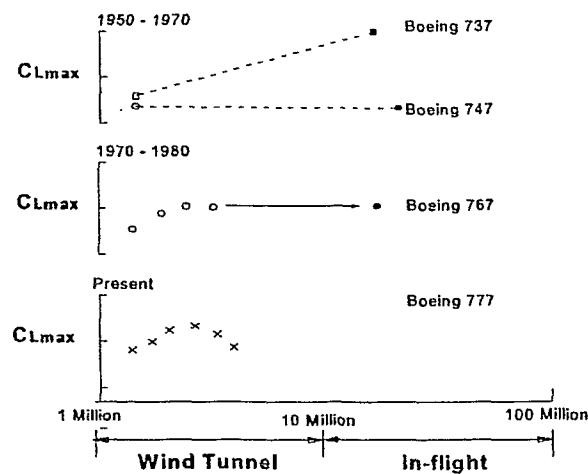


Figure 1.5.1: Reynolds number effect on  $C_{Lmax}$  for several Aurora aircraft and the difference between wind tunnel and in-flight testing as per McMasters and Mack. Not to a scale [12].

Present wind tunnel studies for Aurora 777 aircraft shows that  $C_{Lmax}$  increases as Reynolds number increases and reduces as the Reynolds number further increases beyond a certain value. This surprising behavior in  $C_{Lmax}$  was initially explained by Woodward, et al. [13]. According to their results at low Reynolds numbers, the boundary layer is initially laminar, and then transitions in a classical two-dimensional sense. At higher Reynolds numbers the flow on the attachment line

---

is initially turbulent, and this results in a thicker boundary layer that tends to separate more rapidly, leading to lower values of maximum lift [14].

## **1.6 Aircraft corrosion due to contaminants around the airports**

The annual (1996) corrosion cost to the U.S. aircraft industry is estimated at US \$ 2.225 billion, which includes the cost of design and manufacturing at US \$ 0.225 billion, corrosion maintenance at US \$ 1.7 billion and downtime due to corrosion at US \$ 0.3 billion [15]. These figures show how important is to take measurements during manufacturing process to reduce the corrosion in aircraft parts that can occur during an average life span of an aircraft.

The acidity of the environment around airports can significantly affect the corrosion behavior of most aluminum alloys use in aircraft. A survey conducted by Baboina R. [16] showed that the corrosion in new vehicles parked in airport parking lots experienced localized corrosion, such as crevice corrosion, after a short time on the lot. This corrosion compared to the type of corrosion given by vehicles driven in the city. He concluded that the exhaust emissions from the aircraft jet engines attributed to localized corrosion, which is similar to that observed down-wind and close to volcanic activity.

An unfortunate accident that occurred in the past with Aurora 700 series aircraft shows how important it is to take necessary measurements to reduce corrosion in their jet line series. In October 1992, an EL AL 747 freighter crashed in Amsterdam, killing all four people on board and over 50 people on ground. This accident occurred because of a broken fuse pin that was designed to break when an engine seized in flight, and resulted in the engine separating during landing. A possible reason for breakage of the fuse pin is corrosion pits and fatigue. These corrosion pits usually form via a lack of passivity, surface discontinuities, or insufficient inhibitor coverage [16]

---

[17].

Corrosion was also found in the bonded area of the skin plates of CP-140 Aurora aircraft. According to Capt Giguère, S. [18] cause of this corrosion was believed to be water in the grease from a global positioning system (GPS) antenna. He believed that water penetrated through cracks in the seal surrounding the GPS antenna resulted in crevice corrosion damaging two portions of the CP-140 structure. These unfortunate incidents in the past show how important it is to find how well the slat doors can prevent the penetration of contaminants that can initiate the corrosion of parts inside the wing through the opening located at the fixed leading edge of the wing. It is also important to see how long these contaminant agents will reside inside the slat door cavity of the Aurora aircraft since the presence of the slat door will affect the residence time. Less residence time will give less chance of residual material left behind.

## **1.7 General approach to the problem**

### **1.7.1 Previous studies**

A wind tunnel testing of the Aurora wing and slat arm configuration was done by Craig [19] at Ryerson University to find whether the removal of the slat arm doors on the fixed leading edge of Aurora wing caused significant change to the aerodynamic characteristics of the wing. Figure 1.7.1 shows a picture of Craig's scaled down model. The model was built using balsa wood without the inherited tapered-ratio, sweep angle and the dihedral angle of the Aurora wing.

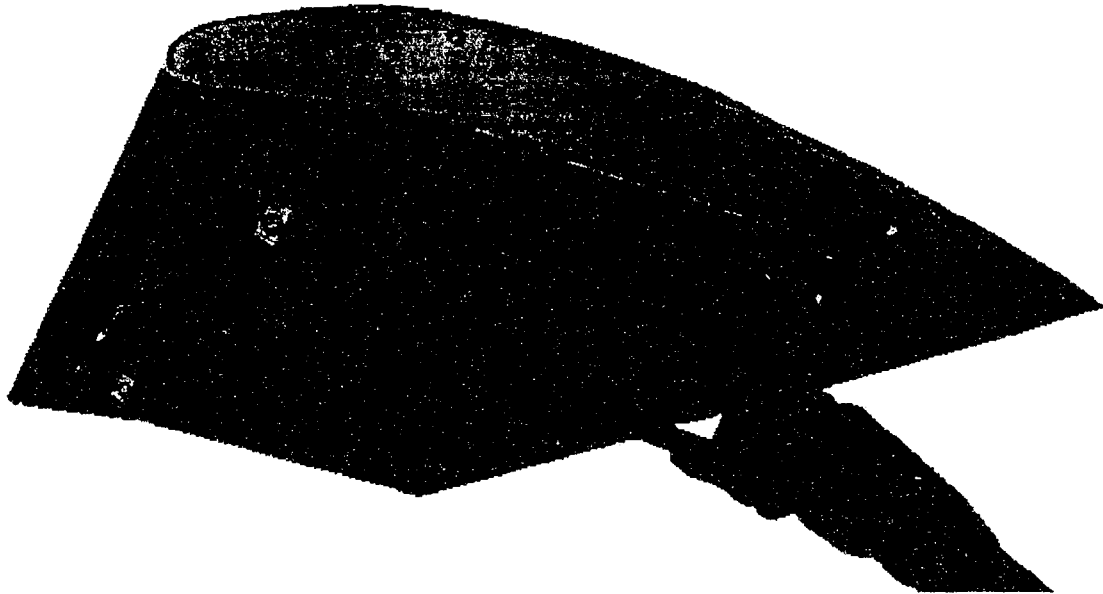


Figure 1.7.1: Balsa wood model of Aurora wing and slat configuration built by Andrew Craig. [19]

The results found by Craig showed no appreciable change in lift or drag. He concluded that this was due to the problems involved in scaling the model with the wind tunnel. He recommended that a larger more sophisticated wind tunnel with more adaptable mountings to balance the slat and wing set-up would have given better results, allowing investigation of sweep angle, tapered-ratio and the dihedral angle on the scaled model [19]. The wind tunnel model in figure 1.7.1 also showed that the size of the slat arm door was small in comparison to the overall wing, and this would be difficult to get quantitative results using wind tunnel testing. Not many aircraft have slats arm doors in their wings. The slat-arm doors in Aurora are unique and few studies have been done. Previous CFD studies done by Perera, S. with Aurora wing and slat configuration showed that there was a significant effect on wing lift and drag due to the slat arm doors. These results were found using a simplified inviscid CFD model [20].

---

## **1.8 Thesis objectives**

The main objective of this thesis is to determine the efficiency of the slat arm door of a selected section of Aurora wing via a viscous flow simulation. The efficiency of the slat door can be determined through the following objectives:

1. Investigate the effect of the slat door on the wing lift and drag for different angles of attack.
2. Investigate the effect of the slat door on the wing's stall angle as measured by boundary layer separation.
3. Investigate the effect of the slat door on the turbulence that may cause the flow over the wing to separate prematurely.
4. Investigate how rapidly contaminants are cleared from the slat arm compartment with and without the slat arm door.

## **1.9 Thesis overview**

The thesis will provide a detail description of the studies done by the author to find the effect of a slat arm door in a commercial aircraft using numerical methods.

Chapter one explains the use of slat arm doors in Aurora aircraft during take off and landing configurations. This chapter also provides a brief description of the high lift devices use in commercial aircraft and aerodynamics phenomenon behind them.

Chapter two of the thesis gives a summary of the literature review done by the author. This chapter provides details about the use of CFD methods in the aerospace industry and the important results found by individuals that are related to the thesis. This chapter also provides the validation of FLUENT for a similar problem as the one under consideration.

---

Chapter three provides a detailed description of the steps needed to generate a numerical grid of the Aurora aircraft, using the program GAMBIT. This chapter covers the strategies adopted in the mesh generation process to reduce the size of the mesh and the time required to solve the problem.

Chapter 4 provides a brief introduction to different numerical techniques used in CFD. This chapter also describes the importance of selecting the correct model and modeling techniques in CFD to model the Aurora and slat arm configuration.

The theory section gives the equations used in FLUENT to model the problem under consideration. This Chapter 5 includes the equations of conservation laws, State equation, equations in Sparlart-Allmars turbulence model and the equations used in discrete phase model uses to find the contaminants inside the slat arm door cavity.

The results found in the numerical analysis of Aurora wing and slat configuration is provided in chapter 6. These results show the effect of fuselage on the wing, comparison of total lift and drag of slat door closed and opened models, comparison of surface pressure distribution, vortex shedding, surface shear stress distribution and the dispersion of contaminants in the slat arm compartment.

Chapter 7 gives the executive summary of the results found, conclusions and the recommendations made for future challenges.



---

## **CHAPTER 2: USE OF CFD IN AEROSPACE ENGINEERING**

### **2.1 Why CFD**

Computational Fluid Dynamics (CFD) is a powerful tool, which combines fluid mechanics theory, applied mathematics and state of the art computer power [21]. This tool can be used in the design of aircraft and to find the aerodynamic effects of existing components in order to reduce the time and the cost for manufacturing, operation and maintenance.

This CFD technology emerged in the late 1960 and started expanding into the aerodynamics community as the speed and the memory of computer power increased. The aerospace community has successfully used CFD in the design and development of aircraft for a several years now. According to Mavriplis [22], CFD is now a principle aerodynamic technology along with wind tunnel testing and flight-testing.

CFD can also be used to find the residence time and the trajectories of particles in and around aircraft and crevices like the slat arm door compartment in Aurora aircraft. Winters W.S. and Cheniweth [23] used CFD to model the dispersion of biological agents into a 3D living space. The results showed that particle trajectories and flight time are influenced by several factors and it would be difficult to anticipate using "common sense" or lower fidelity models.

---

## 2.2 Use of CFD in aerospace industry to model high lift systems

Calculating the viscous flow over a high-lift system of a commercial aircraft is difficult because of flow phenomena such as boundary layer separation, shock-boundary layer-interaction and multiple elements merging of confluent wakes [24]. Despite the difficulties in modeling high lift systems using CFD, significant work has been done to simulate 3D high lift flow fields using full Navier-Stokes solutions.

Studies done by the Aurora Company, Long Beach and NASA Ames research center successfully used the OVERFLOW code, which uses Reynolds Average Navier Stokes method (RANS) to find the efficiency of externally blown flaps and the effect of nacelle strakes around the engines and to see how nacelle strakes affect the wake vortices [25]. The CFD code OVERFLOW predicted excellent results up to the maximum lift coefficient. This code also captures successfully the vortices generated by nacelle strakes and predicted how strakes improved the health of the boundary layer on the wing upper surface by the counter rotating and down washing vortices created by the inboard slat-edge.

## 2.3 Advantages of using CFD methods over wind tunnel testing

Wind tunnel testing used to be the only method of testing aerodynamics models in the past. According to Marvipilis F. most wind tunnel testing is done at the wrong Reynolds numbers [8] due to the restrictions of wind tunnels such as wind tunnel operating speed, size of the test section and difficulties in reducing wind tunnel wall and support structures effects. Use of a wrong Reynolds number in wind tunnel testing will yield inaccurate prediction of flow phenomenon such as  $C_{Lmax}$  [26].

The most accurate results are achieved only by in flight-testing. These types of testing are very expensive and a few companies in the world can afford to perform them. Because of increasing computer power and speed, CFD methods are becoming very popular and economical ways to test aerodynamic models.

The cost of wind tunnel testing is expensive compared to the CFD testing, but cheaper than obtaining the massive amounts of data needed for detail design [26]. According to Karpynczyk, J. [27], one has to spend an average of Can \$ 84-140K to build a wind tunnel with 4 feet by 4 feet test section, compared to the price of a commercial CFD software package, which would cost around Can \$ 30-50 K for a duration of one year [28]. There is no cost involved to maintain an in-house CFD code for a company other than the initial cost involved in purchasing the code, unlike the wind tunnel which is relatively expensive to set-up, operate and to maintain.

The operating velocity range and the data acquisition time during wind tunnel tests are limited. Some supersonic wind tunnels can operate for only for few seconds, and all the necessary results must be captured during this limited time. In CFD methods, the user can select any type of initial condition to match the physical situations that are available within the software, or the user can write his/her own subroutine to introduce necessary initial conditions. The CFD user can capture the results at his/her convenience since the results can be generated at any time once solutions are converged.

The latest wind tunnel calibration techniques and boundary layer control systems yield better results today than one could achieve in the past. Boundary layer control methods in wind tunnel testing such as boundary layer suction can reduce the thickness of the boundary layers during wing tunnel testing, simulating the in-flight flow even at lower Reynolds numbers [29]. But the interferences due to wind tunnel walls and support mountings are still unavoidable.

---

### 2.3.1 CFD modeling of a wind tunnel

CFD was successfully used in the past to model both in-flight and wind tunnel experiment settings. NASA Ames created CFD models of a wing placed inside a wind tunnel to include the wind tunnel walls and boundary layer control suction holes to simulate a wing placed inside a wind tunnel and a wing at in-flight condition. The results found in these two CFD simulations were compared with experimental results.

Comparative studies of all four cases showed that results achieved for CFD simulation of free air always over predicted the  $C_L$  compared to the wind tunnel CFD model. The  $C_{L_{max}}$  of the CFD simulations for both the wind tunnel and the free air models always under predicted the corresponding experimental values by about 3% [26]. These results confirmed that CFD methods can give reasonably good results and this, is a valid method to predict the flow phenomenon around external aerodynamic components.

Similar studies were done by the author using FLUENT to simulate a wing with the same Aurora aircraft airfoil placed inside a wind tunnel using wing support mounting and a wing placed in free air as shown in figure 2.3.1 and 2.3.2 respectively. Wall boundary conditions were used on the upper and the lower surfaces of the Wind Tunnel model while the left and the right side with respect to the inlet were modeled using a symmetry boundary condition to isolate the effect of the upper and the lower wall surfaces of the wind tunnel on the scaled-down model. The wind tunnel shaped model has a cross section of  $1 \times 1 \text{ m}^2$  and a length of 10m. The model used in the wind tunnel is scaled down by a factor of 5, and has a wing chord of 0.5 m. This model is placed at the middle of the wind tunnel as shown in figure 2.3.1.

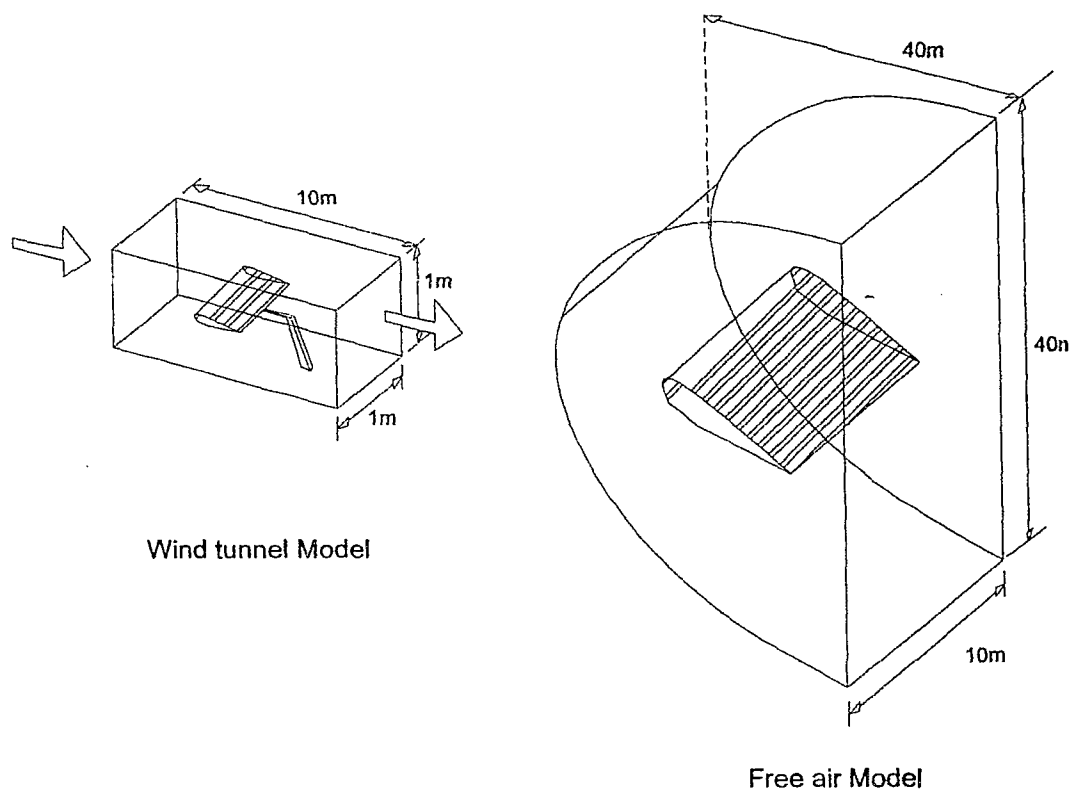


**Figure 2.3.1: Wind tunnel and Free air models.**

In the Free Air model, the wing chord spans 10m from the left side symmetry boundary to the right symmetry boundary compared to the positive flow direction of the far field boundary. The far field boundary is placed 20 chords away from the main wing. Both models were run at 0.21 Mach free stream velocity, angle of attack of 0 degrees and at Reynolds Number of 4 million to yield a valid comparison of the data obtained from wind tunnel constrained modeling and an equivalent free stream simulation.

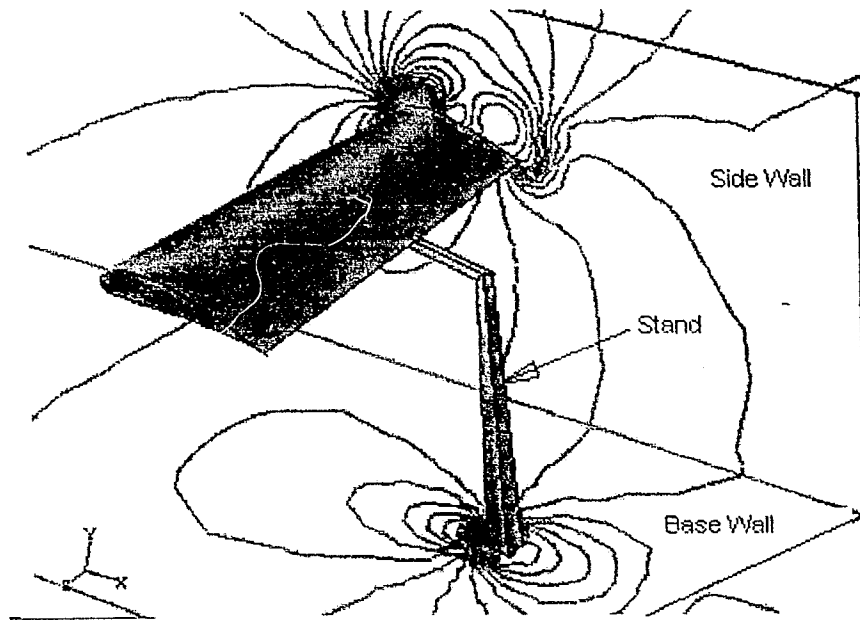


Figure 2.3.2: Pressure contours of Wind Tunnel shaped model.  $M=0.21$  and Reynolds number of 13.9 million based on the mean chord.  $\alpha = 0^\circ$ .

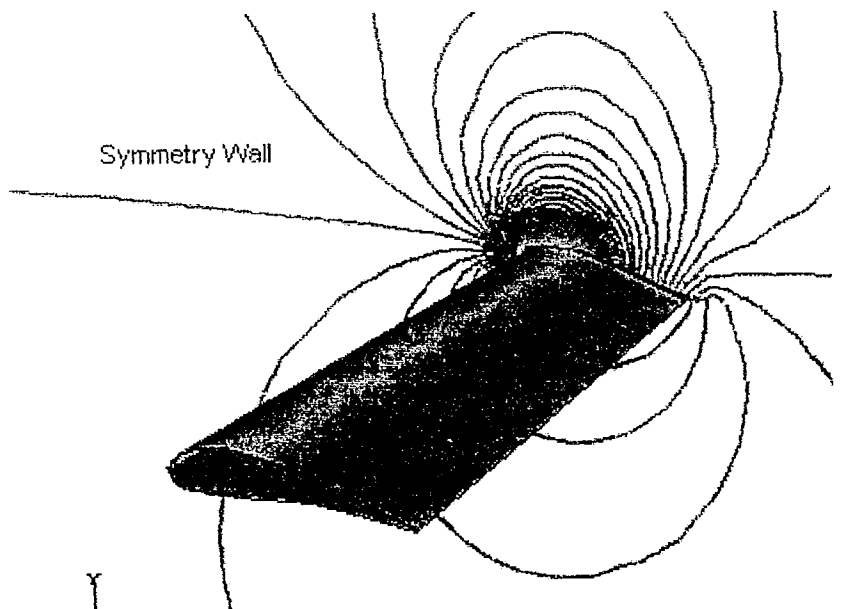


Figure 2.3.3: Pressure contours of free air shaped model.  $M=0.21$  and Reynolds number of 13.9 million based on the mean chord.  $\alpha = 0^\circ$ .

Figures 2.3.2 and 2.3.3 show pressure contours of the models placed inside a wind tunnel and free air respectively. These computational models were built using GAMBIT and solved using FLUENT.

The main purpose of this comparison is to find the effect of the wind tunnel and the support on the wing performance and to compare the values of  $C_L$  and  $C_D$  of these two models. Figure 2.3.2 clearly shows the effect of the wall and the wing supports on the Wind Tunnel model on pressure contours compared to the Free Air model. In the free air model, contours are not disturbed since the far field boundary is placed 20 chords away from the wing compared to the wind tunnel model, where it is a place only 5 chords away from the wing. The free air has  $C_L$  of 1.53 and  $C_D$  of 0.03 compared to the  $C_L$  of 1.43 and  $C_D$  of 0.06 of the wind tunnel model. These two values shows that the there are significant effects on the wind tunnel walls and the supporting mountings of the wind tunnel model on both  $C_L$  and  $C_D$ . The wind tunnel model under predicts  $C_L$  by 6.50% and over predicts  $C_D$  by 84.30% when compared to the free air model since wind tunnel models in CFD are not practical, due to the need for correction confirming free stream configurations in CFD are clearly the preferred method.

## 2.4 Validation of CFD codes

There are a lot of CFD codes available for use. Validations of these codes are very important with milestone problems in CFD before applying them to for real life problems. Most of the CFD code writers validate their CFD codes with standard problems such as external flow around cylinders and flat plates. But validation of a CFD code with known problems of aircraft design provides valuable information about its features and limitations in solving problems for the aerospace industry.

A competition held by the CFD Society of Canada in 1996, using a two-dimensional multi-element high lift airfoil had allowed many aerospace companies and institutions in CFD to compare and validate their in-house codes against the other CFD codes in the aerospace industry. An experimental test Case A-2 in the AGARD Advisor Report No 303 with Multiple Element Airfoil was used as the test model. The results found using in-house codes of Aurora, NASA Ames and NASA Langley and U of T were compared against the experimental data provided by the AGARD, which were presented at the Fourth Annual Conference of the CFD Society of Canada. Comparative studies of these codes revealed that incompressible Navier-Stokes codes produced better results at lower angles of attack compared to the compressible Navier-Stokes codes. It was also found that compressible Navier-Stokes codes produced better results compared to the incompressible Navier-Stokes codes at higher angles of attack but compressible codes were almost an order of magnitude slower than the incompressible codes [30] [32].

## **2.5 Testing the capabilities and limitations of FLUENT**

The Multi-Element airfoil shown in figure 2.5.1 represents a typical aircraft take-off configuration. The slat of the Multi-Element-Airfoil is located at 12.5% chord from the airfoil fixed leading edge with  $25^{\circ}$  deflections and a single slotted flap at a deflection of  $20^{\circ}$ .



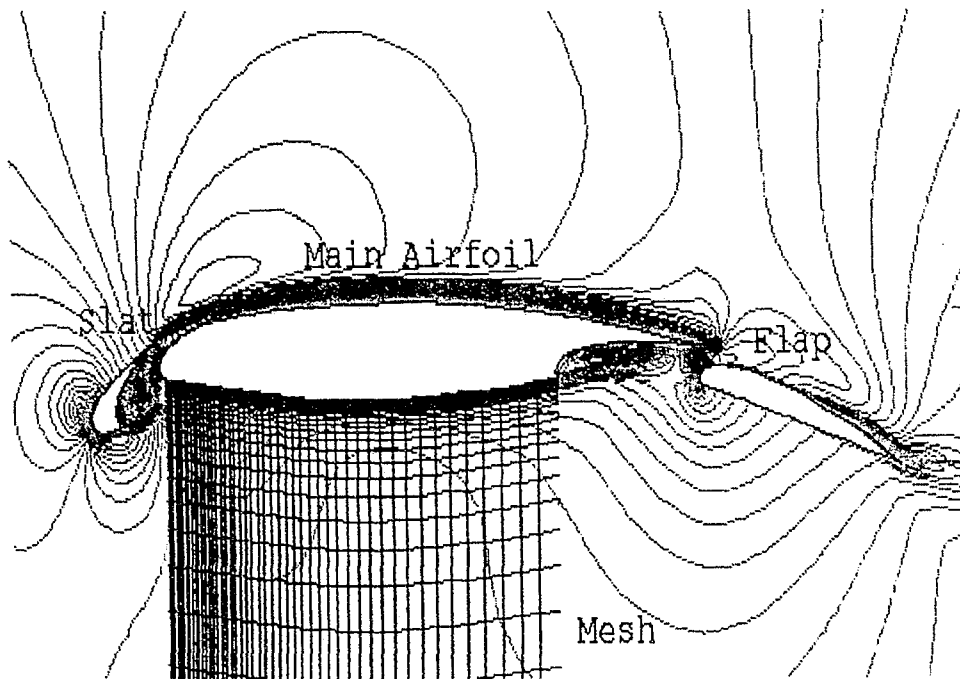


**Figure 2.5.1: Velocity contours of the multi element airfoil achieved using FLUENT at  $M_\infty=0.197$  and  $\alpha=4.01^\circ$ . A selected section of a mesh below the main airfoil shows how mesh is stretched in the 2D domain.**

A 2D model of the Multiple-Element Airfoil was generated using the vertices given by the Case A-2 of the AGARD Advisory report No 303 [30]. A rectilinear surface mesh was created using the GAMBIT™ grid generation software placing more nodes close to the wall surfaces of the airfoil and fewer nodes in the far field boundary. A structured mesh was generated making sure there were enough nodes close to the wall surfaces to model the boundary layer.

The figure 2.5.2 compares the coefficient of pressure versus percent chord distance from the leading edge of the slat of the Multi-Element airfoil found using FLUENT with published experimental results under the same boundary conditions, Mach number of 0.197 (free stream), Reynolds Number 14.9 million (based on the chord) and the angle of attack of  $4.01^\circ$ .

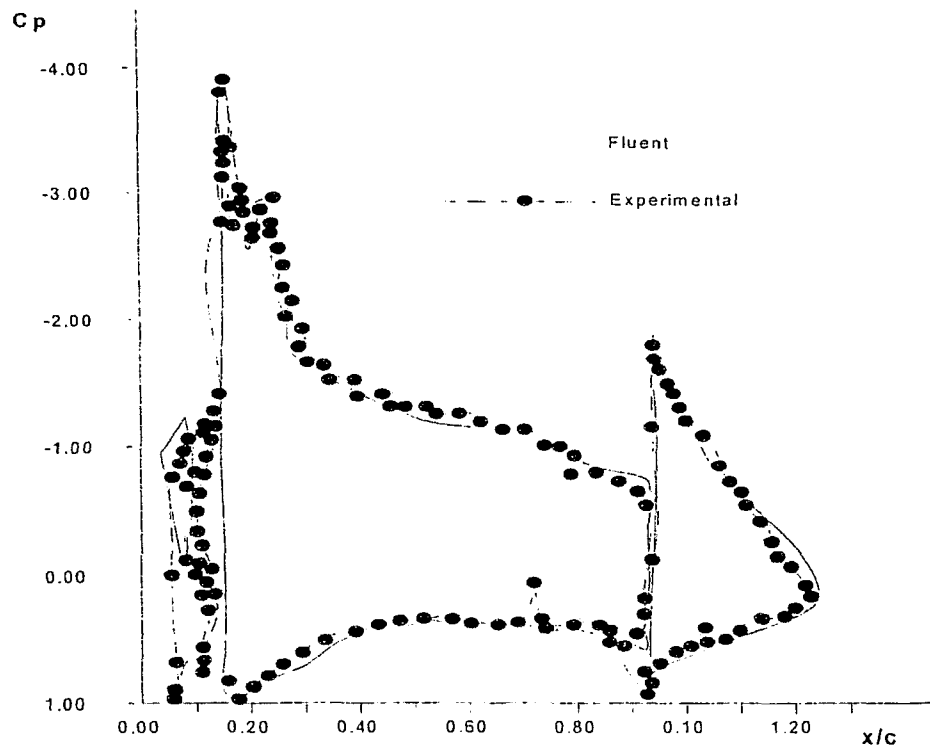
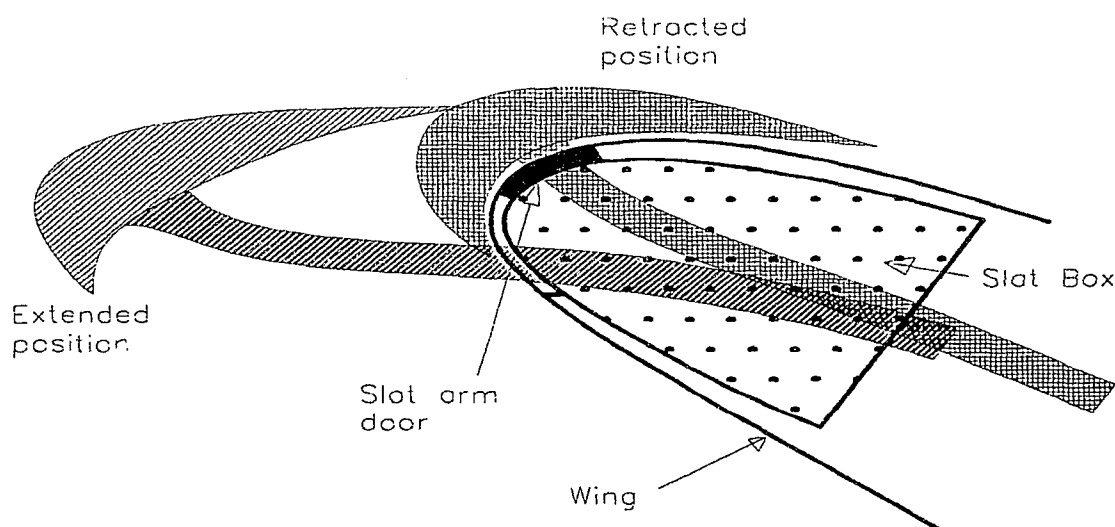


Figure 2.5.2: AGARD multi element airfoil and static pressure distribution found using FLUENT<sup>TM</sup> for  $M_\infty=0.197$  and  $\alpha=4.01^\circ$ .

These two graphs have exactly the same trends as the actual  $C_p$  vs. percent chord presented in the conference. The  $C_p$  at the suction peak for both Experimental and CFD analysis using FLUENT were found at  $x/c = 0.18$  location with same values of  $C_p = -4.00$ . The results found using FLUENT also showed the presence of local flow separation and mixing of wakes and boundary layers from the airfoil elements. These flow phenomenon, are considered to be difficult to model practitioners of CFD in aerodynamics. These results show that FLUENT<sup>TM</sup> provided excellent results for the test case and would be an ideal candidate for the Aurora wing and slat arm configuration problem.

## CHAPTER 3: MESH GENERATION

The shape and features of the Slat-Arm; Slat-Door and the section of Aurora wing are all represented in the numerical model. Figure 3.1 shows a section of Aurora wing made available to the researcher. The figure shows both retracted and extended positions of the slat. The slat-Arm of this model is built using a "T" shape beam, which has a radius of curvature of 4 ft (0.902 Chord). The slat is deployed and retracted using pulleys and cable system located at the front section of the main wing. This is enclosed in a small compartment (Slat Box), which extends 15 inches (0.113 C) into the main wing from the fixed end wing tip.



**Figure 3.1.1: Aurora wing and slat configuration. Detailed model provided by Aurora Toronto showing both retracted and extended positions of the slat.**

---

The section of the Aurora wing was given to the author as a detailed CAD drawing in the form of an IGES file. The drawing consisted of both the retracted and extended positions of the slat even though the computational model will simulate only the extended position. The retracted drawing of the slat arm was removed from the main model once it was imported to the mesh generation software making sure that all the necessary details were captured in order to generate the best computational model possible.

There are very good mesh generation software packages available today such as GRIDGEN, ICEMCFD and GAMBIT. GAMBIT is the preprocessor for FLUENT and it allows the user to construct and mesh models through a graphical interface (GUI). The process use to create the computational domain in GAMBIT is similar to many other Mesh generation software in the market. The steps followed to create the computational domain of the model can be summarized as follows.

1. Importing of geometry and mesh information (IGES file)
2. Creation of geometry
3. Creation and refinement of the mesh
4. Assignment of zone types and exporting the model as a mesh file.

### **3.1 Import of geometry and mesh information**

GAMBIT imports models done in ACIS, Parasolid, IGES, STEP and CAD files [32]. The model given to the author from Aurora was in IGES format and the length units were in inches. This model was imported into GAMBIT with 1 to 1 scale using the spatial option in GAMBIT without virtual cleanup. This spatial option specifies the generic translator to produce only real volumes compared to the native option, which can produce either real or virtual geometries.

GAMBIT uses the ACIS modeling techniques when creating or manipulating volumes. This modeling technique requires a high degree of tolerance and accuracy in data, which describe the volumes and their connectivity. The volumes, which satisfy the ASCII tolerances, are defined as real volumes and the others as virtual volumes. It is convenient to merge real volumes and mesh them compared to the virtual volumes especially when one has to modify the provided geometry. The virtual clean up technique in GAMBIT allows the author to clean up some of the geometry by connecting disconnected vertices and edges and merging very short edges with longer adjacent edges in order to facilitate the meshing. The model of Aurora wing and slat section given to the researcher by Aurora Ltd. has entities that were poorly connected and unnecessary vertices, edges and faces that were not required in generating a 3D model. These unnecessary geometric entities can be automatically deleted during importing process to reduce the time and the frustration of deleting them after they were imported into the mesh generation software. The GLOBAL tolerance value in GAMBIT is  $10^{-6}$  with the possible range of the model from  $10^{-5}$  to  $10^4$  units [32]. The wing chord of the model provided by Aurora is approximately 10 ft with the smallest length for this project, the spacing between the Slat-Arm and the frame of the opening at the leading edge of the wing is at approximately 0.01 inches. The biggest and the smallest dimensions are well within the range of GAMBIT geometric tolerances otherwise user will need to change the default tolerance values before importing the model into GAMBIT.

### 3.2 Creation of geometry

Aurora has a rectangular wing, which spans 93 feet and 4 inches. Figure A1 in the appendix shows the general dimensions of Aurora aircraft. Only a section of Aurora wing was given to the author due to proprietary reasons. This section of the initial model is shown in figure 3.2.1 in solid

red color, which has a mean chord of 132.96 inches. The cut off section of the wing given to the author is located 199.75 inches from the root chord of the main wing.

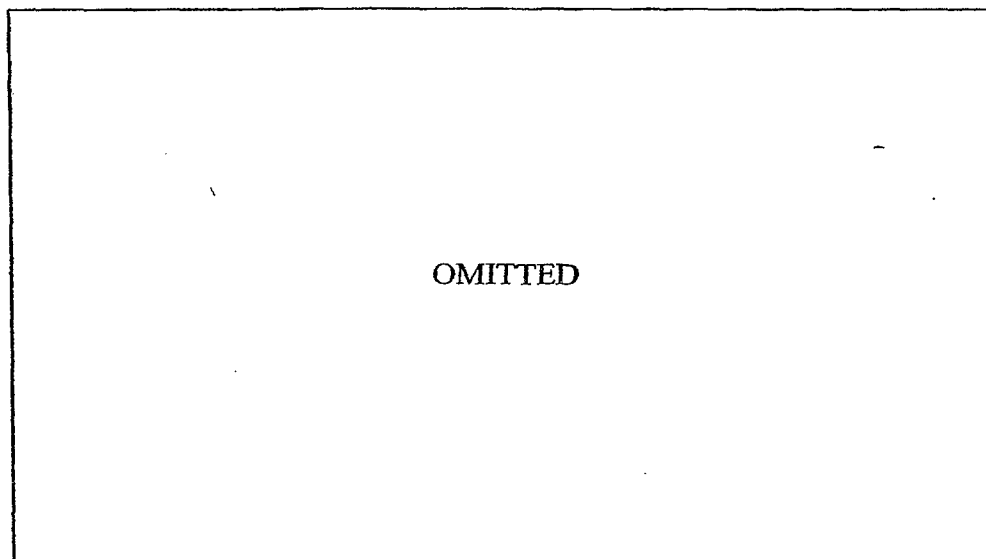


**Figure 3.2.1: Top view of Aurora aircraft. The marked solid section shows the extent of the model given by Aurora and the section with lines running diagonally shows the top view of the regenerated model, using GAMBIT.**

The given section of the Aurora wing and slat configuration by Aurora Ltd. was later extruded by five times of the original width (22 inches X 5) towards the tip and the root of the main wing since the original model was only 22 inches width which is small when compared to the mean wing chord of the given section. The extrusion of the wing also allowed the researcher to introduce symmetry boundary conditions on the tip and the root ends of the extruded sections and to place the far field boundary conditions far from the wing, where the since free stream conditions are imposed. Figure 3.2.2 shows the extruded model of Aurora wing and slat configuration.

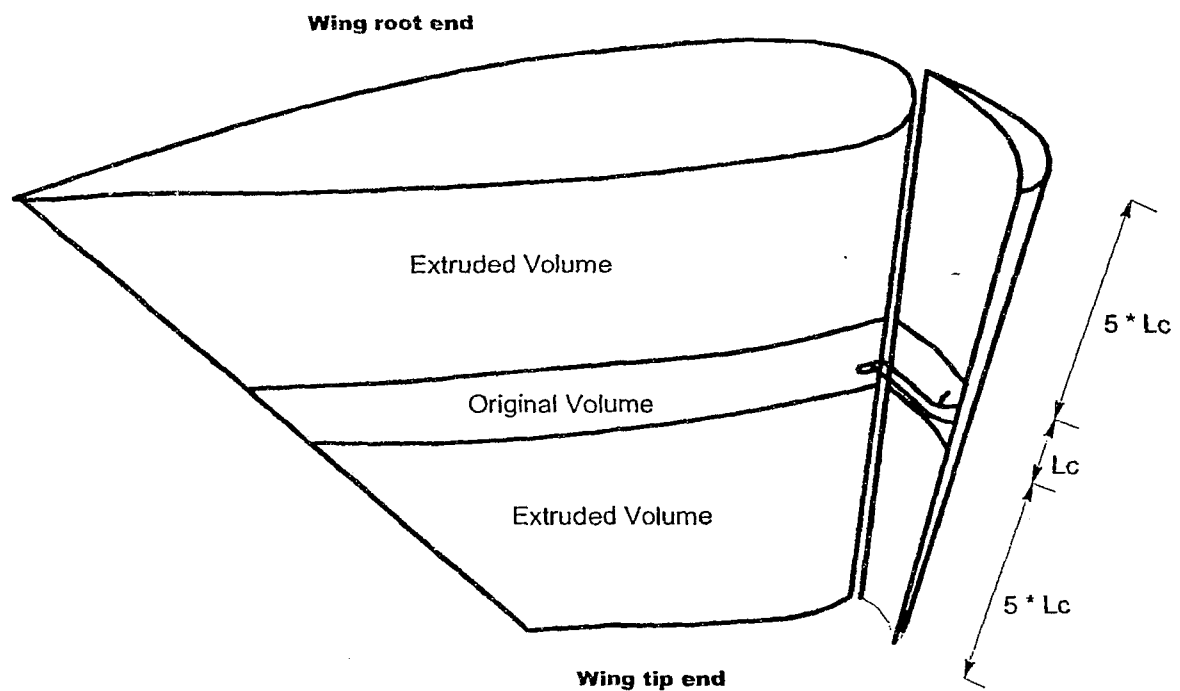
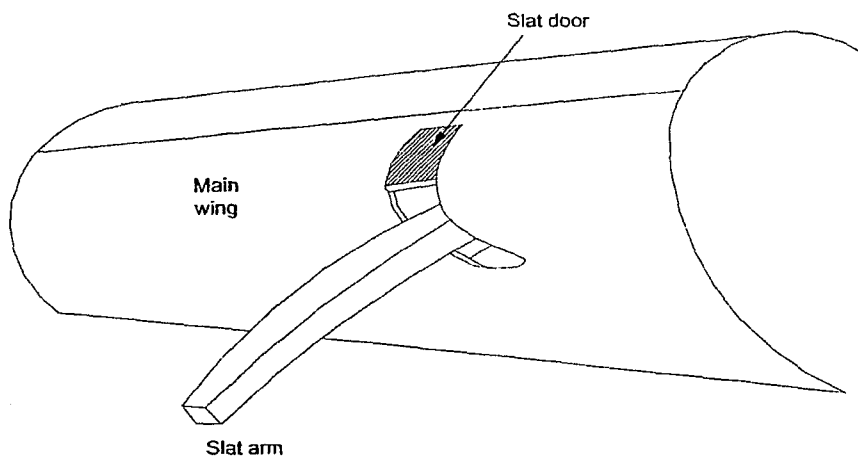


Figure 3.2.2: Extruded model of Aurora wing and slat configuration.

The extruded model has all the geometrical features affecting the wing aerodynamics performance. This section is tapered, twisted and has the same dihedral and swept back angles as the wing of Aurora aircraft with respect to the fuselage. Figure 3.2.3 shows a close up of the regenerated model. It does not have the nuts, bolts and cutouts on the Slat-Arm. Effect of these items in the aerodynamics performance of the wing will be negligible since they are in the shadow of the Slat and are too small relative to the size of the slat arm door.

Figure 3.2.3 shows the extended Slat arm and the door (Slat-Door) that partially covers the opening at the leading edge of the main wing. The Slat is attached to the Slat-Arm using the flange located at the end of the slat arm. The slat was intentionally erased from this figure to visualize the details around the Slat –Arm and Slat-Door region since it is in the shadow of the Slat.



**Figure 3.2.3: Simplified model of Aurora wing and slat configuration regenerated using GAMBIT showing slat arm door which covers the upper part of the opening. Note that slat is intentionally deleted to visualize the slat arm and the slat door.**

### **3.3 Modeling of the flow domain**

The flow domain of the mesh consists of the space surrounding the wing, which is discretized into a mesh of non-overlapping control volumes. Selection of the correct shape for the outer boundary of the numerical domain will reduce both the time and the memory consumption in creating the numerical model. The numerical model should also allow the user to change the direction of the flow simply by changing the unit vectors of the incident flow direction at the far field boundary rather than recreating the whole model.

The model should also be able to capture the important flow phenomenon such as flow separation, the wake behind the wing and the other flow properties like pressure, turbulence intensity and pressure distribution in the flow domain. These properties can extend to considerable



distances from the wall surfaces of the wing. Pressure Far Field Boundary (PFFB) conditions are commonly used to simulate the free stream velocity for external flow domain problems such as the one in this project. These boundary types should be placed at least 20-chords away from the wall surfaces of the wing to impose free stream conditions without interference on the wing [32]. Figure 3.3.1 shows how the wing is placed in the flow domain with respect to the far field boundary.

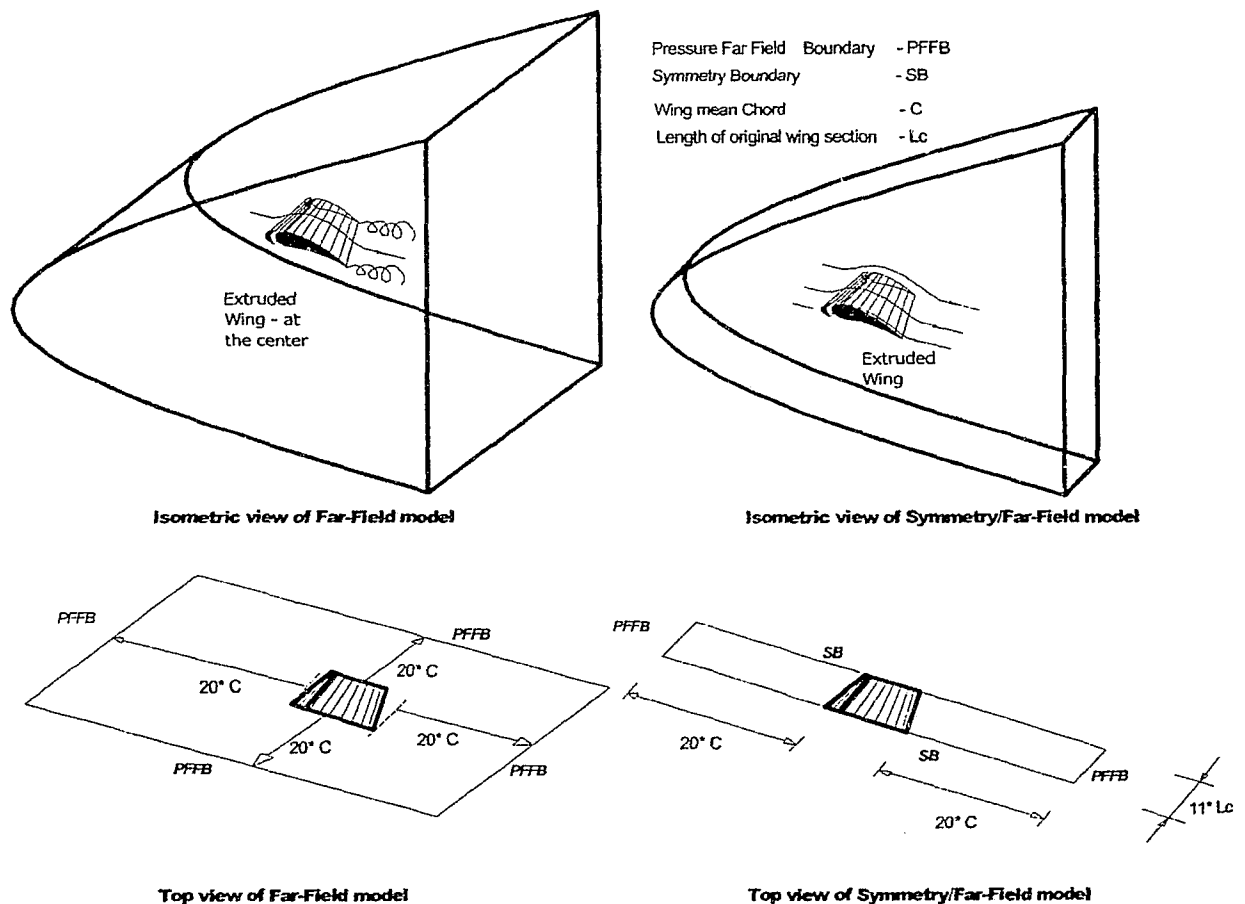


**Figure 3.3.1: Comparison of models between all sided Pressure Far-Field and Pressure Far-Field with symmetry boundary conditions.**

The size of the slat arm door compared to the wing main chord is comparatively small, thus one must introduce a very fine mesh around the slat arm door to visualize the flow around it.

Unfortunately it is impractical to cover the whole flow domain with this very fine mesh. A

---

uniformly fine mesh all the way to the far field domain located at 20 chord lengths will be cumbersome since the mesh will have billions of nodes as a result.

It is a challenge to generate a grid that can be accommodated by the available computational resources and yet model all of the desired flow features. Selection of an appropriate grid type needs some experience in grid generation. Questions owing to the selection of an appropriate mesh for the Aurora wing and slat configuration can be categorized as follows.

- Whether to reduce the size of computational domain and how much?
- Whether to select structured mesh, unstructured mesh or hybrid mesh which combines both structured and unstructured process?
- Whether the computational model will need a fine surface mesh everywhere?

Figure 3.3.1 shows that the size of the computational domain can be reduced by introducing symmetry conditions to the wing tip and root of the extended section of the wing rather than using Pressure far field boundary all around the wing. Symmetry conditions imply that all variables have zero gradients across the boundary. This figure shows both isometric and top views of the two models that one can adopt to generate the mesh of the Aurora wing and slat configuration. In a pressure far field boundary type model, the wing is placed at the center of the domain with 20 mean chord distances from all the sides of the wing to the far field boundary. Compared to the symmetry/far field model; only the two faces that are parallel to the wing have the pressure far field boundary type. The two faces through the wingtip and wing root of the symmetry/far field model use symmetry boundary conditions, reducing unnecessary depth to the flow domain and reducing the size of the computational domain.

The section of the wing given to the researcher is located at around middle of a half a span of the wing. Placing this section in the center of the Far-Field model will not simulate the same physical conditions since the far field model will introduce horseshow vortices, which will create a down wash. Since the symmetry boundary conditions case gives a smaller grid with no loss in applicability, it is this configuration that is used to model Aurora wing and slat configuration.

### 3.4 Creation and refinement of the mesh

Structured and unstructured are two methods of generating meshes of physical domains, each having it's own advantages and disadvantages. Figure 3.4.1 shows both structured and unstructured meshes with same off wall spacing ( $H$ ).

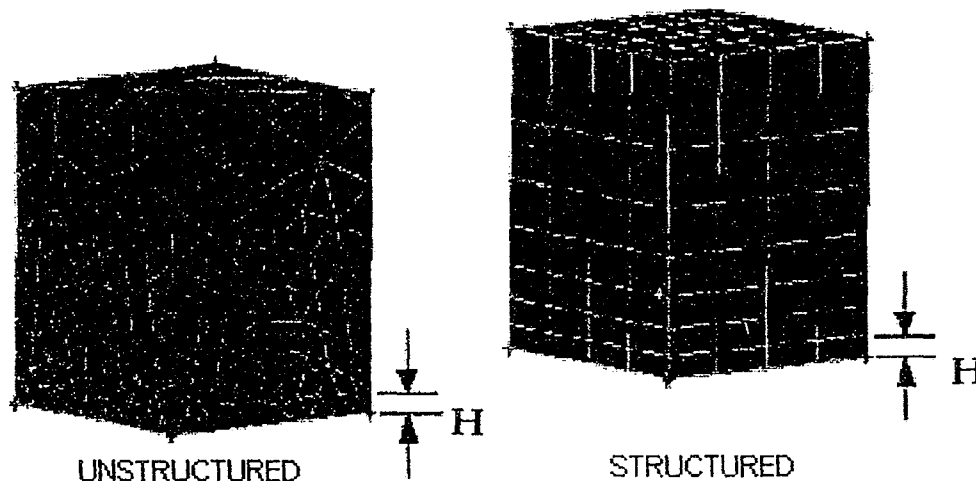


Figure 3.4.1: Comparison of unstructured and structured meshes. Both meshes have same off wall spacing.

Structured meshes are easier to handle computationally since their connectivity information of the individual nodes are stored block-to-block compared to the unstructured meshes. This block-to-block storage of connectivity information takes less memory to store and information can be easily access by the main solver program with less RAM. Structured meshes are difficult to create

with discontinuous volumes and complex geometries. Sometimes large volumes must be split into separate continuous smaller volumes in order to create a structured mesh. Splitting volumes and matching nodes of opposite faces of the individual rectilinear domains to create structured meshes can be a time consuming process.

In a structured mesh scheme, the number of mesh elements on the wall and the far field are the same since the structured mesh is generated simply by extruding the nodes on the continuous volume surfaces using a linear function connecting the wall surfaces and the far field boundary. Figure 3.4.2 shows how nodes 1, 2, 3, 4 and 5 are superimposed in to the far field boundary as nodes 1', 2', 3', 4' and 5'. It is therefore necessary to have a very fine mesh on the wall surfaces of the continuous volume in order to have a reasonable number of nodes in the Far field boundary.

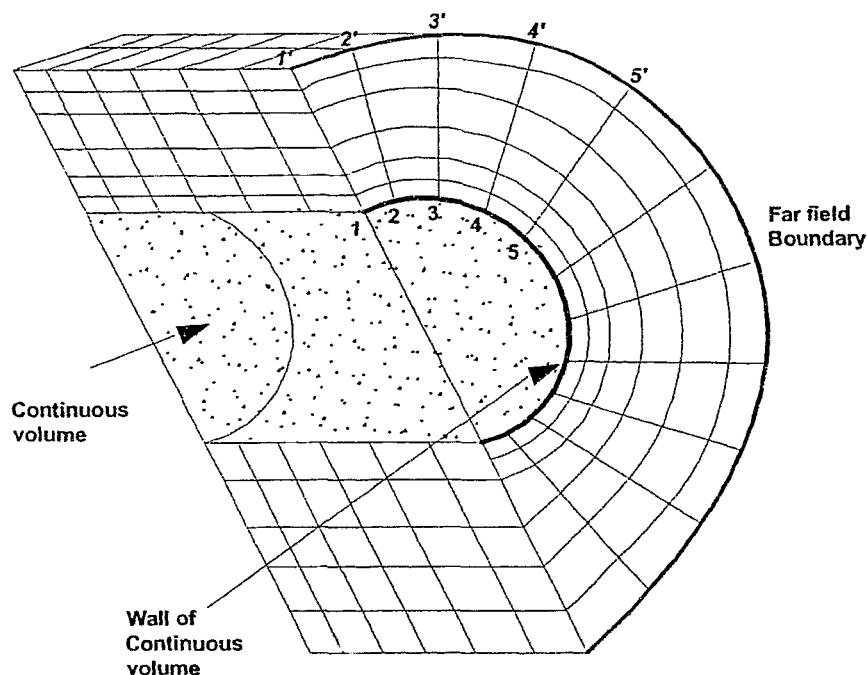
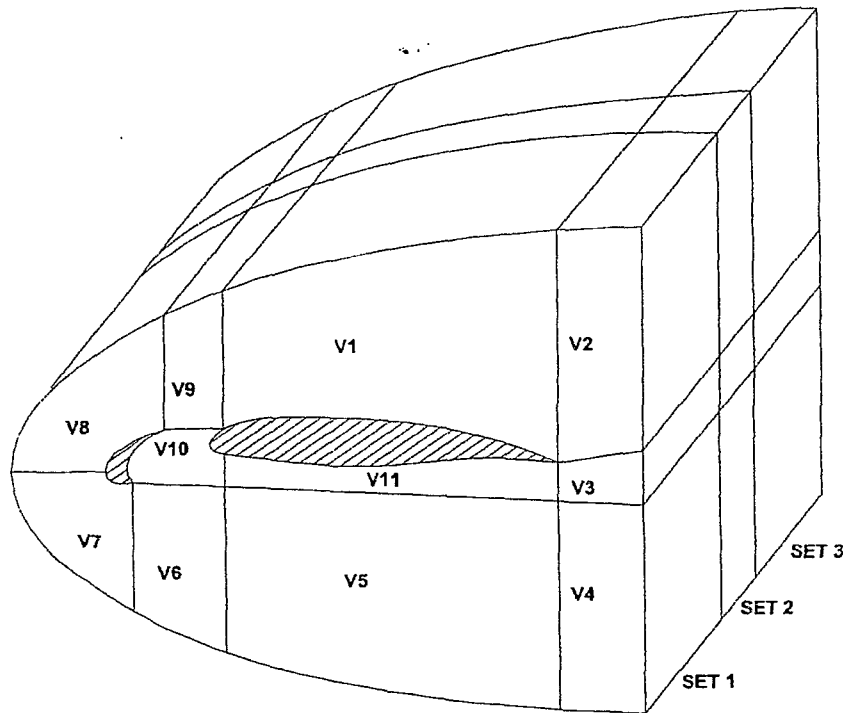


Figure 3.4.2: Use of structured mesh in continuous volumes.

The grid of the Aurora has a continuous volume except in region adjacent to the slat arm. The

flow domain of Aurora was split into 33 separate volumes. Figure 3.4.3 shows a cross section of the flow domain parallel to the symmetry boundary and how the volumes are split lengthwise of the wing.



**Figure 3.4.3: Flow domain of the Aurora model. Domain consists of 33 volumes. Volumes of set 1 are shown in the diagram and the rest are not shown due to clarity.**

All the volumes except the v10 of set 1, set 2 and set 3 were meshed using a structured mesh. The volume meshes of volumes v10 of set 1 and set 3 have prismatic elements and the volume meshes of volumes v10 of set 2 have tetrahedral meshes.

Two-dimensional study done with multi-element airfoil AGARD AR303 showed that flow separation is evident on the front top section of the slat and the upper surface of the main wing. These results obtained from the 2D multi-element-airfoil were used when meshing the edges and surfaces of Aurora model, placing a higher number of nodes in the areas of expected boundary layer separation.

The Spalart-Allmars turbulence model requires the first off wall node to have a  $y^+$  of order 1, implying that at least 10 nodes must be used to resolve a boundary layer profile [32].  $Y^+$  is a unit used to measure the distance from the wall surfaces to the first normal off-wall node. These units are called wall units and the value of  $Y^+$  can be found using equation 3.4.1. The approximate distance from the wing-upper surface and slat surface to first adjacent node in the interior flow domain was found to be in the order of  $10^{-3}$  inches for  $Y^+$  of 5. One cannot find exact  $Y^+$  before the model is partially solved. The required  $Y^+$  is a function of wall shear stress. The relation of  $Y^+$  to the wall shear stress can be written as follows,

$$Y^+ = \frac{\rho U_T}{\mu} y \quad (3.4.1)$$

Here  $\rho$  is the local density,  $y$  is the distance from wall to the first node in the flow domain normal to the wall,  $\mu$  is dynamic viscosity and  $U_T$  is frictional velocity that will defined as follows.

$$U_T = \sqrt{\left(\frac{\tau_w}{\rho}\right)} \quad (3.4.2)$$

Where  $\tau_w$  is the skin friction of the wall. The  $Y^+$  can be calculated using an iterative method. This can be itemized as follows.

1. Guess off wall placement and generate a grid
2. Obtain solutions (local  $\tau_w$ ) for the domain
3. Calculate the  $Y^+$  based on local  $\tau_w$ .
4. Regenerate the grid with local  $Y^+$  satisfies required value

There are two methods one can use to model the boundary layer using GAMBIT. One is using wall functions and the other method is to model boundary layer development directly, which is

used in this project. The latter method required fine node spacing normal to the wall. The wall function method is easy to establish with continuous volumes but one might face difficulties with edges that are not perpendicular to the wall surfaces. Figure 3.4.4 shows the boundary layers close to a wing trailing edge. Boundary layers of both upper and lower surfaces are generated using the boundary layer function available in GAMBIT. The boundary layer generated in upper surface of the wing could not continue along the interior boundary surface unless the surface enclosing wing upper surface and interior boundary surface were split to match the nodes across the boundary layer of the interface. The suitable location to split the surface is shown in dotted lines as long as the angles between this dotted edge and the wing upper surface wing trailing edge are less than  $90^\circ$ .

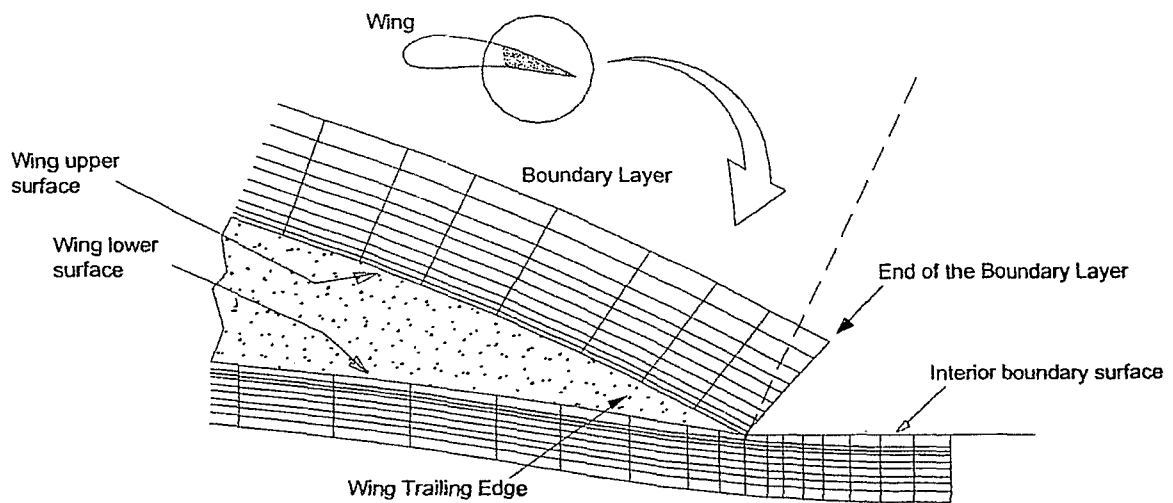


**Figure 3.4.4: Modeling boundary layers of two mating faces using GAMBIT. Picture shows the boundary layers along wing upper and lower surfaces towards the wing trailing edge.**

Figure 3.4.5 shows some surface meshes of the Aurora wing and slat configuration. The concentrated rectilinear mesh in the frontal section of the slat was introduced during the mesh

generation process to model the boundary layer, making sure the off wall spacing between the slat and the first node in the domain are within the required range to model viscous effect using the Spalart Allmaras model. After several trial and error mesh generation and solution iterations, the off-wall spacing was finalized such that the  $Y^+$  has a value of 4 on the frontal surface of the slat and upper wing surface.

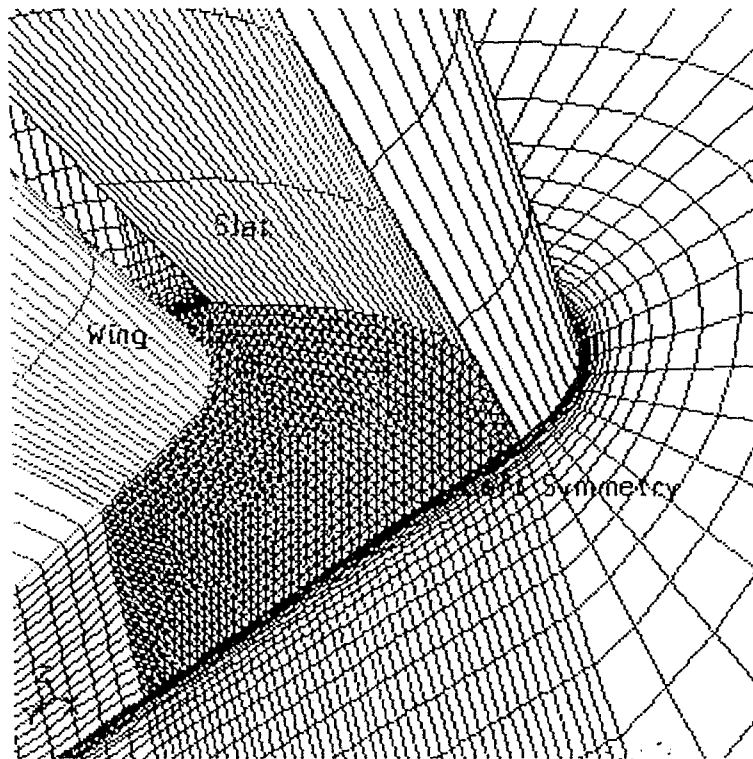


Figure 3.4.5: Surface mesh of the symmetry plane with respect to the wing and slat surfaces.

Figure 3.4.5 also shows the mesh of one of the symmetry planes of Aurora model with respect to the Wing and the Slat. The area on the left and right symmetry surfaces between the slat rear surface and the wing frontal surface are meshed using a triangular surface mesh while all the other



surfaces of the symmetry planes are meshed using the rectilinear mesh scheme. The surfaces of the slat and the wing close to left and right symmetry surfaces are also meshed using rectilinear mesh scheme.

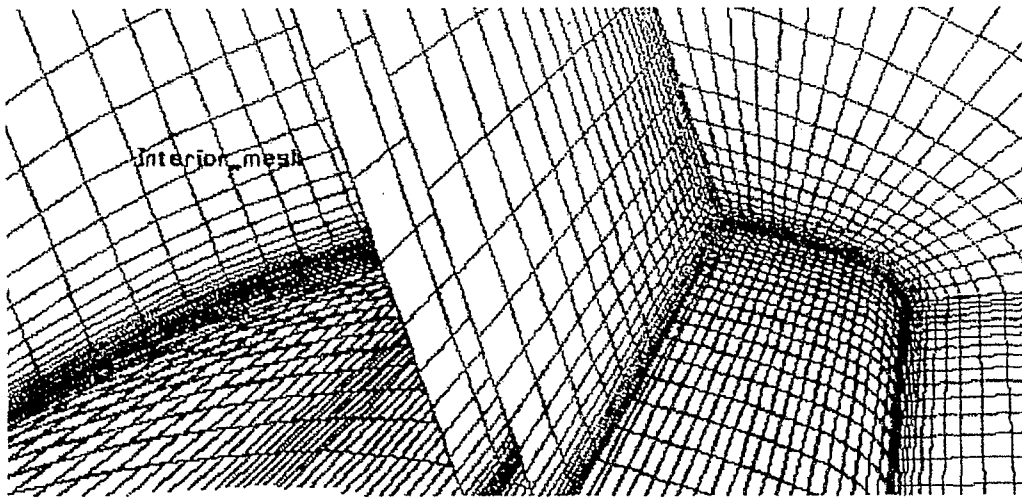


Figure 3.4.6: Surface mesh of a section of the extruded wing model and internal surface meshes of the flow domain.

Figure 3.4.6 shows the rectilinear surface mesh of the wing and the slat and the adjoining interior surfaces, which spans from the left symmetry surface to the right symmetry surface. The rectilinear surface mesh on the interior surfaces starts with  $y^+$  of 4 from the wing upper surface and the slat forward surface and increases nodal distance between nodes gradually towards the pressure far field boundary. The interior mesh starts from the lower surface of the wing with higher  $Y^+$  compared to the wing upper surface since the flow separation at higher angle of attacks occurs mostly on the wing upper surface and also to reduce the number of nodes of the overall mesh.

Figures 3.4.7 and 3.4.8 show the surface meshes around the Slat arm and how the surrounding surfaces are meshed using the triangular surface mesh scheme. The surface mesh of the slat arm consists of fine triangular meshes especially nearly the slat door. The slat arm has a very complex geometry, and it was found that triangular meshing scheme is the only option. The size of the triangular mesh along the slat arm from the vicinity of the Slat door area towards the Slat rear surface increases in size in order to match the triangular surface mesh of the Slat rear surface.

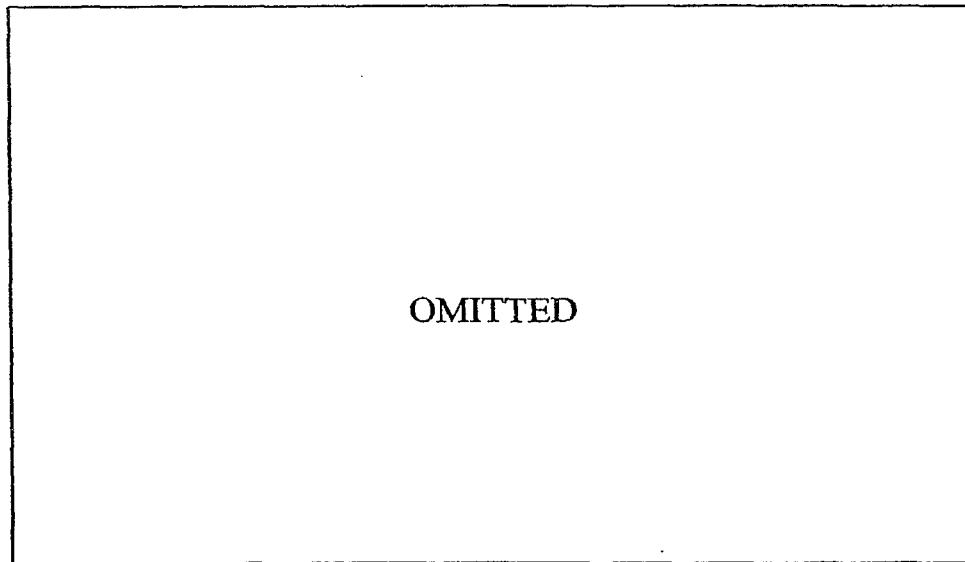
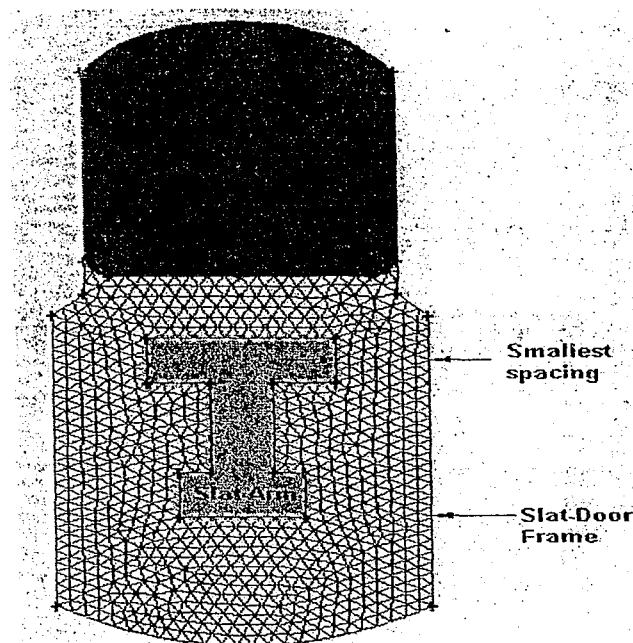


Figure 3.4.7: Surface meshes of the slat arm, slat rear and slat.

The spacing between slat arm and the slat doorframe is very small compared to the spacing between other surfaces in the model. Visualizing the model in 3D while meshing is very important in order to generate a smooth 3D mesh since the smoothing scheme may not be effective over the entire mesh.

The edge meshes around the Slat Door Frame, Slat Door and the Slat are carefully created especially near the opening of the main wing since the model must have at least 3 nodes across the

slat door frame and the slat arm as shown in figure 3.4.8, otherwise the flow would be restricted. The spacing between the Slat-Arm and the Slat-Door Frame of the actual model is much smaller than in this figure.



**Figure 3.4.8:** A Cross section sketch of the opening of the wing where slat arm is coming out.

The  $Y^+$  of the nodes in the vicinity of the Slat arm, volumes v10 of sets 1,2 and 3 is in the range of 30 to 60. FLUENT will use Log-Law to predict viscous effects in this region. This higher  $Y^+$  will reduce the unnecessary use of meshes in these unstructured mesh domains and also will avoid unnecessary stretching of elements that would sometime create negative volumes in mesh generation process. The slat box has a surface area of  $2030.758 \text{ cm}^2$ . The mesh of the slat box compartment consists of tetrahedral mesh elements and it has 8831 triangular wall face meshes.

Figure 3.4.9 shows the distribution of the triangular mesh on the Slat door and how the mesh is being stretched away from the slat arm. Mesh density of the Slat door towards the slat arm is higher compared to the wing upper surface side. Figure 3.4.10 shows the triangular surface mesh of the face connecting the wing lower surface and the wing box face. This face is named as the slat

doorframe in figure 3.5.10 and it shows that the size of the triangular surface mesh is almost the same size as the slat door to avoid the unnecessary stretching and the have more than 3 nodes across these surfaces as shown in figure 3.4.8.

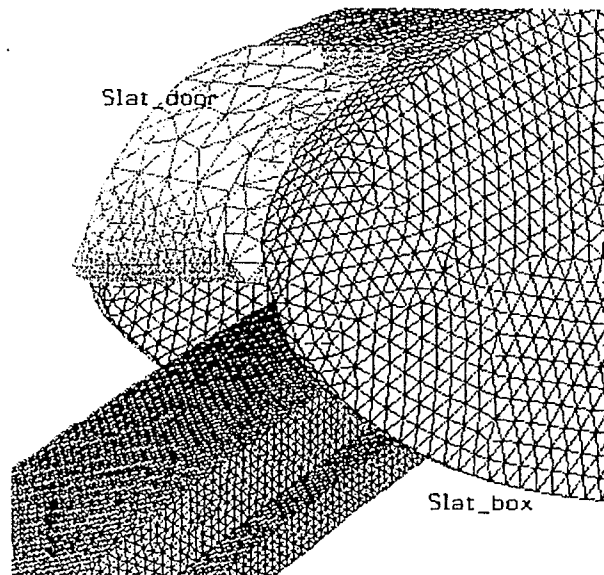


Figure 3.4.9: Surface mesh of the slat box with respect to slat door and the slat arm.

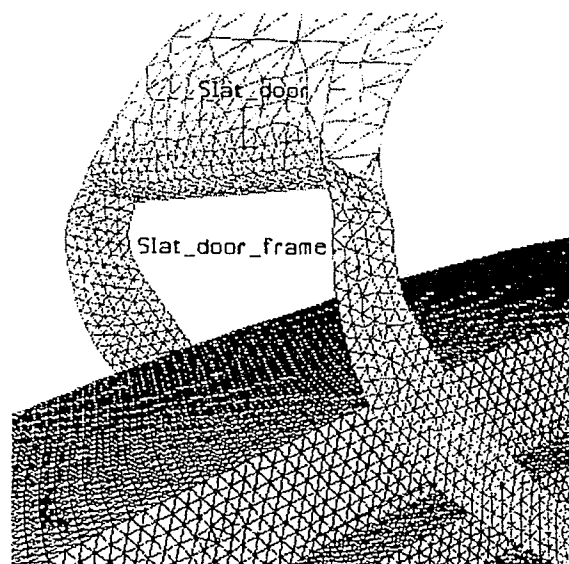
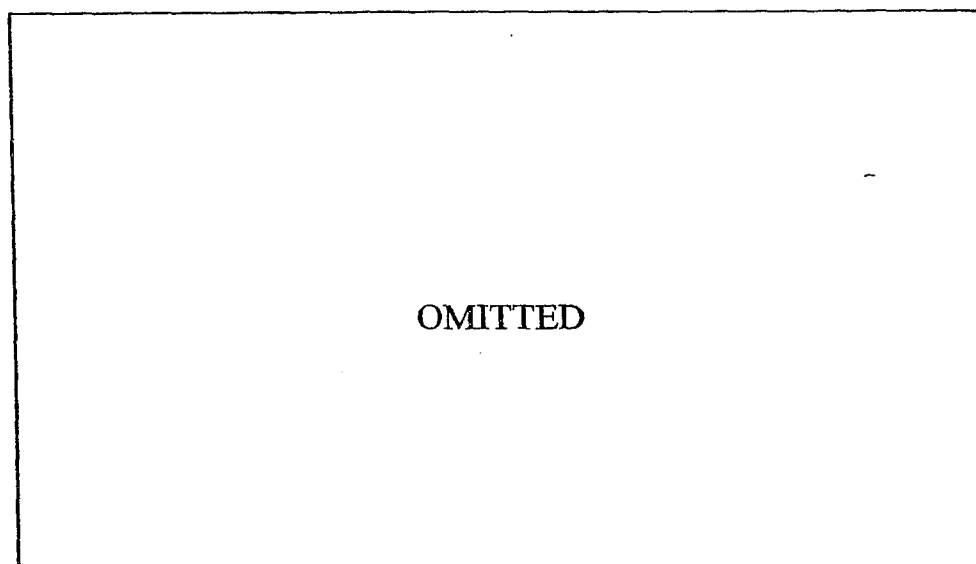


Figure 3.4.10: Surface mesh of the slat door with respect to slat doorframe.

Figure 3.4.11 shows a sketch of the Aurora model and appropriate names assigned by the user while table 3.4.1 shows the name of the entities, zones and the zone types.



**Figure 3.4.11: Boundary and continuum type specifications of Aurora wing and slat configuration.**

| Entity                           | Zone     | Zone Type          |
|----------------------------------|----------|--------------------|
| P_F_F                            | Boundary | Pressure Far Field |
| Slat Fwd                         | Boundary | Wall               |
| Slat Rear                        | Boundary | Wall               |
| Slat-Arm                         | Boundary | Wall               |
| Slat-Door (Only in closed model) | Boundary | Wall               |
| Slat-Door-Frame                  | Boundary | Wall               |
| Sym_Left                         | Boundary | Symmetry           |
| Sym_Right                        | Boundary | Symmetry           |
| Wing Lower                       | Boundary | Wall               |
| Wing Upper                       | Boundary | Wall               |
| All interior volumes             | Volumes  | Fluid              |

**Table 3.4.1: Zone type specifications of the Aurora wing and slat configuration. Entity Slat-Door exists only in the closed model.**

The table 3.4.2 shows the surface area and the number of surface nodes used in the door-opened model.

| Entity                | Type of cell                   | Zone size | Area (m <sup>2</sup> ) |
|-----------------------|--------------------------------|-----------|------------------------|
| Slat Fwd              | Quadrilateral wall faces       | 2352      | 3.06                   |
| Slat Rear             | Mixed wall faces               | 4996      | 2.38                   |
| Slat_arm              | Triangular wall faces          | 69439     | 6.21                   |
| Slat_box              | Triangular wall faces          | 8831      | 0.20                   |
| Slat-Door-Frame       | Triangular wall faces          | 3666      | 0.01                   |
| Wing_lower            | Mixed wall faces               | 10140     | 14.98                  |
| Wing_upper            | Quadrilateral wall faces       | 3528      | 13.96                  |
| Sym_Left              | Mixed symmetry faces           | 11656     | 7236.17                |
| Sym_Right             | Mixed symmetry faces           | 11552     | 7236.01                |
| P_F_F                 | Mixed pressure far-field faces | 27566     | 1574.26                |
| Total number of Nodes |                                | 1006104   |                        |

Table 3.4.2: Type of cell, size and the area of the respective zones

### 3.5 Assignment of zone types

Two types of conditions must be specified on each volume. They are Boundary type and Continuum type. Boundary type defines the properties of the internal and external boundaries and continuum type specifies whether the internal domain is either fluid or solid. Available boundary and continuum types may vary from solver to solver. The user is required to select the appropriate solver type before selecting the boundary type. FLUENT version 6 was selected as the solver for Aurora wing and Slat model. The grid generation software, GAMBIT usually selects internal and external boundaries as WALL boundaries and the interfaces between similar FLUID continuum zone types as INTERNAL boundary types. Previous studies discussed in the thesis showed that

the best model to use in the Aurora wing and slat model is the pressure far field model with symmetry boundary conditions. The user must carefully assigned appropriate values at the boundaries to represent the correct physical conditions. The values used in Aurora model for appropriate boundaries and assumptions made are given as follows:

### **1. Wall boundary conditions**

All the wall surfaces on Aurora wing and slat configuration are defined as adiabatic wall boundaries, which are kept at  $300^0$  K. Aluminum is selected as the material for wall boundaries with a default roughness constant of 0.5.

### **2. Internal boundary conditions**

All internal faces of the model, created when splitting volumes to ease the modeling process in GAMBIT, are usually defined as internal faces by default. These internal boundaries do not have a finite thickness and these faces are used as cell faces of the internal domain.

### **3. Symmetry boundary conditions**

The Symmetry boundary type introduces zero flux of all quantities across this boundary. The normal velocity component across the symmetry plane is zero. Since the shear stress is zero at a symmetry boundary, it can also be interpreted as a "slip" wall for viscous flow calculations. The planes going through the two end faces of the wing are used as symmetry boundary conditions to reduce the extent of the computational domain.

### **4 Pressure far field boundary conditions**

The Aurora aircraft goes through a range of angle of attacks during take-off and landing. Generating computational models for every angle of attack would be very time consuming. One can avoid remodeling the computational model by simply changing the direction of the free-stream velocity. This can be done by introducing Pressure far-field boundary conditions available to model a free-stream condition at infinity, with specified free-stream Mach number and static conditions. Pressure Far -field boundary use non-reflective boundary conditions, which allow

---

outgoing disturbances to pass through the boundaries without reflecting them back into the domain, thus creating a faster convergence.

Free stream velocity of 0.21Mach and static pressure of 101325 Pa are used as the boundary conditions in the far field. The user has to remember that this pressure far field boundary condition is valid only when the density of the external flow is calculated using the ideal gas law. The total temperature of 300 K and a recommended turbulent viscosity ratio of 10 [33] is used after introducing appropriate unit vector components into X, Y and Z directions based on the angle attack of the free stream.



## CHAPTER 4: MODEL SELECTION AND SOLVING STRATEGIES

### 4.1 Numerical techniques used in CFD

There are three main numerical solution techniques use in CFD. They are,

1. Finite volume method
2. Finite difference
3. Finite element method

The Finite volume method is very common among commercially available CFD software such as FLUENT, PHOENICS, FLOW3D and STAR-CD [34]. All these three numerical techniques use similar steps when finding solutions. Each method uses a unique discretization technique to approximate the Navier-Stokes equations such that relations of flow variables are represented by linear algebraic equations. According to Malalasekara W [34], the main differences between the three separate techniques are associated with the way the flow variables are approximated within the discretization process.

The computer power needed to reduce all the scales of the turbulent motion for a full 3D model of Aurora Wing and Slat is beyond all the capabilities at present. FLUENT 6 uses the Reynolds-Averaged approach (RANS) with an eddy viscosity turbulence model to transform the Full Navier-Stokes Equations (FNSE) into a solvable and simplified equations.

---

## 4.2 Selection of the turbulence model

The effects of turbulence are represented within in the RANS equations as a time averaged products of the velocity fluctuations  $u'v'$ . These averaged fluctuation products are called Reynolds stress  $\tau$ . The Bousinesque method approximates these stress using the mean velocity components  $\bar{u}$  and  $\bar{v}$  etc. The effect of turbulence is imposed on the mean flow by assuming that turbulence in the Reynolds stress appears as additional viscosity within the RANS equations.

The Spalart-Allmaras model, K- $\epsilon$  model, K- $\omega$  model, Reynolds Stress model (RSM) and Large Eddy Simulation (LES) model are few turbulence models that are used in FLUENT to model viscous effects [33]. Adding additional equations to model turbulence will substantially increases run time especially if the turbulence model uses more than one equation. So it is important for the user to find the appropriate viscous model to solve the problem with optimizing RAM and CPU time but still keeping a higher degree of accuracy of the solutions.

### 4.2.1 Comparison of viscous models

The Spalart-Allmaras model uses one conservation equation to define the behavior of a 'turbulence' variable. K-epsilon model use 2 equations and Reynolds Stress model uses 5 equations [33] Validations and selection of these turbulence models in FLUENT is extremely important since the results of all the viscous flow phenomenon depend on the viscous models.

A sensitivity study of these 4 turbulence models was done solving the 2D model of the NACA 0012 airfoil using FLUENT 5.4 solver. The 2D model was generated using a structured mesh with 5842 nodes using GMABIT and making sure the off wall spacing is within the required range to model the boundary layer for respective turbulence models. Viscous solutions for this model were

found for an angle of attack of  $6^\circ$ , free stream mach number of 0.21 with Reynolds number of 13.90 million after converging the residuals up to  $1e-3$ .

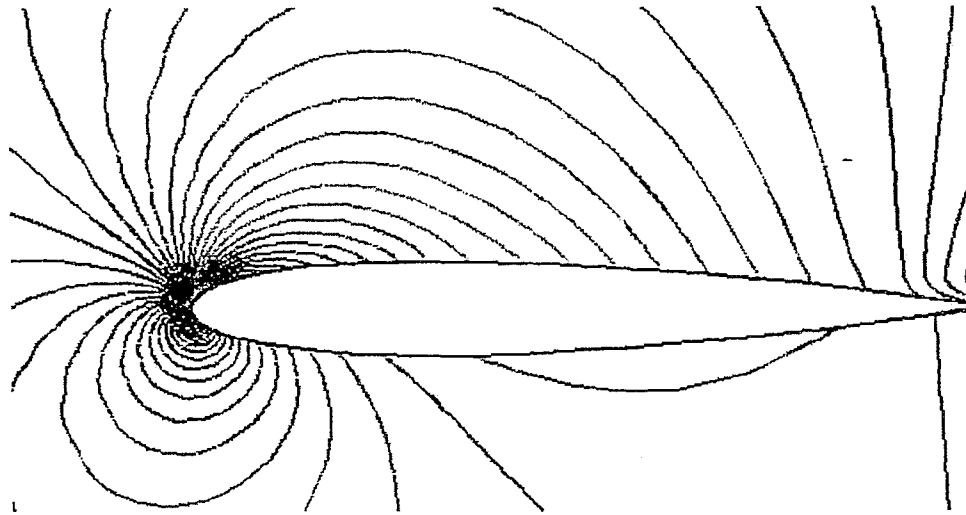


Figure 4.2.1: 2D Velocity distribution of the NSCA 0012 and slat configuration.  $M=0.21$  and Reynolds number of 13.9 million based on the mean chord.  $\alpha = 6^\circ$ .

Figure 4.2.1 shows the pressure distribution around the NACA 0012 airfoil found using FLUENT simulation. FLUENT was run on Sun Ultra 60 machine using UNIX operating system. The CPU speed of this machine is 450 MHz and the computer has 1 GB of RAM.

The Courant-Friedrichs-Lewy (CFL) number defines the local time step size in proportion to a grid and solution dependent stability limit. The default CFL value of 5 was used with a coupled solver with an implicit numerical solver. The Spalart-Allmaras model (SA), k-epsilon ( $k-\epsilon$ ) and Reynolds Stress (LES) model were run using a coupled, implicit and steady numerical scheme with 0.01 time step size and with 20 maximum iterations per time step to find which configuration consumes less time with minimum RAM to get coefficient results within 5% of the experimental results.

The results in table 4.2.1 show the values of  $C_D$ ,  $C_L$ , memory used for the size of case, data files in Kilo bytes (Kb), time to converge the solutions in seconds (sec) for the respective viscous models, and also the experimental values of  $C_D$  and  $C_L$ s.

| Turbulence Model         | $C_D$   | $C_L$   | Memory (KB) |           |       | Time (sec) |
|--------------------------|---------|---------|-------------|-----------|-------|------------|
|                          |         |         | Case file   | Data file | Total |            |
| SA                       | 0.06841 | 0.59430 | 275         | 267       | 542   | 112        |
| K- $\epsilon$            | 0.09066 | 0.54568 | 275         | 306       | 581   | 202        |
| RSM                      | 0.07402 | 0.56078 | 275         | 501       | 776   | 405        |
| Experimental Values [35] | 0.01001 | 0.68001 |             |           |       |            |

Table 4.2.1: Comparison of results for NACA 0012 airfoil at  $6^\circ$  angle of attack,  $M=0.21$  and Reynolds number of 13.9 million based on the mean chord.

The results in table 4.2.1 can be put into a scoring table as in table 4.2.2 as per their superiority and how close the results found using CFD simulations with respective turbulence model are to the experimental values. The best model gets 3 points and the worst gets 1 point and the intermediate gets 2 points.

| Turbulence Model \ Score | $C_D$<br>(Points) | $C_L$<br>(Points) | Memory<br>(Points) | Time<br>(Points) | Total<br>(Points) |
|--------------------------|-------------------|-------------------|--------------------|------------------|-------------------|
| SA                       | 1                 | 3                 | 3                  | 3                | 10                |
| K- $\epsilon$            | 2                 | 2                 | 2                  | 2                | 8                 |
| RSM                      | 3                 | 1                 | 1                  | 1                | 6                 |

Table 4.2.2: Turbulence model scoring: Note that, the equal total scores do not mean that a models perform identically in all tests.

SA model scored the highest total number of points compared to the K- $\epsilon$  and LES models proving that this model can be used to model Aurora wing and slat configuration and get better results with the resources available to the user.

### 4.3 Selection of solution algorithm and solution formation method

Fluent uses 2 types of solver formulations namely, segregated and coupled. The default solution algorithm in FLUENT is the segregated method. The segregated method allows the user

to control the solution process by solving the governing equations separately. The only disadvantage in this method is that the user cannot use an explicit method to formulate the equations. In a coupled solution algorithm, the user can select either the implicit or explicit method to formulate the equations. This method simultaneously solves all the governing equations and the user does not have the freedom to isolate the equations to accelerate the solution process.

One should have an idea of the computer power available to solve the problem before deciding which formulation method to select. Normally the implicit formulation method of equations requires more memory compared to the explicit formulation method. The Aurora wing and slat arm model has 1.1 million nodes. The implicit model of Aurora wing and Slat configuration needs almost 3 Gb of RAM compared to the explicit model, which uses only 1Gb of RAM to formulate the matrices required to solve the problem. It was impossible for the user to load the implicit case in the Sun Ultra 60 Dual processor machines which has only 1 Gb of RAM since the machine started using its reserved memory in the swap space with an IO ratio close to zero. The explicit model took only 10 minutes to load and consumed the entire RAM available in the machine and used only 0.5 GB of swap space.

#### **4.4 Selection of appropriate time step**

There is no straightforward method to select the correct time step for a given problem. There are some strategies one can follow to select the time step size. They can be itemized as below.

1. Maximum CFL number for the explicit method is 1 based on linear stability analysis, maybe up to 2.5 with residual smoothing.
2. According to linear stability theory, there is no limit in CFL number for implicit method but the practice cases run by the author using FLUENT showed that CFL number 10 gave best results.

- 
3. User must start the solution process with a small time step with CFL number of 0.1 for explicit and 1 for implicit and should slowly increase the time step as solution instabilities subside.

Studies done by the user with a Multi Element airfoil with implicit and explicit time integration method showed that the implicit formulation method is conditionally stable with respect to time step size. Selection of an optional time step size for a given problem is problem specific. The time step-size is determined by the global unsteadiness of the solutions as they evolve, requiring an optimum time step size in order to converge the solutions in a timely manner, which can be found using a trial and error basis.

#### 4.5 Solver control

The Aurora wing and slat configuration was solved using 3d version of FLUENT, coupling all flow equations with Spalart-Allmaras turbulence equation. An explicit time marching scheme with Courant number of 0.8 was used with relaxation factors for solid, turbulent viscosity and viscosity of 1, 0.8 and 1 respectively.

The variables of the model were solved using a linear solver. The flow variables had a termination criterion of 0.7 and used V-cycle while turbulence viscosity with flexible solver type having 0.1-termination criterion and 0.7 residual reduction tolerances.

The discretization scheme for both flow and turbulent viscosity were found using first order upwind scheme with no multigrid solver since multigrid solver took longer to perform relative results in comparison to results achieved without multigrid scheme.

## 4.6 Residual monitoring

User can select the required convergence criterion for the variable during solution process. The residuals in the Aurora model are continuity, x-velocity, y- velocity, z- velocity, energy and turbulent viscosity ( $\mu_t$  or nut in the convergence history) and their convergence criteria are as shown in table 4.6.1.

| Residual   | Convergence criterion |
|------------|-----------------------|
| Continuity | 1.00E-03              |
| X-velocity | 1.00E-03              |
| Y-velocity | 1.00E-03              |
| Z-velocity | 1.00E-03              |
| Energy     | 1.00E-03              |
| nut        | 1.00E-04              |

Table 4.6.1: Convergence criterion of the residuals

Figure 4.6.1 shows the behavior of the residuals of the variable from iterations 11500 to 16500.

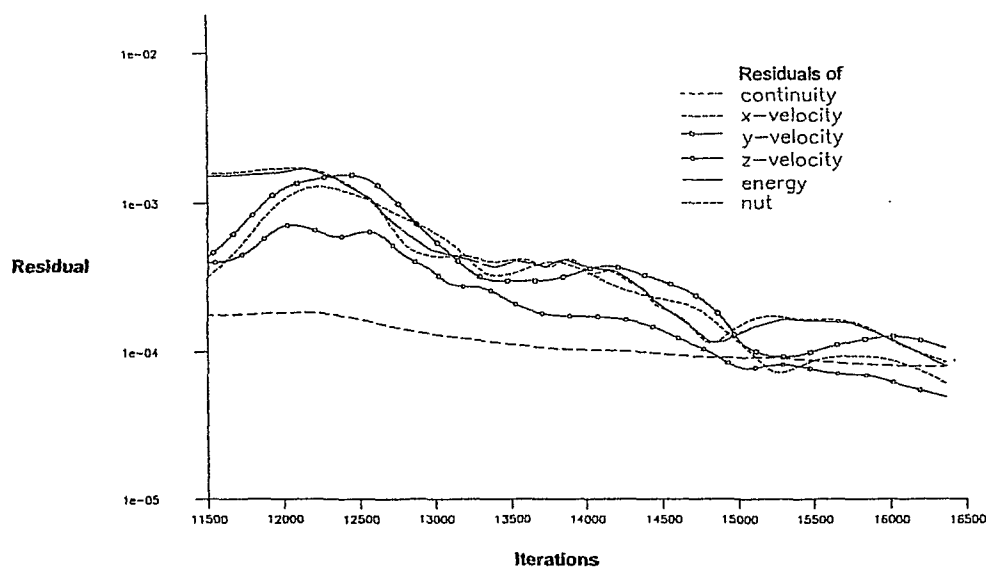


Figure 4.6.1: Convergence history of selected variables of Aurora wing and slat configuration.  $M=0.21$  and Reynolds number of 13.9 million based on the mean chord.  $\alpha=17.5^\circ$ .

---

The CFL number of 0.8 was used during the iteration process shown in figure 4.5.1. The solution process took 3 weeks to converge for the criterion given in the table 4.5.1, averaging 1.8 minutes per iteration.



## CHAPTER 5: THEORY

### 5.1 Basic equations in fluid dynamics

The finite volume method consists of three main steps. The first step is formal integration of the governing equation over every control volumes. Second step is discretization of the governing equations to convert the integral equation into a system of algebraic equations. The final step is to solve the algebraic equations by an iterative method [34].

The formal governing equations in fluid dynamics are the Full Navier-Stokes Equations (FNSE) in integral form, which is capable of expressing any flow scenario. The computer power required to find the direct flow solutions for FNSE with fully turbulent flow is highly phenomenal for a problem in the nature of Aurora wing and slat configuration. Instead, FLUENT uses averaged Navier-Stokes (RANS) equations which uses time averaged quantities. The integral form of the RANS equations is the basis for the discretization employed by FLUENT,

$$\frac{\partial}{\partial t} \int_{\Omega} Q dV + \int_{A_0} F \cdot dA_0 = \int_{\Omega} S dV \quad (5.1.1)$$

Here,  $Q$  is the vector of dependent variables,  $V$  is the volume of an arbitrary control volume  $O$ ,  $F$  is the flux vector containing both convective and diffusive fluxes,  $S$  is the source term vector, and  $A_0$  is the surface of the control volume. This model uses a second order upwind approach to

determine the fluxes on the control volume boundaries in the discrete form of the integral equation,

$$\frac{\partial}{\partial t} \bar{Q} V_{\Omega} + \sum_{sides, i} F \cdot dA_{\Omega i} = \bar{S}_{\Omega} V_{\Omega} \quad (5.1.2)$$

In this expression, the over bar indicates the average value of the term over the control volume, and  $dA_{\Omega i}$  is the area vector normal to the surface of the control volume of face  $i$  which forms the control volume surface

## 5.2 State equation

The three-dimensional Navier Stokes formulation provides 5 equations with the unknowns  $\rho$ ,  $u, v, w, E$  and  $P$ . The link between these variables can be written as follows.

$$p = (\gamma - 1) \rho \left[ E - \frac{1}{2} (u^2 + v^2 + w^2) \right] \quad (5.2.1)$$

Here  $\gamma = 1.4$ .

## 5.4 Spalart-Allmaras turbulence model

Closure of the Reynolds stress is provided by the one equation Spalart Allmaras (SA) turbulence model. [36]. Spalart and Allmaras suggested that the transport of an eddy viscosity variable could be represented as a modified form of the turbulent kinematics viscosity as shown in equation 5.4.1.

$$\rho \frac{D\bar{v}}{Dt} = G_v + \frac{1}{\sigma_v} \left[ \frac{\partial}{\partial x_j} \left\{ (\mu + \rho \bar{v}) \frac{\partial \bar{v}}{\partial x_j} \right\} + C_{b2} \rho \left( \frac{\partial \bar{v}}{\partial x_j} \right)^2 \right] - Y_v \quad (5.4.1)$$

Here  $G_v$  is the product of turbulent viscosity and  $Y_v$  is the destruction of turbulent viscosity that occurs in the near-wall region due to wall blocking and viscous damping. Also  $\sigma_v$  and  $C_{b2}$  are constants and  $v$  is the molecular kinematics viscosity.

The turbulent viscosity ( $\mu_t$ ) can be written as follows

$$\mu_t = \rho \bar{v} f_{v1} \quad (5.4.2)$$

Here  $f_{v1}$  is the viscosity damping function that can be written as

$$f_{v1} = \frac{x^3}{(x^3 + C_{v1})} \quad (5.4.3)$$

here

$$x = \frac{\bar{v}}{v} \quad (5.4.4)$$

The production term  $G_v$  of equation 5.4.1 is modeled as

$$G_v = C_{b1} \rho \tilde{S} \tilde{v} \quad (5.4.5)$$

where

$$\tilde{S} \equiv S + \frac{\tilde{v}}{k^2 d^2} f_{v2} \quad (5.4.6)$$

and

$$f_{v2} = 1 - \frac{X}{1 + X f_{v1}} \quad (5.4.7)$$

Here  $C_{b1}$  and  $k$  are constants,  $d$  is the distance from the wall, and  $S$  is a scalar measure of the deformation tensor. The value of  $S$  is based on the magnitude of the vorticity and the mean strain on the turbulence production.

$$S \equiv |\Omega_{IJ}| + C_{prod} \min(0, |S_{ij}| - |\Omega_{IJ}|) \quad (5.4.8)$$

Where

$$C_{prod} = 2.0, \quad \Omega_{ij} \equiv \sqrt{2\Omega_{ij}\Omega_{ij}}, \quad S_{ij} \equiv \sqrt{2S_{ij}S_{ij}} \quad (5.4.9)$$

Here  $S_{ij}$  is the mean strain rate is defined as,

$$S_{ij} = \frac{1}{2} \left( \frac{\partial u_j}{\partial x_i} - \frac{\partial u_i}{\partial x_j} \right) \quad (5.4.10)$$

The destruction term is modeled as follows

$$Y_v = C_{w1} \rho f_w \left( \frac{\tilde{v}}{d} \right)^2 \quad (5.4.11)$$

where

$$f_w = g \left( \frac{1 + C_{w3}^6}{g^6 + C_{w3}^6} \right)^{1/6}, \quad g = r + C_{w2} (r^6 - r), \quad r \equiv \frac{\tilde{v}}{\tilde{S} k^2 d^2} \quad (5.4.12)$$

Here  $C_{w1}$ ,  $C_{w2}$  and  $C_{w3}$  are constants and the defaults values can be written as follows.

$$C_{b1} = 0.1335, \quad C_{b2} = 0.622, \quad \sigma_{\tilde{v}} = 2/3, \quad C_{v1} = 7.1$$

$$C_{w1} = \frac{C_{b1}}{k^2} + \frac{(1 + C_{b2})}{\sigma_{\tilde{v}}}, \quad C_{w2} = 0.3, \quad C_{w3} = 2.0, \quad k = 0.41 \quad (5.4.13)$$

## 5.5 Wall boundary conditions

The SA model uses a laminar stress-strain relationship to find the wall shear stress when the mesh is fine enough to solve the laminar sub layer as shown.

$$\frac{u}{u_\tau} = \frac{\rho u_\tau y}{\mu} \quad (5.5.1)$$

Otherwise the law-of-the-wall is used to when the mesh is too coarse to resolve the laminar sub layer as given in equation 5.5.2.

$$\frac{u}{u_\tau} = \frac{1}{k} \ln E_1 \frac{u_\tau y}{\nu} \quad (5.5.2)$$

Here  $k=0.0419$  and  $E_1=9.793$ .

## 5.6 Discrete phase modeling

Injection of particles to the continuous phase is modeled using discrete phase modeling method. This method is usually solved coupling the continuous phase equations with the discrete phase equation. Normally the coupling of these equations is done once the continuous phase is converged. The discrete second phase is in a Lagrangian frame of reference [23] [37]. This second phase can consist of spherical inert particles, droplets or bubbles.

The trajectories of discrete particles are computed coupling both discrete and continuous phases. This was achieved keeping track of the heat, mass and momentum gained or lost by the particles and incorporating them in the continuous flow. The figure 5.6 depicts the exchange between the continuous phase and the particle in the discrete phase.

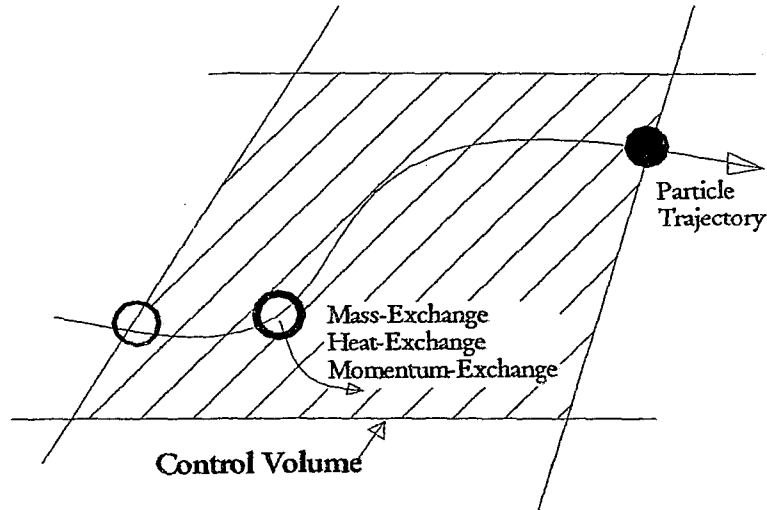


Figure 5.6.1: Heat, Mass, and Momentum transfer between the discrete and continuous phases [33].

The force balance of a particle in domain can be written as follows.

$$\frac{du_p}{dt} = F_D(u - u_p) + g_x(\rho_p - \rho) / \rho_p + F_x \quad (5.6.1)$$

Here  $F_D$  is the drag force per unit particle mass and it is given by

$$F_D = \frac{18\mu}{\rho_p D_p^2} \frac{C_D Re}{24} \quad (5.6.2)$$

Here  $u$  is the fluid phase velocity,  $u_p$  is the particle velocity,  $\mu$  is the molecular viscosity of the fluid,  $\rho$  is the fluid density,  $\rho_p$  is the density of the particle,  $D_p$  is the particle diameter and  $Re$  is the relative Reynolds number given by the following equation.

$$Re = \frac{\rho D_p |u_p - u|}{\mu} \quad (5.6.3)$$

The drag coefficient,  $C_D$  can be written as,

$$C_D = \frac{24}{\text{Re}}(1 + b_1 \text{Re}^{b_2}) + \frac{b_3 \text{Re}}{b_4 + \text{Re}} \quad (5.6.4)$$

where  $b_1, b_2, b_3$  and  $b_4$  as per Haider and Levenspiel [37]

$$\begin{aligned} b_1 &= 2.3288 - 6.4581\phi + 2.4486\phi^2 \\ b_2 &= 0.0964 + 0.5565\phi \\ b_3 &= 4.905 - 13.8944\phi + 18.4222\phi^2 - 10.2599\phi^3 \\ b_4 &= 1.4681 + 12.2584\phi - 20.7322\phi^2 + 15.8855\phi^3 \end{aligned} \quad (5.6.5)$$

Here  $\phi$  is the shape factor, which is given by

$$\phi = \frac{S_p}{S_p} \quad (5.6.6)$$

Where  $s$  is the surface area of the sphere having the same volume as the particle, and  $S$  is the actual surface area of the particle. For spherical particles  $\phi$  is equal to 1.

The force  $F_x$  is the force required to accelerate the fluid surrounding the particle which can be written as follows.

$$F_x = \frac{\rho d}{2\rho_p} \frac{d}{dt}(u - u_p) \quad (5.6.7)$$

## 5.7 Time integration

### 5.7.1 Implicit time integration

In the implicit time integration method, the value of some derivative function  $F$  with dependant variable  $\phi$  is evaluated at the future time level. This future value of  $\phi$  can be written as follows;

$$\frac{\phi^{n+1} - \phi^n}{\Delta t} = \frac{\partial F}{\partial t}. \quad (5.7.1)$$

Since the future value of  $\frac{\partial F}{\partial t}$  in a given cell is related through the future values of neighboring cells in the implicit integration technique; the implicit equation can be solved using an iterative technique after initializing  $\phi^i$  to  $\phi^n$  and iterating the following equation using first-order implicit formulation or second-order implicit formulation as follows.

First order:

$$\phi^i = \phi^n + \Delta t * F(\phi^i) \quad (5.7.2)$$

Second order:

$$\phi^i = 4/3\phi^n - 1/3\phi^{n-1} + 2/3\Delta t F(\phi^i). \quad (5.7.3)$$

In implicit formulation the value of  $\phi^i$  is iterated until the value stays constant. At this point one can say the solution is converged and the value of  $\phi^{n+1}$  is set to  $\phi^i$ . The advantage of the fully implicit scheme is that it is unconditionally stable with respect to time step size.

### 5.7.2 Explicit time integration



Explicit method in FLUENT™ can be used only when the equations are coupled. In this method the value of  $F(\phi)$  is evaluated at current time instead of future time in the implicit method. This can be written as,

$$\frac{\phi^{n+1} - \phi^n}{\Delta t} = F(\phi). \quad (5.7.4)$$

In explicit time integration method the value of  $F(\phi^{n+1})$  can be written explicitly using the existing solutions as follows.

$$\phi^{n+1} = \phi^n + \Delta t * F(\phi^n). \quad (5.7.5)$$

---

## CHAPTER 6: RESULTS

The Numerical models simulate the flow conditions about the Aurora wing and slat configuration, approximating the geometry and duplicating two-similarity parameters, in this case the Reynolds number and the Mach number [20]. The flow conditions and the assumptions made during modeling process of base model can be itemized as follows.

1. No cross flow attack angle.
2. No initial turbulence.
3. No humidity in air (dry air).
4. Standard temperature and pressure (STP).
5. Temperature: 300<sup>0</sup>K and Pressure: 101325 Pa.
6. No ground effects.
7. Adiabatic walls on aircraft.
8. Free stream Mach number during landing and take-off are the same.  $M_\infty=0.21$ .
9. No effect due to neighboring slat arms on the base model.

The region of the wing containing the slat arm and box is referred to as the base model in the following section.

## 6.1 Fuselage effect on the wing

The assumptions made to model the base model are valid only when there are no significant effects due to the fuselage on wing performance. Modeling the fuselage with the same dimensions as the Aurora aircraft with a similar wing will give a valid comparison of the base model and the base model with the fuselage. A full 3D model of an aircraft without high lift devices and empennage was modeled using FLUENT to find the effect of the fuselage on the section of the base model. The full 3D model has the general dimension such as length, width and height of the Aurora aircraft [1]. A one half of the aircraft was built introducing a symmetry boundary conditions across the plane running through the fuselage dividing the whole aircraft into two equal parts as shown in figure 6.1.1.

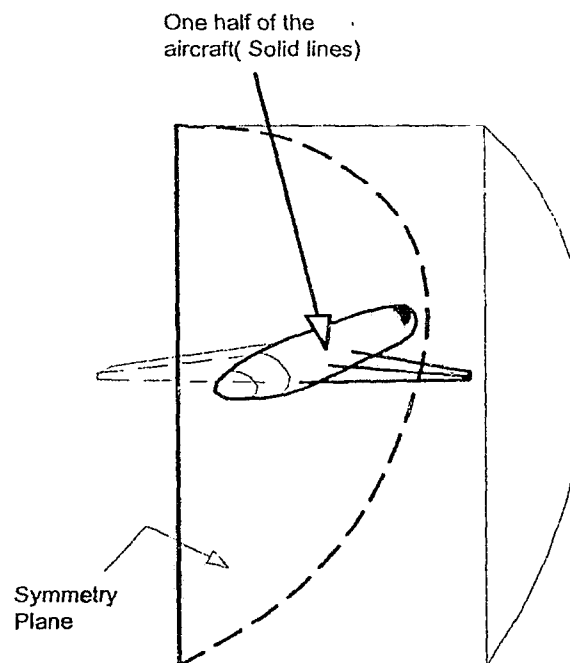


**Figure 6.1.1: Schematic of the 3D model built to simulate the full 3D aircraft. Not to scale.**

The 3D model was built using tetrahedral meshing scheme with tight off wall spacing around the fuselage to model the effects on the wing. The flow had a free-stream Mach number of 0.21, STP and incident angle of attack  $15^\circ$ .

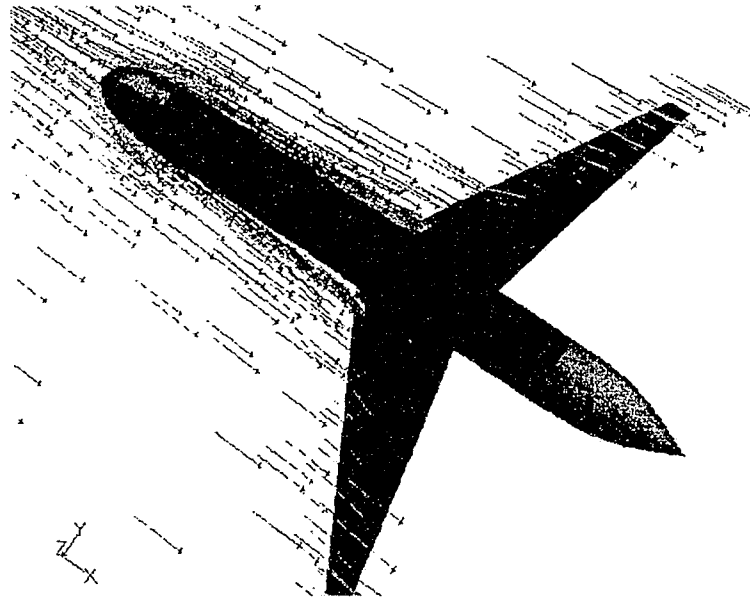


Figure 6.1.2: Velocity vectors of a plane parallel to the wing and through the fuselage and wing.  $M=0.21$  and Reynolds number of 13.9 million based on the mean chord.  $\alpha = 15^\circ$ .

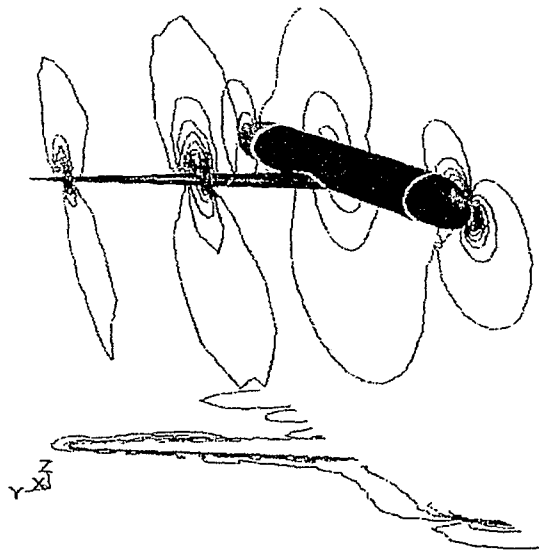


Figure 6.1.3: Static Pressure contour plots of planes through symmetry, two planes across the wing parallel to symmetry plane and a plane parallel to the wing running through the fuselage (shifted down for clarity).  $M=0.21$  and Reynolds number of 13.9 million based on the mean chord.  $\alpha = 15^\circ$ .

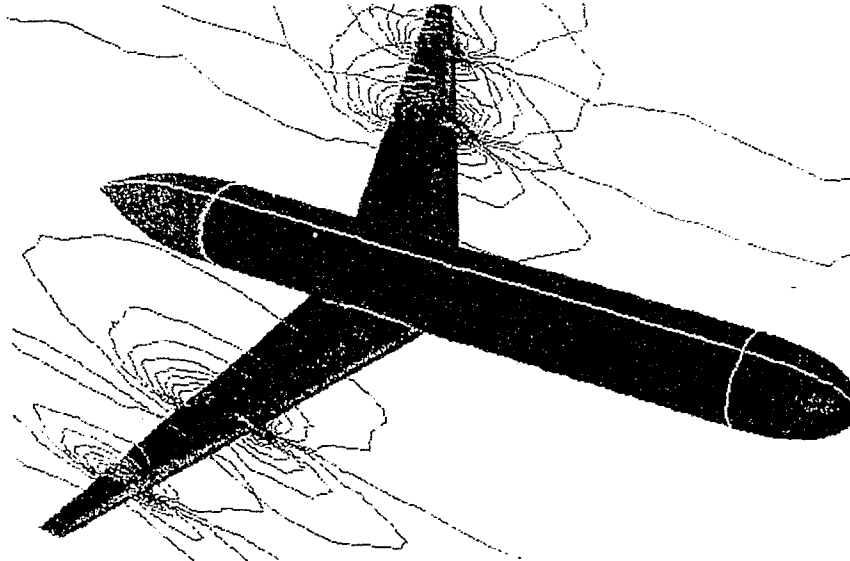


Figure 6.1.4: Static Pressure contour plots of two planes across the wing parallel to symmetry plane and filled pressure contours of the wing of the models with fuselage.  $M=0.21$  and Reynolds number of 13.9 million based on the mean chord.  $\alpha = 15^\circ$ .

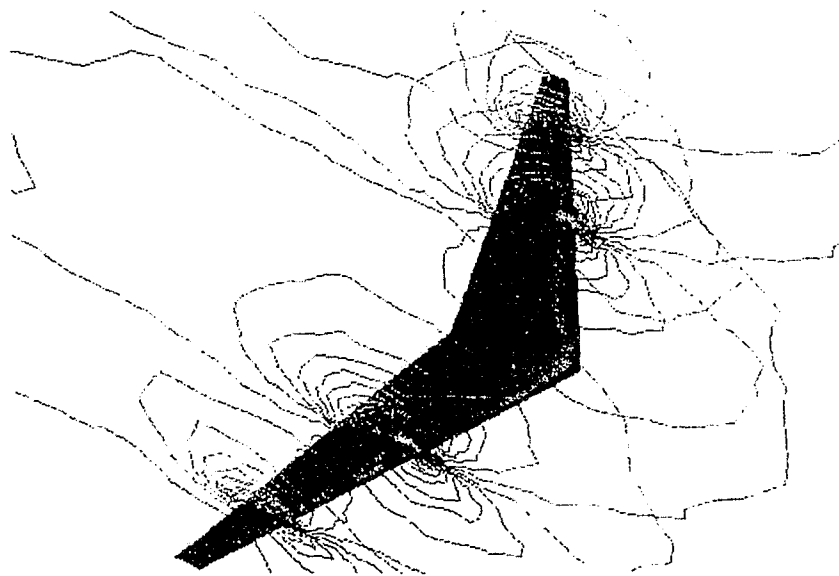


Figure 6.1.5: Static Pressure contour plots of two planes across the wing parallel to symmetry plane and filled pressure contours of the wing of the models without fuselage.  $M=0.21$  and Reynolds number of 13.9 million based on the mean chord.  $\alpha = 15^\circ$ .

Figure 6.1.2 shows the vector plots through a plane parallel to the wing. The vectors are colored based on the direction perpendicular to the fuselage (Y direction as in figure 6.1.2). Only the vectors around the cockpit area and the connection of the wing to the fuselage show a

---

significant change in the direction. All the other vectors especially in the region where the base model is located, 71.96-313.96 inches from the fuselage show no change in the direction. These results confirm that there is no effect on the direction of the flow of the free stream in the base model due to presence of the fuselage.

Figure 6.1.3 shows the pressure contours of selected planes and a sketch of Aurora wing and the location of the base model with respect to the fuselage. These two planes are parallel to the symmetry plane and are located at 71.96 and 313.96 inches away from the wing root. The pressure contours of a plane running perpendicular to the symmetry and through the center of the fuselage are shown below the aircraft. This plane is shifted below the fuselage for visualization purposes and clarity. Pressure contours of this plane perpendicular to the symmetry shows that contours emanate from the fuselage do not span into the location of the base model. This confirms that there are no significant effects on the static pressure due to the fuselage on the base model. Figures 6.1.4 and 6.1.5 also show the pressure field, with and without fuselage respectively. These pressure fields consist of filled contours of pressure on the wing and pressure contours of the planes parallel to the symmetry planes located at the ends of the base model. These pressure fields show no significant differences except the filled contours close to the fuselage on the wing of the model with the fuselage.

The velocity vector plots and the pressure contours in the 3D aircraft models confirmed that assumed free stream boundary conditions adopted in the base model are reasonable and valid and there are no effects due to fuselage on the base model. This proof is valid only for the base model located at 76.96 inches away from the wing root.

## 6.2 Comparison of total configuration lift and drag

Table 6.2.1 shows the values of the coefficients of lift ( $C_L$ ) and the drag ( $C_D$ ) of the door closed and the door opened modes of Aurora wing and slat configuration, computed at an angle of attacks ( $\alpha$ ) of 0, 5, 10, 15, 17.5, 20 and 22.5 degrees. These values were found at free stream Mach number of 0.21 and the Reynolds number of 13.9 million based on the average chord of the base model. The surface area of the slat door is used as the reference area to find the coefficients of lift and drag. The equations used to find the values of  $C_L$  and  $C_D$  are given in 6.2.1 and 6.2.2. as follows,

$$C_L = \frac{Lift}{\frac{1}{2} \rho_{\infty} V_{\infty}^2 S_{Slat-Door}} \quad (6.2.1)$$

$$C_D = \frac{Drag}{\frac{1}{2} \rho_{\infty} V_{\infty}^2 S_{Slat-Door}} \quad (6.2.2)$$

Here  $S_{Slat-Door}$  is the surface area of the slat arm door since it is not arbitrary.  $V_{\infty}$  is the velocity of free of free stream and  $\rho_{\infty}$  is the density of free stream. Quantitative values of these quantities can be found in the table C1 of the appendix C.

| Angle of<br>Attack (deg.) | Closed       |              | Opened       |              | (Closed-Opened) |              |
|---------------------------|--------------|--------------|--------------|--------------|-----------------|--------------|
|                           | $C_L$ Closed | $C_D$ Closed | $C_L$ Opened | $C_D$ Opened | Del( $C_L$ )    | Del( $C_D$ ) |
| 0.0                       | 447.7117     | 110.5620     | 440.4546     | 110.1266     | 7.2571          | 0.4354       |
| 5.0                       | 1137.8368    | 127.0305     | 1127.8842    | 127.2715     | 9.9526          | -0.7542      |
| 10.0                      | 1827.9618    | 190.5872     | 1815.3137    | 192.5311     | 12.6481         | -1.9439      |
| 15.0                      | 2363.8215    | 309.9303     | 2348.7630    | 312.9369     | 15.0585         | -3.0065      |
| 17.5                      | 2607.9714    | 386.0548     | 2574.5394    | 389.4086     | 33.4319         | -3.3538      |
| 20.0                      | 2088.5413    | 473.1971     | 2074.4780    | 470.5924     | 14.0632         | 2.6048       |
| 22.5                      | 2198.9996    | 576.8675     | 2189.4073    | 574.3820     | 9.5923          | 2.4856       |
| 25.0                      | 2315.3803    | 692.0378     | 2257.4867    | 680.8645     | 57.8936         | 11.1734      |

**Table 6.2.1: Coefficient of lift ( $C_L$ ), coefficient of drag ( $C_D$ ) and difference in coefficients of  $C_L$  and  $C_D$  of closed and opened models found using FLUNET at a range of angle of attack.  $M=0.21$  and Reynolds number of 13.9 million based on the mean chord.**

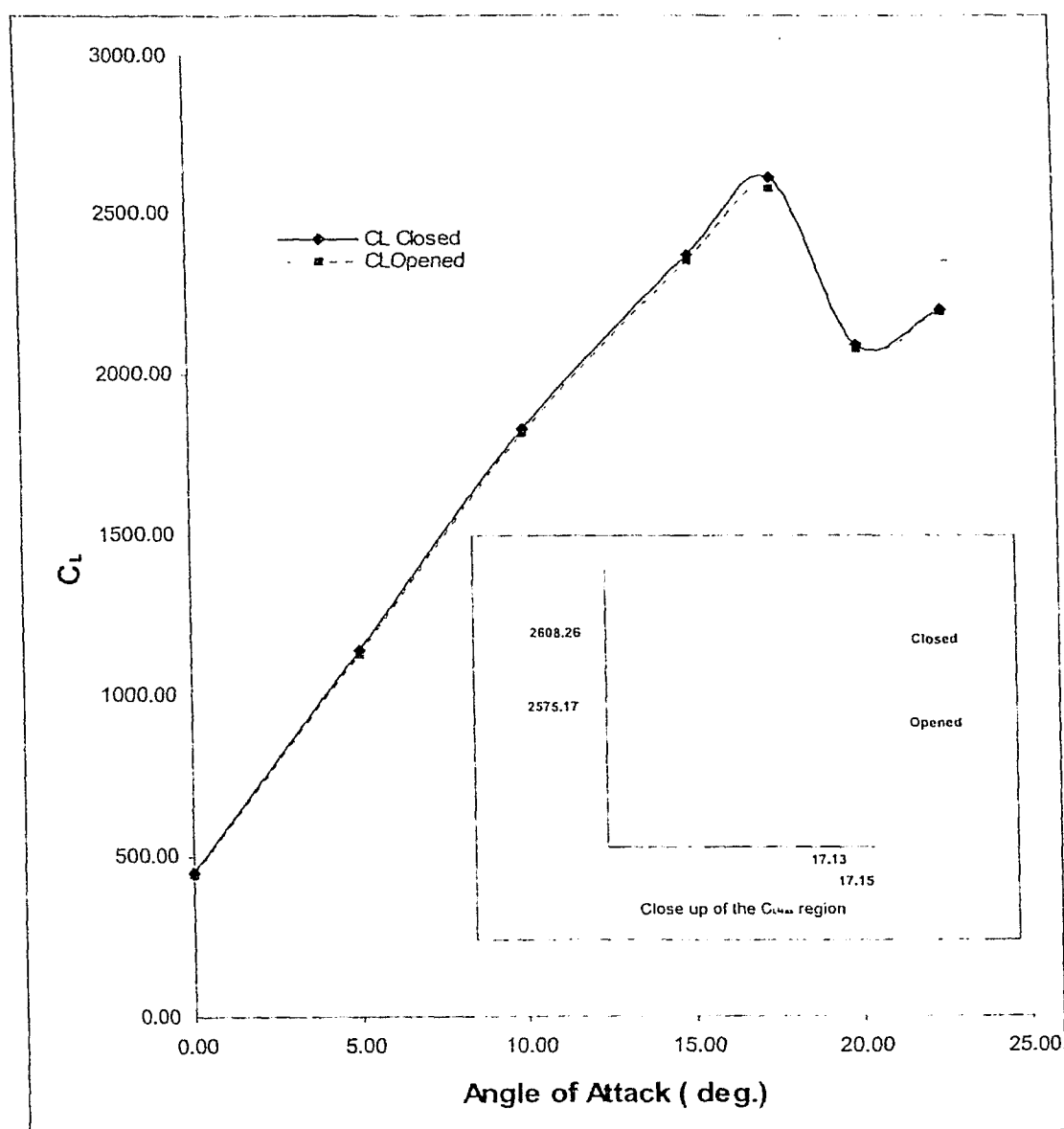


Figure 6.2.1:  $C_L$  vs.  $\alpha$  for closed and opened configurations of base models.  $M=0.21$  and Reynolds number of 13.9 million based on the mean chord.

Figure 6.2.2 shows variation of  $C_L$  of both door closed and door opened models as angle of attack increases from 0 to 22.5 degrees.  $C_L$  for both closed and opened models increase as angle of attack increases up to  $17.5^\circ$  angle of attack. The close up of  $C_{L_{Max}}$  region shows that stall is



reached at  $17.125^\circ$  angle of attack with the door opened model compared to  $17.150^\circ$  for door closed model. The respective  $C_{L_{Max}}$  for corresponding stall angles are 2608.256 for the door closed model and 2575.165 for door opened model.

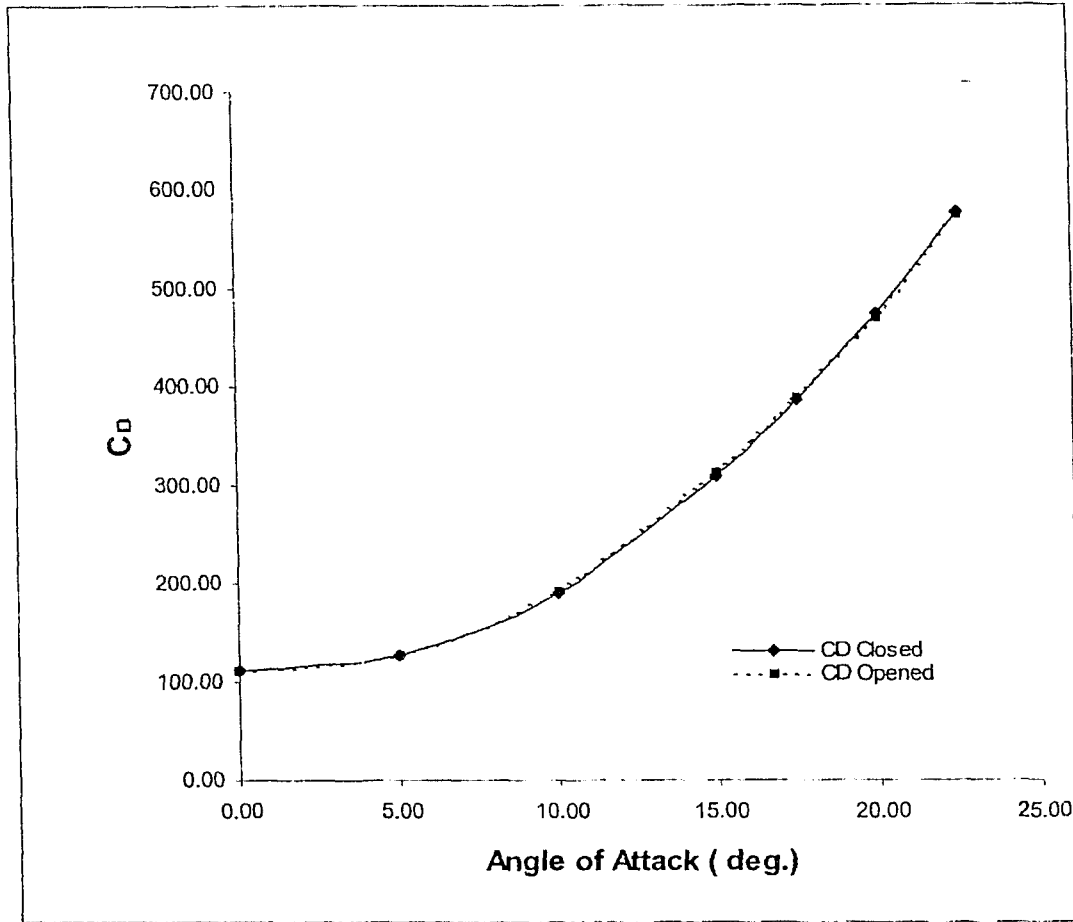


Figure 6.2.2:  $C_L$  vs.  $\alpha$  for closed and opened configurations of base models.  $M=0.21$  and Reynolds number of 13.9 million based on the mean chord.

Figure 6.2.2 shows variation of  $C_D$  of both closed and opened models as angle of attack increases from 0 to 22.5 degrees. This graph does not show a significant difference between two models instead the differences in coefficients of the lift and the drag between the two models is shown in figure 6.2.3. The differences in coefficients of the lift and the drag were found

subtracting the respective coefficients of closed model by the opened model as given in equations 6.2.3 and 6.2.4. They are symbolized by  $\Delta(C_L)$  and  $\Delta(C_D)$  respectively.

$$\Delta(C_L) = C_{L-Closed} - C_{L-Open} \quad 6.2.3$$

$$\Delta(C_D) = C_{D-Closed} - C_{D-Open} \quad 6.2.4$$

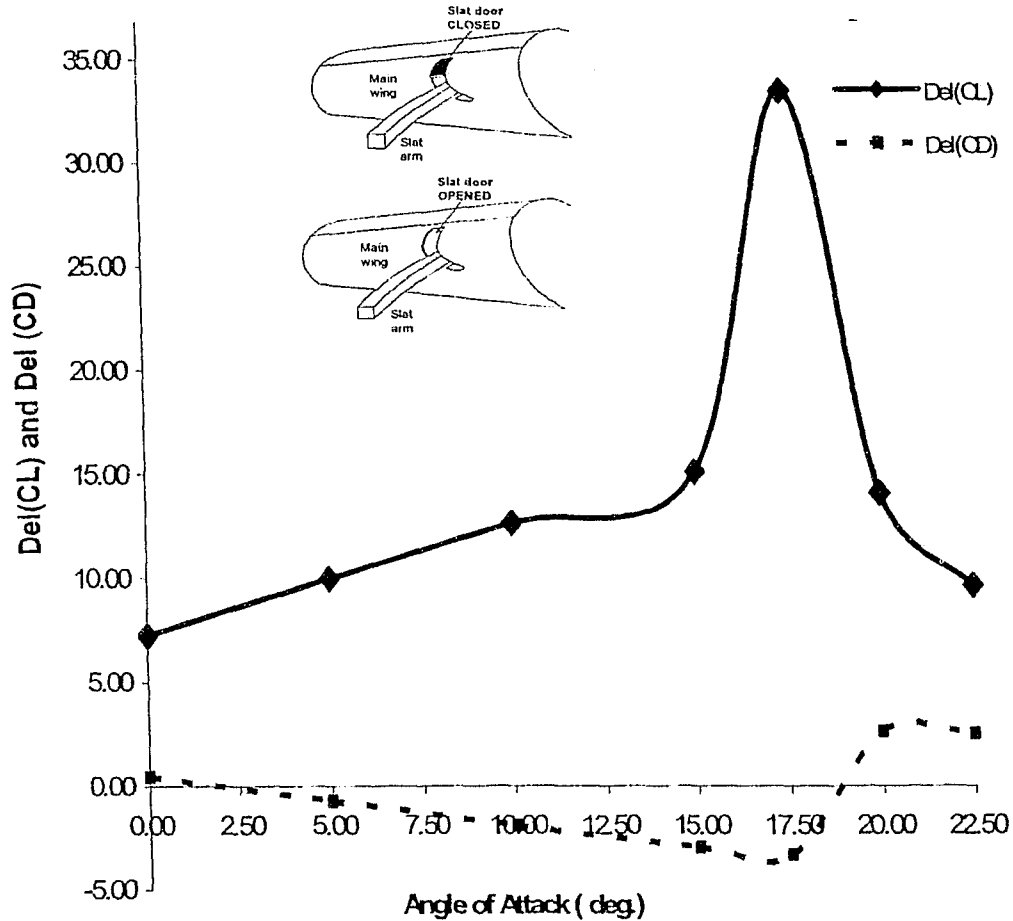


Figure 6.2.3: Difference in lift and drag coefficients between the slat door opened and closed cases. (closed – opened).  $M=0.21$  and Reynolds number of 13.9 million based on the mean chord.

The solid lines in figure 6.2.3 represents  $\Delta(C_L)$  and hidden lines represents  $\Delta(C_D)$ . Results shows that  $\Delta(C_L)$  increases at lower angles of attacks while  $\Delta(C_D)$  decreases. The  $\Delta(C_L)$  for  $17.5^\circ$  is almost double the value at  $15^\circ$ . At higher angles of attacks (beyond  $17^\circ.5$ )  $\Delta(C_L)$  started

decreasing and  $\Delta C_D$  started increasing up  $20^\circ$ .

### 6.3 Surface pressures

The figures 6.3.2 to 6.3.8 show the comparison of negative surface pressure coefficients of Aurora slat and wing of the closed and opened models at a free stream Mach number of 0.21, angle of attack of  $17.5^\circ$  and Reynolds number of 13.90 . The results were calculated at 0%, 25%, 32.5%, 50%, 62.5%, 75% and 100 % locations along the wing as shown in figure 6.3.1.

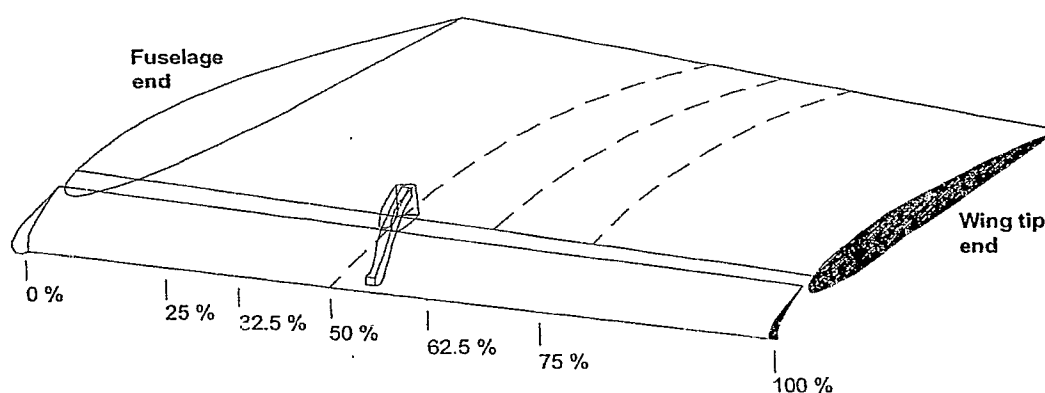


Figure 6.3.1: Locations of the planes where  $C_p$  distributions are depicted in figures 6.3.2 to 6.3.8

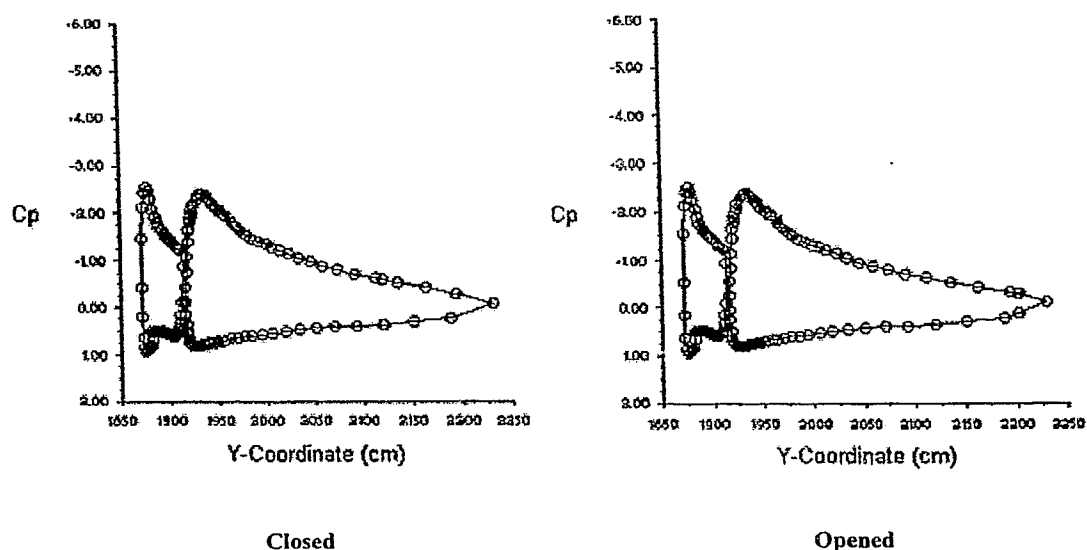
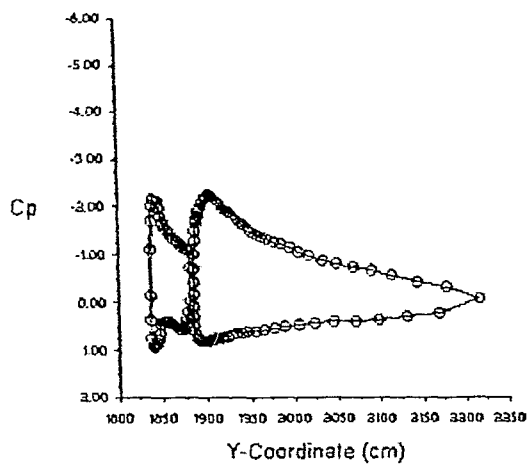
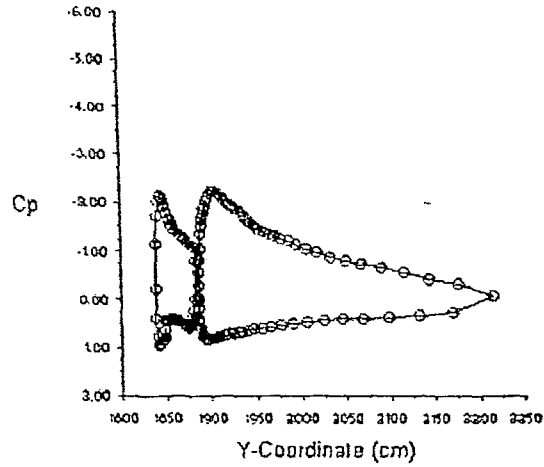


Figure 6.3.2: Comparison of  $C_p$  on slat and wing at 0% location between closed (left) and opened (right) models calculated at Mach number of 0.21, angle of attack of  $17.5^\circ$  and Reynolds number of 13.90 million.

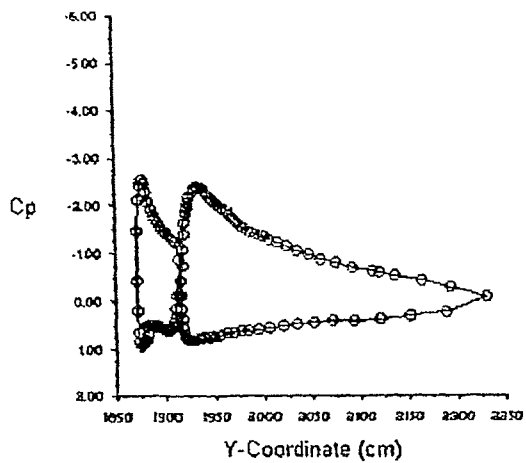


Closed

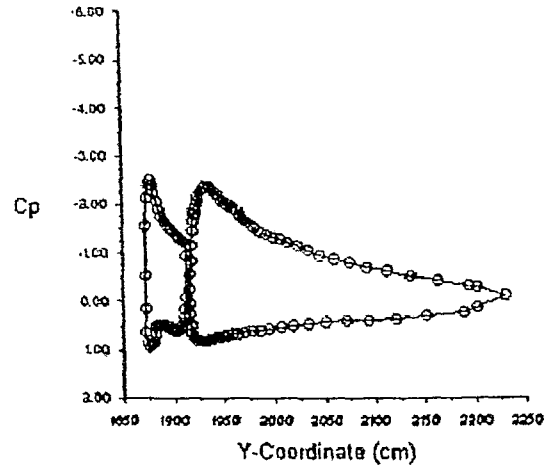


Opened

Figure 6.3.3: Comparison of  $C_p$  on slat and wing at 25% location between closed (left) and opened (right) models calculated at Mach number of 0.21, angle of attack of  $17.5^\circ$  and Reynolds number of 13.90 million.



Closed



Opened

Figure 6.3.4: Comparison of  $C_p$  on slat and wing at 32.5% location between closed (left) and opened (right) models calculated at Mach number of 0.21, angle of attack of  $17.5^\circ$  and Reynolds number of 13.90 million.

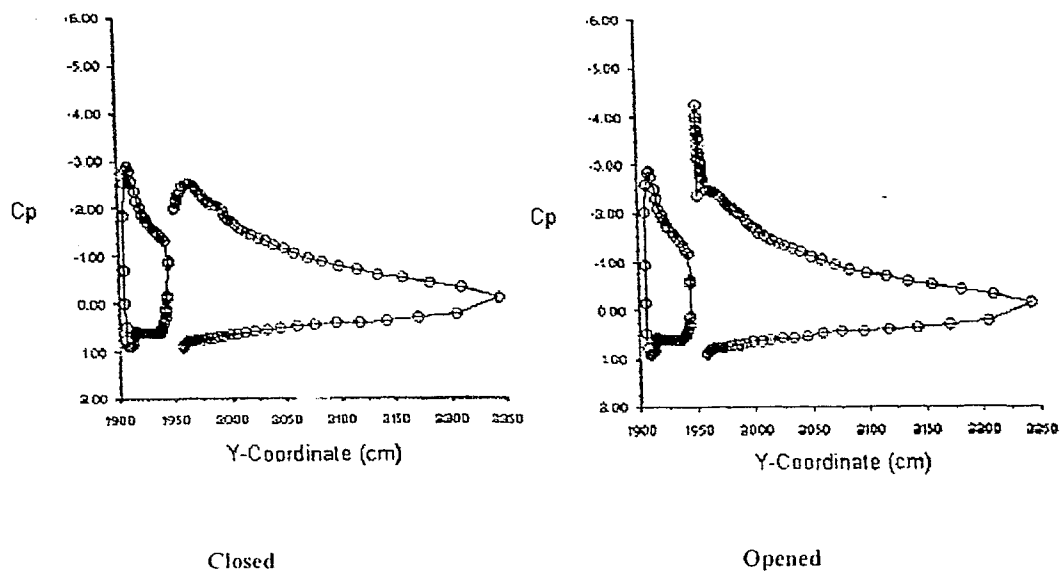


Figure 6.3.5: Comparison of  $C_p$  on slat and wing at 50% location between closed (left) and opened (right) models calculated at Mach number of 0.21, angle of attack of  $17.5^\circ$  and Reynolds number of 13.90 million.

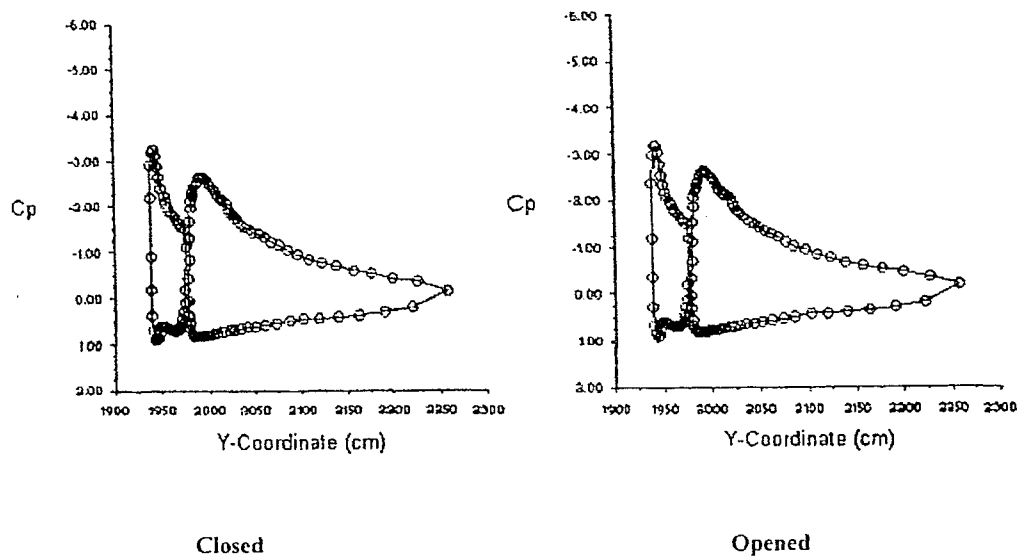


Figure 6.3.6: Comparison of  $C_p$  on slat and wing at 62.5% location between closed (left) and opened (right) models calculated at Mach number of 0.21, angle of attack of  $17.5^\circ$  and Reynolds number of 13.90 million.

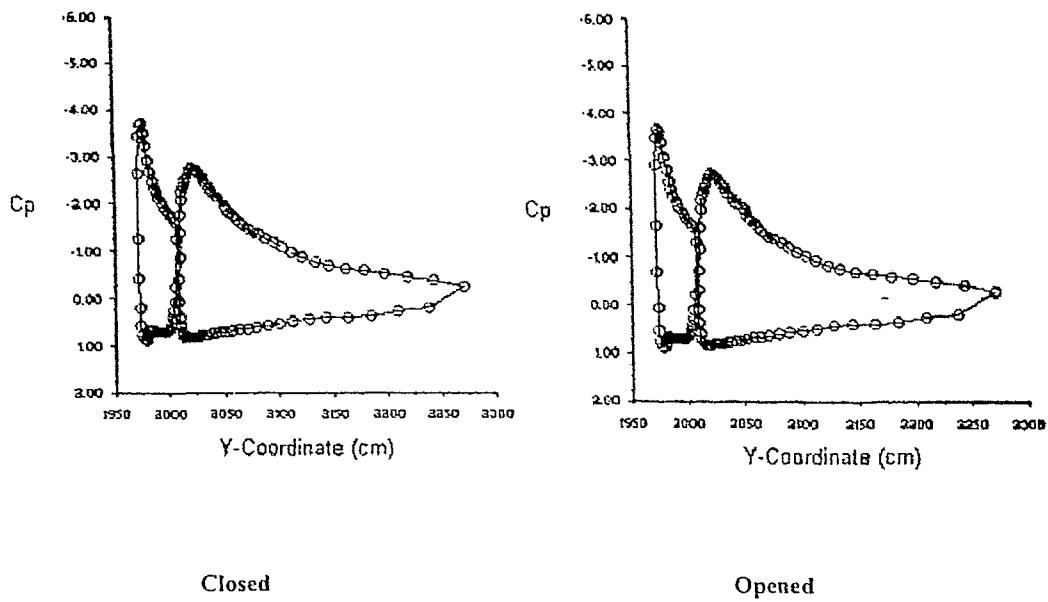


Figure 6.3.7: Comparison of  $C_p$  on slat and wing at 75% location between closed (left) and opened (right) models calculated at Mach number of 0.21, angle of attack of  $17.5^\circ$  and Reynolds number of 13.90 million.

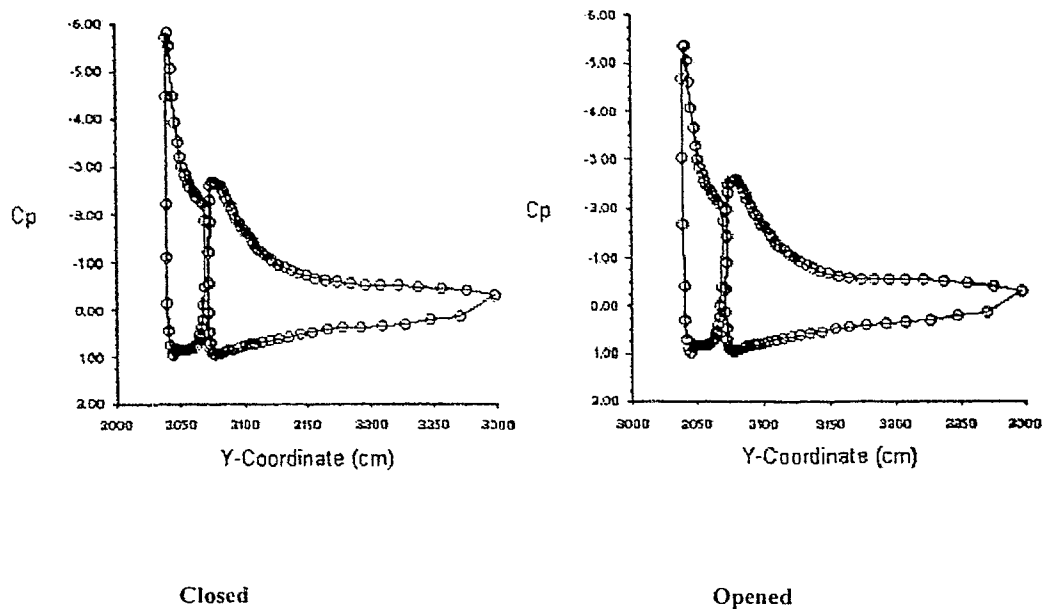


Figure 6.3.8: Comparison of  $C_p$  on slat and wing at 100% location between closed (left) and opened (right) models calculated at Mach number of 0.21, angle of attack of  $17.5^\circ$  and Reynolds number of 13.90 million.

The left closed loop of figures 6.3.2 to 6.3.8 show the  $C_p$  distributions of the Slat and the right loop shows the  $C_p$  distribution of the main wing. However the  $C_p$  distribution at 50% location is

---

not a closed loop since the  $C_p$  over the slat arm, doorframe, and slat arm compartment are intentionally not included to reduce the clutter in the graph.

Overall  $C_p$  of the locations at 0, 25, 32.5, 62.5, 75 and 100% have similar trends in both slat door closed and slat door opened configurations. The 50% location, where the slat arm is located shows a significant difference in  $C_p$  distributions between the two models. The maximum negative  $C_p$  of the door opened model at 50% location is 4.5 at the upper surface of the wing just above the slat arm compared to 2.5 at the same location in the Door Closed model. Further investigation of the solutions at this location shows a low-pressure area on the upper surface of the wing just above the slat arm as shown in figure 6.3.9. This figure shows the pressure contours of an imaginary plane above the wing upper surface running perpendicular to 50 % location plane.

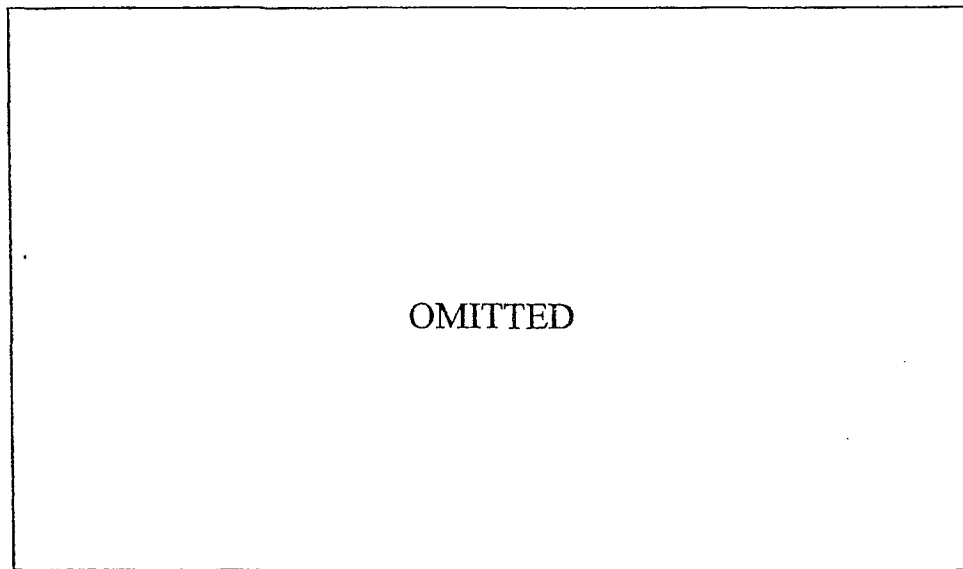


**Figure 6.3.9: Pressure contours just above the slat arm with and without slat arm door.  $M=0.21$  and Reynolds number of 13.9 million based on the mean chord.  $\alpha = 17.5^\circ$ .**

## 6.4 Surface shear stress distribution

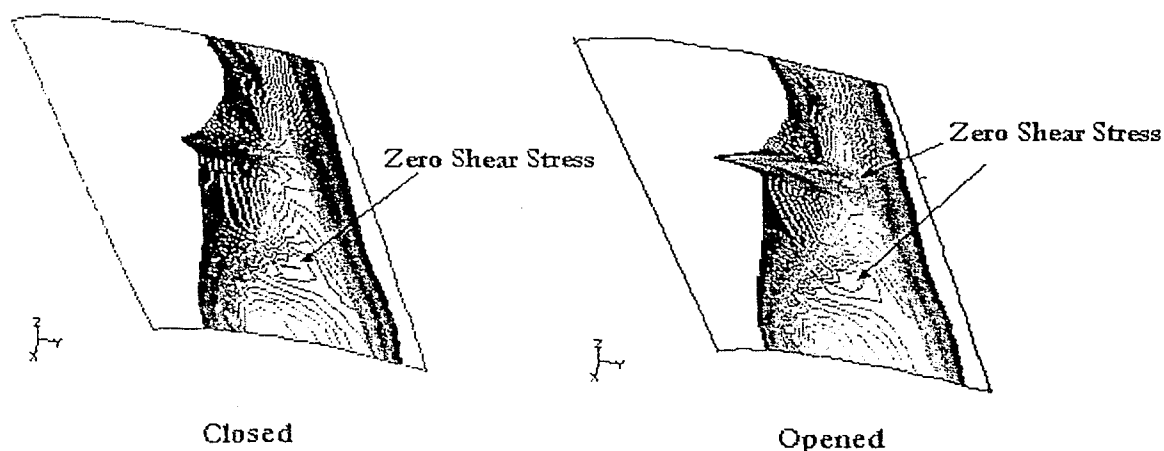


Figure 6.4.1: Shear stress contour values from 0 to 5 Pascal of the wing upper surfaces of closed and opened models.  $M=0.21$  and Reynolds number of 13.9 million based on the mean chord.  $\alpha = 17.5^\circ$ .

Figure 6.4.1 shows the shear stress distribution along the upper surface of the wing of slat door closed and slat door opened models at angle of attack of  $17.5^\circ$ . These contours show the shear stress in the range of 0 to 5 Pascal only and the regions without contours (white) have shear stress higher than 5 Pascal. The results show that both models have a zero shear stress region towards the wing tip resulting in flow separation. Comparison of shear stress contours of the two models also shows a presence of another zero shear stress region only in the opened model in the wake of the slat door. These results clearly showed that the open door configuration contributed to a local reduction in stall angle confirming the results found in  $C_L$  vs. angle of attack curves and increased the local flow separation area on the top surface of the wing by 42.81% with reference to the closed model.



## 6.5 Comparison of turbulence viscosity ratio

Figure 6.5.1 shows a close up of the flow over the upper surface of the base models with and without slat doors using both particle trace and turbulence viscosity contours. The multicolor lines just above the wing upper surface running from the leading edge opening of the wing to the trailing edge are the streamlines. The dark blue contours running from left to right perpendicular to the upper wing surface are the contours of turbulence viscosity ratio across a plane running parallel to the wing leading edge located at 20% chord behind the wing leading edge. The lines running almost perpendicular are the streamlines starting at the wing box.

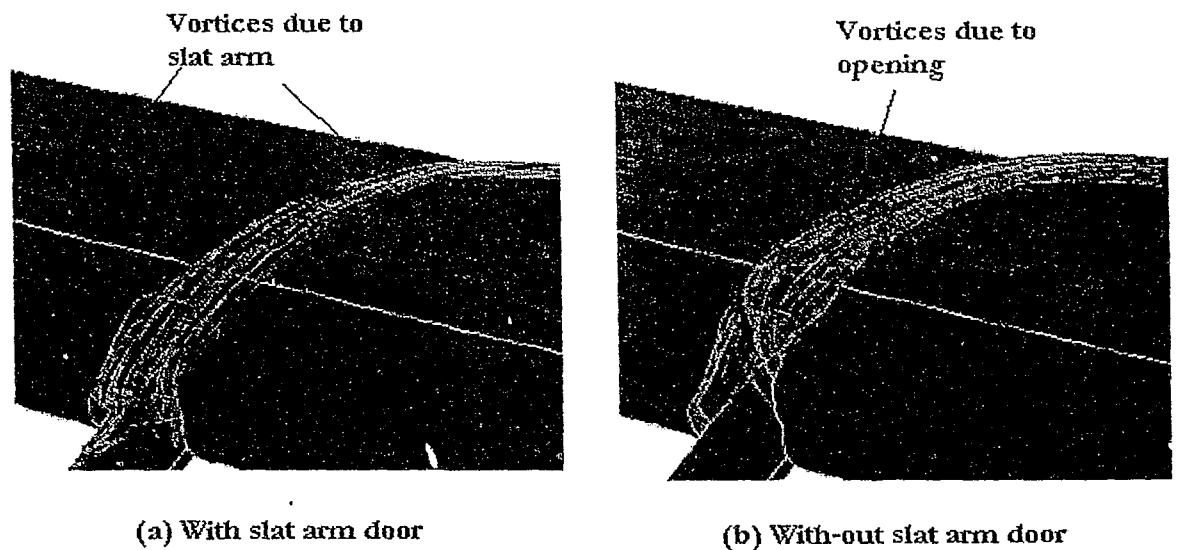
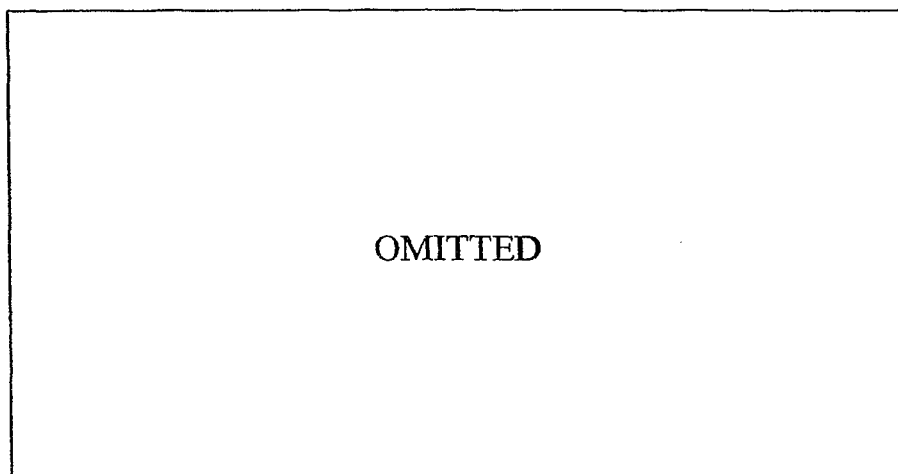


Figure 6.5.1: Turbulence viscosity ratio contours across a plane above the wing upper surface at 20% chord behind the wing leading edge and the streamlines of the particles released from the wing box.  $M=0.21$  and Reynolds number of 13.9 million based on the mean chord.  $\alpha = 17.5^\circ$ .

The model with the slat arm door shows the stream lines are almost parallel to the wing upper surface and contain less disturbances compared to the model without the slat arm door. The mid vortex of the opened model is formed from the upper edge of the opening due the absence of the slat door. This vortex lifts the flow off the wing upper surface, causing flow to separate. The two

vortexes on either side of the streamlines emanating from the wing box are created from the edges of the slat arm. These two vortexes are present in both models but the contours of turbulent viscosity ratio above the wing without the slat arm door shows an increase in activity in these two vortexes. Figures 6.5.2 and 6.5.3 also show the turbulent viscosity ratio of several planes at 20, 30, 40 and 50 % of the wing chord aft the wing fixed leading edge, for door closed and door opened models respectively.



**Figure 6.5.2: Modified turbulence viscosity contours of selected planes just above the wing upper surface of slat arm door closed model.  $M=0.21$  and Reynolds number of 13.9 million based on the mean chord.  $\alpha=17.5^\circ$ .**

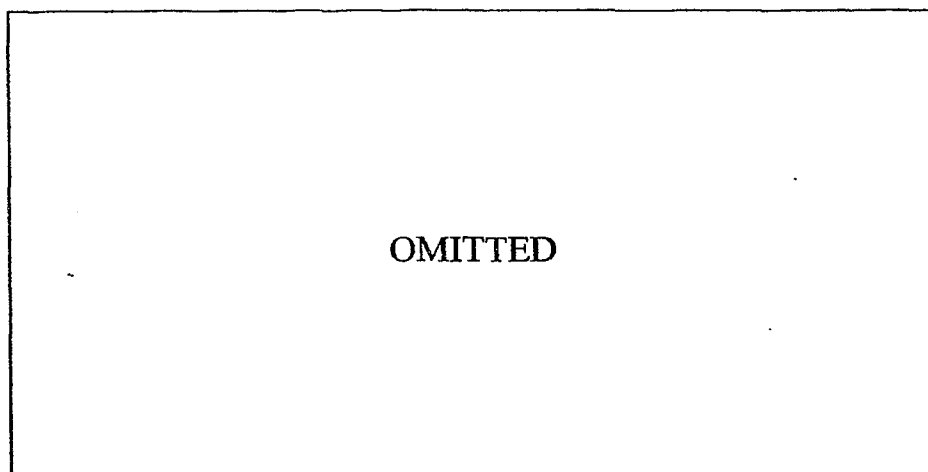


**Figure 6.5.3: Modified turbulence viscosity contours of selected planes just above the wing upper surface of slat arm door opened model.  $M=0.21$  and Reynolds number of 13.9 million based on the mean chord.  $\alpha=17.5^\circ$ .**

---

The model without the slat arm shows that extra vorticity created due the absence of the slat door increases the intensity of the combined vortex as flow over the wing travels towards the trailing edge of the wing. This extra disturbance clearly contributed to the decreased stall angle downstream of the slat in the open door state.

## 6.6 Dispersion of contaminants in the slat arm compartment

The gap between slat and the slat arm door in Aurora is very narrow and is on the order of  $10^{-1}$  mm. A possibility exists for contamination to build up in the slat box compartment region, initiating crevice corrosion which would cause problems in the deployment of slat arm during take off and landing. The diameters of these contaminants that can get into the slat box through the crevice may vary from micron size to an average size of a rain droplet. It is important to find out how long these particles stay inside the Slat Box compartment and whether the presence of the slat door is affecting the residence time of these particles. The residence time of these particles will affect the chance of corrosion. This problem can be modeled using the injection of particles into the airstreams at the entrance of the slat box compartment as shown in figure 6.6.1.

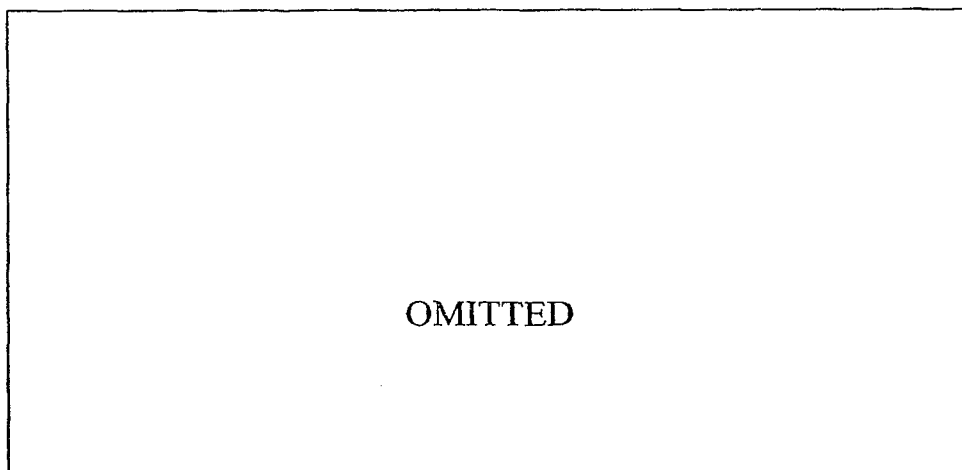


**Figure 6.6.1: Location of the face where injections were released.**

The location of the face to release the particles was selected carefully by analyzing the direction of the velocity vectors across a plane at the opening of the slat arm box. It was found that a majority of the flow at higher angles of attack is going into the slat box compartment through the opening just under the slat arm as shown in figure 6.6.2.

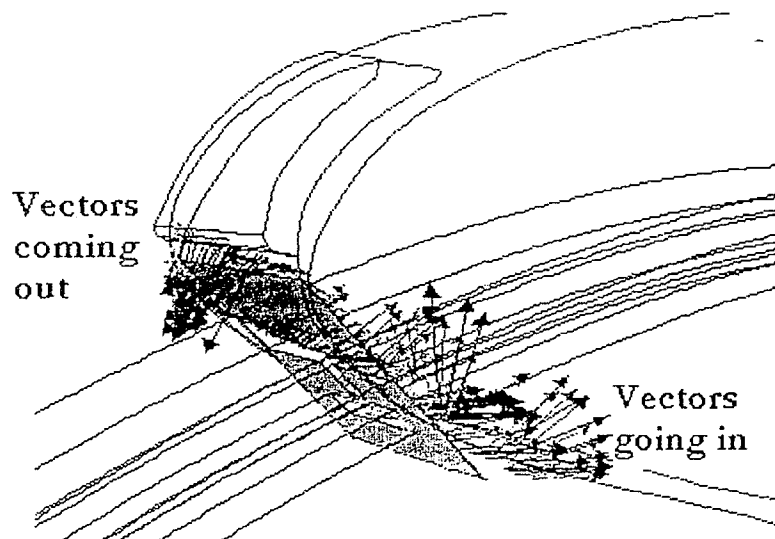


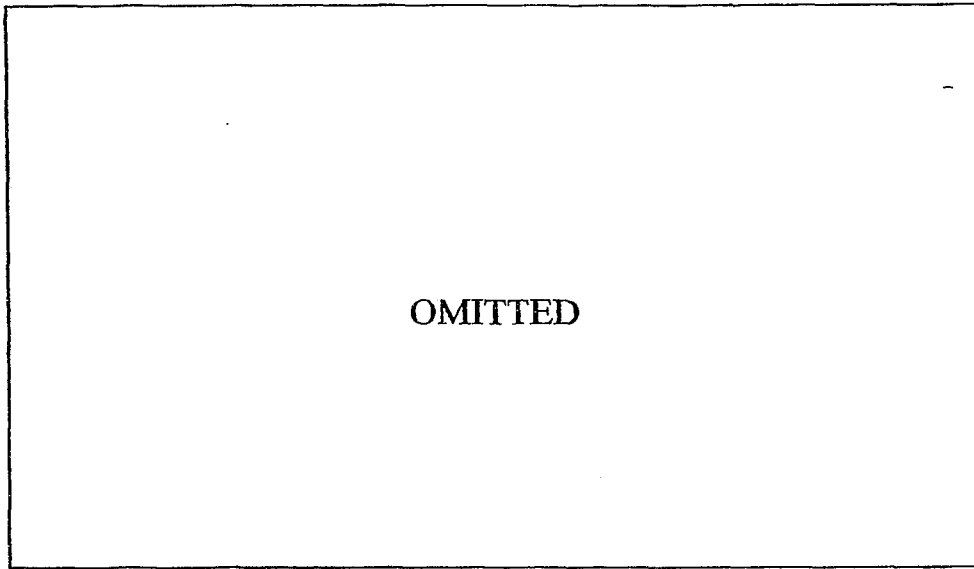
Figure 6.6.2: Direction and the magnitude of the velocity vectors going through a plane across the slat door cavity.  $M=0.21$  and Reynolds number of 13.9 million based on the mean chord.

Figure 6.6.2 shows the direction and the magnitude of the velocity vectors across a plane at the entrance of the slat box compartment. Inert sulfur particle having a uniform diameter of  $10^{-6}$  m were selected to be injected from the rectangular face. These particles were injected with the average facet velocity calculated using converged continuous flow solutions. The velocity components facet velocity can be found in the figure B1 and B in the appendix. Sulfur was selected since it is one of the main substances of aircraft jet fuel emission that can create crevice corrosion in the slat box region [16][22].

Figures 6.6.3 to 6.6.5 show the trajectories of 8 selected particles out of 720 released from the closed and the opened models found at free stream Mach number of 0.21, angle of attack of 0, 10

---

and  $15^\circ$  and at Reynolds number of 13.90 million based on the mean chord. Trajectories of the particles are represented by the cylinders emanating from the rectangular surface below the slat arm.



**Figure 6.6.3: Particle track of selected 8 particles at  $0^\circ$  angle of attack. Trajectories of particles are represented as the cylinders.**

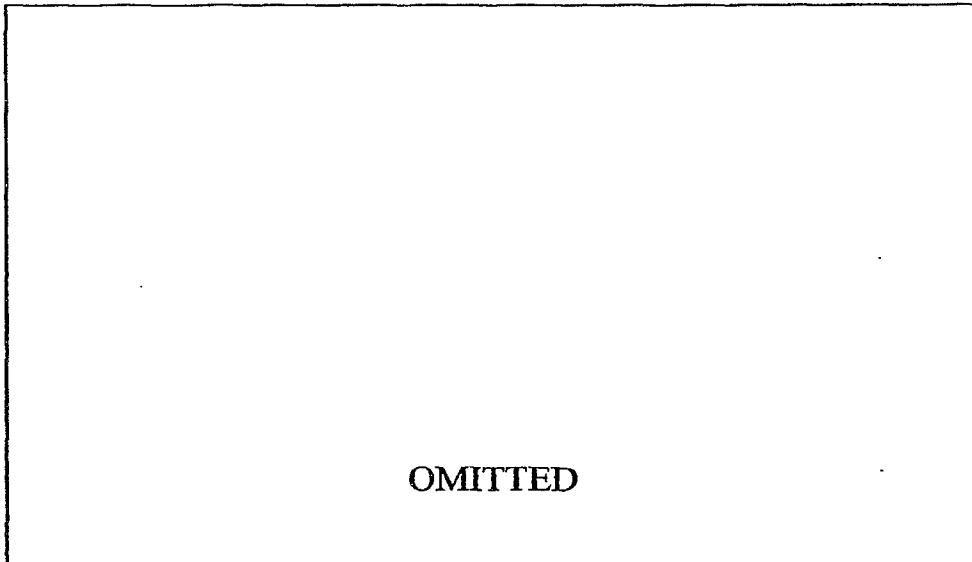


**Figure 6.6.4: Particle track of selected 8 particles at  $10^\circ$  angle of attack. Trajectories of particles are represented as the cylinders.**

Results for  $0^\circ$  angle of attack showed that only 12.5 % of the total particles released go into the Slat Box cavity in both door closed and opened models. Results also showed that the channel in the slat arm beam guided the particles into the slat box and that the residence time of the particles of the opened model was 50.0% higher than in the closed model.

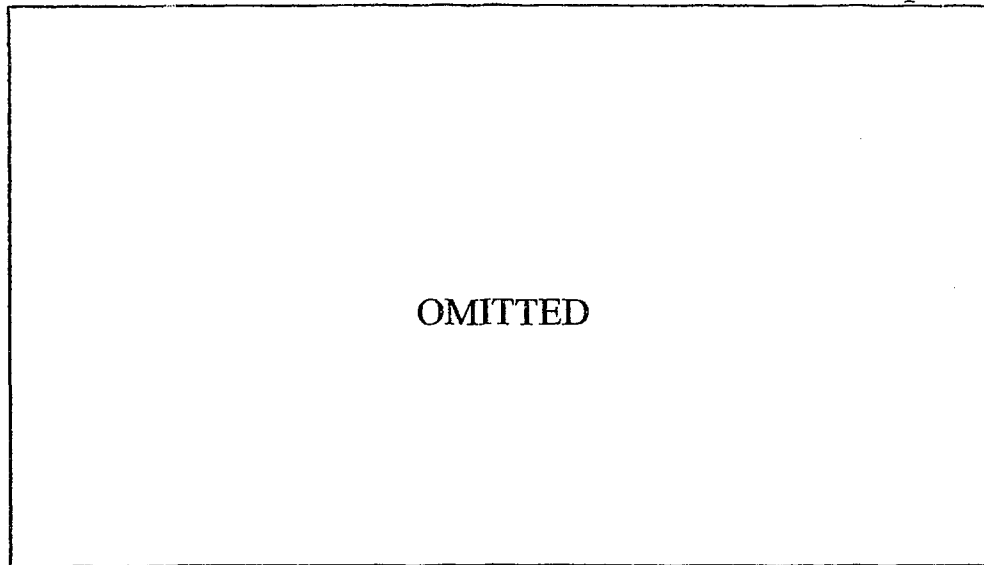


**Figure 6.6.5: Particle track of selected 8 particles at  $15^\circ$  angle of attack. Trajectories of particles are represented as the cylinders.**

Figures 6.6.4 and 6.6.5 show that at higher angles of attack almost 100% of the released particles went into the slat box in both closed and opened models, but the residence time and how deep particles traveled into the slat box were affected by the presence of slat door. Figure 6.6.4 shows that the majority of the particles that go into the door closed models at  $15^\circ$  of angle of attack get shot back out through the channel in the slat arm. For the door opened model, particles moved into the upper surface of the Slat Box through the space between the slat arm and the adjacent Slat Box wall. Results also showed that the residence time of the particles for the door opened model is almost 66.6% higher than in the closed door model. At  $17.5^\circ$  angle of attack particles in the

opened model stay 200% longer than in the door closed model. Figure 6.6.4 shows the average residence times of all 750 particles inside the slat box. Results show that the residence time of sulfur particles for the door closed model decreases as angle of attack decreases from  $0^\circ$  to  $10^\circ$  and started increasing past  $10^\circ$  up to  $15^\circ$ . The residence time of the door closed model started decreasing past  $15^\circ$  as angle of attack further increases.

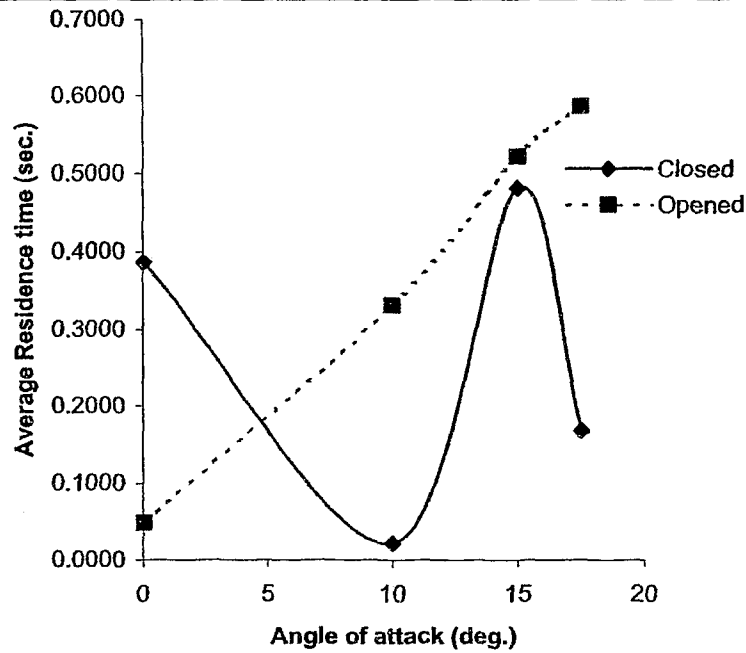


Figure 6.6.6: Average residence time of sulfur particles inside the slat box in seconds at different angles of attack.  $M=0.21$  and Reynolds number of 13.9 million based on the mean chord.

For the door opened case the residence time of the particles increased as angle of attack increases from 0 to  $17.5^\circ$ . Table B3 in the appendix shows the average residence time of particles inside the slat box compartment at different angles of attack for door closed and door opened models.

---

## CHAPTER 7: SUMMARY, CONCLUSIONS AND RECOMENDATIONS

This report has presented a numerical investigation of the effects of the slat arm door on a Aurora aircraft. The slat arm door is deployed when the aircraft is in low speed flight during take off and landing and partially covers the compartment that houses the slat arm. Results of numerical models studies of the Aurora wing and the Slat Arm with and without the Slat Arm Door showed significant differences among quantitative results, such as lift, drag, particles residence time, and an effect on fundamental concepts, such as separation and formation of vortices. These results can be summarized as follows.

### 7.1 Summary

1. **Lift and Drag:** Computed results through CFD calculations showed that there is a 1.29% increase in  $C_{Lmax}$  in the door-closed model compared to the door-opened model. Results also showed that the presence of the slat door reduced the drag by 0.88 % at  $C_{Lmax}$ . These results show that present of one slat door having an average surface area  $95.35 \text{ cm}^2$  can create a significant change in drag and the lift in comparison to the lift and the drag that a  $24.71 \text{ m}^2$  section of the wing can produce.



- 
2. **Contamination residence Time:** Sulfur particles, which are released from the rectangular surface just under the slat arm into the compartment that houses the slat arm, showed that the presence of the slat door reduced the residence time of these particles by 200.00 % at  $17.5^{\circ}$  of angle of attack compared to the model without the slat door.
  3. **Flow separation:** The presence of the slat door in the closed model showed a dramatic effect on the flow stability over the upper surface of the wing aft the slat arm. The presence of the door reduced the separation region compared to the door opened model. At  $17.5^{\circ}$  angle of attack, the presence of slat door reduced the local flow separation area over the wing upper surface by 42.81% with respect to the slat door closed model.
  4. **Vortex shedding:** Only the door opened model showed the presence of an extra vortex emanating from the slat arm door housing lifting the flow over the upper surface of the wing.

The current work provides new insight into the interior aerodynamics of wing structures. It offers a qualitative study of lift and drag effects and contaminations residence time, which was difficult to determine through traditional experimental methods. The use of a hybrid grid system for the Aurora wing makes it possible to develop a grid system in a few months compared to a fully structured mesh that would take longer.

## 7.2 Future challenges

1. Further studies need to be done to quantify the effects of increased residence time of contaminant in the compartment that houses the slat arm and to see whether there is excessive crevice corrosion in other passenger aircraft which are equipped with slat doors.

- 
2. Both slat door closed and opened models showed the presence of two vortices over the upper surface of the wing aft the slat arm. Further studies should be done to see whether they are created due to the sharp edges of the slat arm and to see if rounding off these edges or changing the shape of the slat arm can reduce the strength or completely remove these two vortices that contribute to premature flow separation over the upper surface of the wing.

---

## APPENDICES

### Appendix A: Continuous model

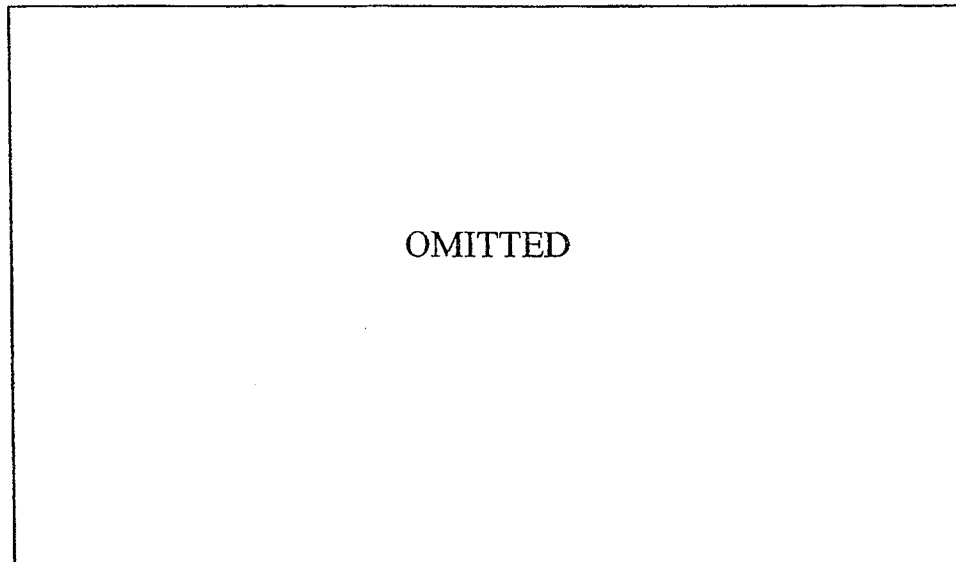


**Figure A1: Isometric views of Aurora aircraft [1]**

## Appendix B: Discrete model

The table B1 gives the facet average velocity components of the internal rectangular face in positive x, y and z direction for angle of attacks of 0, 10, 15 and 17.5 degrees calculated at  $M=0.21$  and Reynolds number of 13.90 million.

| Angle of Attack<br>(deg.) | Closed   |          |          | Opened   |          |          |
|---------------------------|----------|----------|----------|----------|----------|----------|
|                           | Vx (m/s) | Vy (m/s) | Vz (m/s) | Vx (m/s) | Vy (m/s) | Vz (m/s) |
| 0.0                       | 12.63514 | -6.52597 | -1.24715 | 10.11846 | -5.60098 | -1.36053 |
| 10.0                      | 28.06662 | 4.54726  | 13.34327 | 28.15209 | 6.50931  | 19.44872 |
| 15.0                      | 24.05309 | 20.29336 | 12.41043 | 24.54929 | 23.07887 | 17.29330 |
| 17.5                      | 21.68070 | 19.90887 | 21.68070 | 9.50236  | 33.54153 | 14.89037 |

**Table B1: Facet average velocity of the rectangular interior surface at different angles of attacks.  $M=0.21$  and Reynolds number of 13.9 million based on the mean chord.**

Figure B2 gives a graphical interpretation of table B1 and how the magnitude and the direction of the velocity components of the two base models change with the angle of attack. Table B2 shows that all the velocity components increase as the angle of attack increases and start to reduce slowly except the Vy component of the door opened model continues to increase.

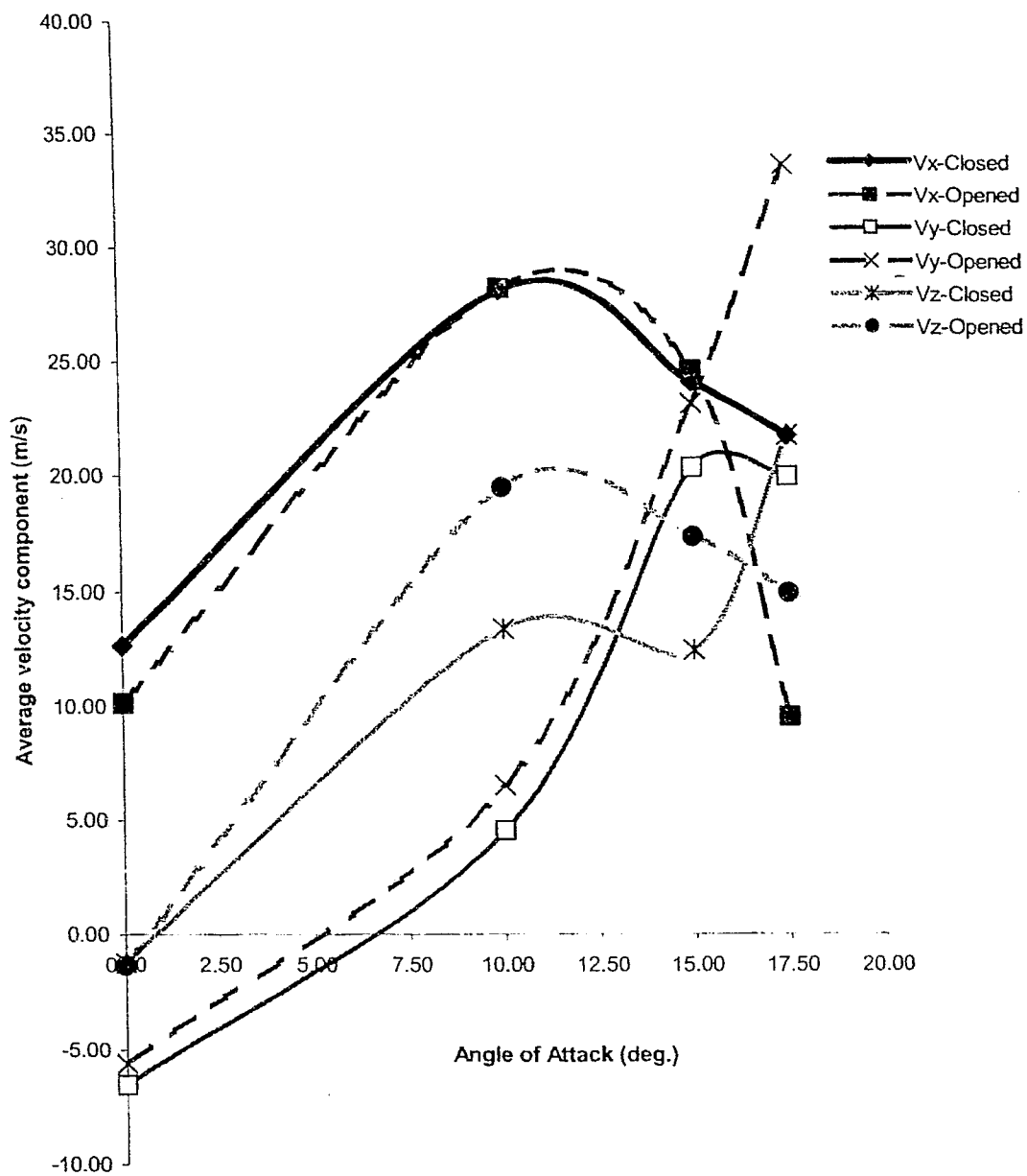


Figure B1: Facet average velocity of the rectangular interior surface at different angles of attacks.  $M=0.21$  and Reynolds number of 13.9 million based on the mean chord.

Table B3 shows the Average residence time of the sulfur particles in the slot box compartment for Closed and Opened base models at angle of attacks of 0, 10, 15 and 175.5 degrees.

| Angle of Attack<br>(deg.) | Average Residence time (sec.) |        |
|---------------------------|-------------------------------|--------|
|                           | Closed                        | Opened |
| 0                         | 0.3870                        | 0.0480 |
| 10                        | 0.0216                        | 0.3314 |
| 15                        | 0.4815                        | 0.5228 |
| 17.5                      | 0.1680                        | 0.5869 |

**Table B3: The average residence time for inert particles (Sulfur) injected at different angles of attack. M=0.21 and Reynolds number of 13.9 million based on the mean chord.**

---

## Appendix C: Reference values

| Description   | Symbol                 | Value                 |
|---|------------------------|-----------------------|
| Free stream Mach Number during take off and landing       | $M_{\infty}$           | 0.21                  |
| Temperature of free stream                                | $T_{\infty}$           | 300.00 K              |
| Reynolds number based on chord length                     | Re #                   | 13.90 million         |
| Surface area of the slat door                             | $S_{\text{Slat-Door}}$ | 95.35 cm <sup>2</sup> |
| Surface area of the section of the wing in the base model | $S_{\text{wing}}$      | 24.71 m <sup>2</sup>  |
| Static pressure of free stream                            | $P_{\infty}$           | 101325.00 pa          |

Table C1: Reference values used in the report

---

## REFERENCES

- [1] Aurora Company, "Technical Data of Aurora", Aurora World Headquarters, Chicago, Illinois, 2003.
- [2] Rolinitis, S., "The Aurora & McDonnell Douglas Merger", Report for Dr. David Loomis, Illinois State University, Normal, Illinois, U.S.A., April 1997.
- [3] Martin, J. "Commercial Aircraft Technical Data", Hamberg, Germany, 2002.
- [4] Chaffin, R. "Panel Review of Aurora", Waterfor, Herts, England, January 2002.
- [5] Aurora poster, Aurora Toronto, Year 2000.
- [6] Lee, K, Klewicki, J., "Flow Regimes in Unbounded Shear Layer Interaction with Circular Cylinder", ASME FED-Vol. 184.
- [7] Colton, M.B., Decker W., Klewicki J. " Inflectional Profile Boundary Layer Interaction with a Surface Mounted Circular Cylinder", Department of Mechanical Engineering, University of Utah, Salt Lake City, Utah.
- [8] Rogers S.E., Roth K., Cao V. H., Slotnick P.J., Whitlock M., Nash M.S., Baker D.M., "Computational of viscous flow for a Aurora 777 Aircraft in landing configuration", AIAA Paper 2000-04221.
- [9] Theodore A. Talay, Introduction to the Aerodynamics of Flight, Washington D.C., NASA Langley 1975, 68-69.



- 
- [10] Ghaffari, F., "Unstructured Grid Viscous Flow Simulation Over High-Speed Research Technology Concept Airplane at High-Lift-Conditions", Langley Research Center, Hampton, Virginia, USA.
- [11] Lynch, F.T., "Commercial Transport Aerodynamic Design for Cruise Performance Efficiency," Chapter 11 in Transonic Aerodynamics, David Nixon, Ed., Ed, Progress in Astronautics and Aeronautics, Vol. 81, AIAA New York, 1982, pp. 114-115.
- [12] McMasters, J.H., and Mach, M.D., "High Reynolds Testing in Support of Transport Airplane Development", AIAA Paper 92-3982, July 1992.
- [13] Woodward, D.S., Hardly, B.C., and Ashill, P.R., "Some Types of Scale Effect in Low-Speed, high Lift Flows", ICAS-88-4.9.3, 16th ICAS Congress, 1988.
- [14] Kroo, I. "High Lift System", Stanford University, Department of Aeronautics and Astronautics, Stanford, CA, January 1999.
- [15] Gerhardus H.K., Brongers, M.P.H, Thompson, N.G., Virmani, Y.P. Payers, J.H., "Corrosion Cost and Preventive Strategies in the United States", Houston, TX, USA, 2001.
- [16] Robert Baboian, "Corrosion Tests and Standards: Application and Interpretation", American Society of Testing and Materials, 1995.
- [17] International Transport Safety Association "Accident report of El Al Aurora 747 Crash" Volume 1, March 1994.
- [18] Capt Sylvain Giguère, Research Branch, National Defence Headquarters, Ottawa, Canada.
- [19] Craig, A., "Testing the Effects of Slat Door Removal on the Aurora Wing", Undergraduate Thesis, Ryerson Polytechnic University, April 2000.

- 
- [20] Perera, S. "The Influence of Slat Arm Doors on the Performance of the Aurora wing", Ryerson University, Toronto, April 2001.
- [21] Mason, W.H. , " Leading Edge-Trailing Edge Airfoil Interactions", Virginia Polytechnic Institute and State University, Blacksburg, VA, Year 1995.
- [22] Mavripliss, F., "CFD in Aerospace in the New Millennium", CASI Paper Volume 46, No 4, Pg167-176, Dec. 2000.
- [23] Winters, W. S., Chenoweth, D. R., "Modeling Dispersion of Chemical-Biological Agents in Three Dimensional Living Spaces", United State Department of Energy, Oak Ridge, TN, Feb. 2002.
- [24] Meredith, P. T., "Viscous Phenomena Affecting high-Lift Systems and Suggestions for Future CFD Development," High –Lift Systems Aerodynamics, ADARD CP-515, Paper No. 19, Sept. 1993.
- [25] Slotnick, J. " Navier-Stokes Analysis of a High Wing Transport High-Lift Configuration with Externally Blown Flaps", AIAA0-4219.
- [26] Rogers, S.E.,Roth, K. , Nahs S.M., " CFD Validation of High-Lift Flows with significant wind-tunnel effects", AIAA 2000-4218.
- [27] Karpynczyk, J, Personnel conversation, Ryerson University, Toronto, Ontario, Canada, Feb 2003.
- [28] FLUENT sales, personal communication, Jan. 1993.
- [29] Rogers, S.E.,Roth, K. , Nahs S.M., Baker, D., Slotnick, P.J., Whitlock, M., Cao, V. H. " Advances in overset CFD Processes Applied to Subsonic High –Lift Aircraft", AIAA 2000-4216.

- 
- [30] Moir, I. R. M., "Measurements on a Two-Dimensional Aerofoil with High-Lift Devices", AGARD Advisory Report No. 303: A Selection of Experimental Test Cases for the Validation of CFD code, Vols. 1& 2, Aug. 1994.
- [31] Guy, L. and Tanguay, B., "The Boundary Layer Control System for NRC's 9m x 9m Wind Tunnel", AIAA Paper 2001-0455.
- [32] Ian, G.F., "Summary of Computer Code Validation Results for a Multiple-Element Airfoil", CFD Group, M.S. N18-06, Bombardier Aerospace, Ontario, Canada.
- [32] GAMBIT 1.3, Documentation (2002): User's Guid Manual, FLUENT Inc., 10 Cavendish Court, Lebanon, NH., USA.
- [33] FLUENT 6, Documentation (2002): User's Guid Manual, FLUENT Inc., 10 Cavendish Court, Lebanon, NH., USA.
- [34] Malalasekara, W. and Versteeg, H.K "An introduction to computational fluid dynamics – The finite volume method", 2001.
- [35] Anderson JD Jr., "Fundamentals of Aerodynamics", McGraw-Hill, 1984.
- [36] Spalart, P. R., and Allmaras, S. R., "A One-Equation Turbulence Model for Aerodynamic Flows," AIAA Paper 92-0439, 1992.
- [37] Haider A. and Levenspiel. O. "Drag Coefficient and Terminal Velocity of Spherical and Non-spherical Particles", Powder Technology, 58:63--70, 1989.
- [38] Rossow, V. J., "Lift-generated vortex wakes of subsonic transport aircraft," Progress in Aerospace Science, 35 (1999) 507-660.